ABSTRACT

Title of Document: **DRAG COEFFICIENT STUDY OF TWO WALL-MOUNTED OBSTACLES**

Ana Ramekar, Candidate for Master of Science, 2018

Directed By: Prof. Elaine Oran, Aerospace Department

In order to support various intelligence, surveillance, reconnaissance (ISR) missions, aircraft often undergo structural changes that affect the aircraft's aerodynamics. A computational fluid dynamics (CFD) study was performed to understand changes to the drag coefficient when two wall-mounted obstacles, representative of common ISR modifications, are positioned in a tandem configuration and exposed to fully subsonic flow. The size, shape and position of the two obstacles is varied. The CFD study used three-dimensional, steady-state, compressible, Reynolds Averaged Navier Stokes equations.

The study reported four major results. First, interference effects generally increase the drag of the trailing obstacle up to 45% and generally decreases the drag of the leading obstacle up to 27%. Second, the interference effects on both obstacles produces a 12% reduction in drag at the lower Mach numbers studied and a 37% increase in drag at the higher Mach numbers studied. Third, a larger trailing obstacle will reduce the drag of a leading obstacle of a smaller size. Lastly, the region where interference effects occur becomes smaller if the fineness ratio of the trailing obstacle increases.

DRAG COEFFICIENT STUDY OF TWO WALL-MOUNTED OBSTACLES

By

Ana Ramekar

Thesis submitted to the Faculty of the Graduate School of the
University of Maryland, College Park, in partial fulfillment
of the requirements for the degree of
Master of Science
2018

Advisory Committee:
Professor Elaine Oran, Chair
Professor Jewel Barlow
Professor Anya Jones

Acknowledgements

There are several people I would like to express my sincerest gratitude to. First, thank you to my advisor, Prof. Elaine Oran, for your patience, guidance, and the opportunity to join your research team. Thank you to Prof. Ryan Houim for the invaluable discussions and helping me get my project on track in its earliest phase. Thank you to fellow graduate students for all the feedback shared over the years. Lastly, thank you to the entire staff of the University of Maryland's Aerospace department, without whom my academic success would not be possible.

Table of Contents

List of Tables

List of Figures

List of Abbreviations and Symbols

Acronym	Definition
α	Angle of Attack
γ	Ratio of heat capacity
ϵ	Turbulent dissipation
κ	Von Karman constant
ρ	Density
μ	Dynamic Viscosity
μ_τ	Friction velocity
τ	Shear stress
τ_w	Shear stress at wall
ω	Specific turbulent dissipation rate of energy
A	Area, Axial force
AFM	Aircraft Flight Manual
c	Chord
C_D	Coefficient of drag
C_P	Coefficient of pressure
CAD	Computer Aided Design
CFD	Computational Fluid Dynamics
D	Drag force
E	Energy
ELINT	Electronic Intelligence
FAA	Federal Aviation Administration
FL	Flight Level – designates altitude in hundreds of feet
GUI	Graphical User Interface
ISA	International Standard Atmosphere
ISR	Intelligence, Surveillance, Reconnaissance
K	Turbulent kinetic energy
KA300	King Air 300
L	Lift force, Length
LE	Leading Edge
M	Mach number
N	Normal Force
N.S.	Navier-Stokes
OML	Outside Mold Line
P	Pressure
PDE	Partial Differential Equation
q_∞	Dynamic pressure
R	Aerodynamic resultant force
R_{ij}	Reynolds stress

Re	Reynolds Number
RANS	Reynolds Averaged Navier-Stokes
R&D	Research and Development
RFP	Request for Proposal
S_{ij}	Mean rate of deformation
SIGINT	Signal Intelligence
t	Time
T	Temperature
TE	Trailing Edge
U	Velocity
u+	Dimensionless velocity
V	Velocity
X_i	Position
y+	Dimensionless position normal to a wall
z	Geometric altitude

Chapter 1: Introduction

Modification of Existing Aircraft

Intelligence, surveillance and reconnaissance (ISR) aircraft play a major role in the current assets and future investments of the U.S. Army, Air Force and Navy. ISR planes are often existing aircraft that have been structurally, electronically or aerodynamically modified. These modifications include the removal and addition of physical structures to reduce weight, enhance performance, and provide space for new electronic systems and other payloads. Over the past few decades, the increasing cost for developing and testing new aircraft has prompted aircraft companies to look for economical alternatives that can meet customer requirements. Reusing aircraft for different purposes is very cost-effective.

The Hawker Beechcraft King Air 300 (KA300) is one of the most modified ISR aircraft. Its manufacturer and third-party vendors sell engineered modifications which are certified by the Federal Aviation Administration (FAA), and their aerodynamic performance is well documented. Many planes, however, require custom aerodynamic modifications, and the assessing impact to the aerodynamic performance of custom modifications is an expensive endeavor.

Objectives

By identifying relationships between the coefficient of drag and design parameters, such as the size of a modification and the distance between modifications, this study will help designers and engineers propose more efficient changes to aircrafts like the KA300.

Two Examples of Modifications

TU-214R. The Russian Air Force TU-214R Reconnaissance Aircraft (Figure 2), deployed in the Syrian war zone in February 2016,[1] was converted from a TU-204 (Figure 1), a twin-engine, medium-range passenger jet. (The Figure 2 photo has been flipped horizontally to facilitate comparison of the original aircraft and its modified form.).

Figure 1. A Tu-214R with several modifications.

Figure 2. The unmodified TU-204 in flight.

The TU-214R was outfitted with several radomes, or housings for electronic intelligence (ELINT) equipment and signal intelligence (SIGINT) equipment. At least two radomes were placed on the left hand side behind the cockpit and behind the wing. The aircraft's belly was also modified behind the nose landing gear and behind the wing structure. These radome modifications change the airflow around the TU-214R and generate additional drag, which impacts aircraft performance. The engineers responsible for the layouts of these modifications tend to reuse past designs, seldom knowing how they will affect aircraft performance. In general, the appropriate engineers calculate the performance impact much later, during the design validation and testing phases, using Computational Fluid Dynamics (CFD) or flight tests. The results of CFD or flight tests

rarely drive the layout and design so the engineers often accept the performance impact as a necessary penalty.

E11A. The US Air Force's E-11A aircraft (Figure 4)[2] was originally a Bombardier Aerospace Global 6000, an ultra-long-range business jet (Figure 3).[3] It was modified with a large droplet-shaped radome addition, four small antennae on top of the plane, and a half-cylindrical shaped radome on its belly for housing SIGINT and ELINT equipment.

Figure 4. E-11A with several major modifications.

Figure 3. Bombardier Aerospace Global 6000.

These modifications, especially smaller equipment such as antennae, are placed on the surface with little consideration for the aerodynamic penalty. The study aims to help designers to position antennas, cameras, fairings and other aircraft modifications more wisely.

Request for Proposals

When working on ISR aircraft modifications in the proposal stages, a design team's timeline and budget often limits the amount of data available to make informed choices. The structural or systems engineers who work on aircraft modifications often disregard the aerodynamic ramifications of their design choices since wind tunnel tests or CFD results are expensive and time consuming. To illustrate why the designs are often finalized without

thoroughly searching for the optimal solution, a basic sequence events during the proposal process is now outlined.

First, the customer defines a set of requirements for a new aircraft and asks the industry for feedback. Companies in the industry provide feedback to the customer in hopes that they will influence the revised requirements in a way that makes their own product the most qualified solution. The customer incorporates some of the feedback into a formal document known as a request for proposal (RFP). Engineers at competing companies start their design concepts and address the official requirements stated in the RFP. Engineers begin the process of designing their aircraft, addressing the costs and associated risks. Unless engineers have extensive funding available, they must make decisions about their aircraft design without optimizing the aerodynamics.

The customer eventually evaluates the various solutions from competing companies and awards the contract to one of them. The winning company continues to develop and test the initially design concept, often lacking funds to redesign and revamp the initial proposal under contractual obligation to remain faithful to the proposed design. The layout of the aircraft modifications is thus determined very early in the development phase, with limited data.

Engineers therefore respond to RFPs with limited tools even though CFD results can be useful at an earlier stage in the design process. A goal of this thesis is to improve the design of aircraft modifications by narrowing the gap between engineers working on proposals and the aerodynamicists, who use wind tunnel data or CFD analysis to predict the aerodynamic performance impact of modifications. This paper solely considers modifications that alter the aircraft's outside mold line (OML).

Chapter 2: Background and Perspective

Sources of Drag

The drag force opposes the motion of objects through a medium and therefore reduces the efficiency of that movement. Energy must be spent to overcome drag. All aircraft experience drag when moving through earth's atmosphere. The energy necessary to overcome the drag force is provided by burning fuel in an engine and creating thrust. In order to reduce fuel costs, aerospace engineers spend a lot of time minimizing the drag force.

To understand the magnitude of the drag force, it is helpful to understand what causes it. The different sources of drag on an aircraft are outlined in Figure 5, as adapted from the National Test Pilot School's Handbook of Aerodynamics for Flight Testers.

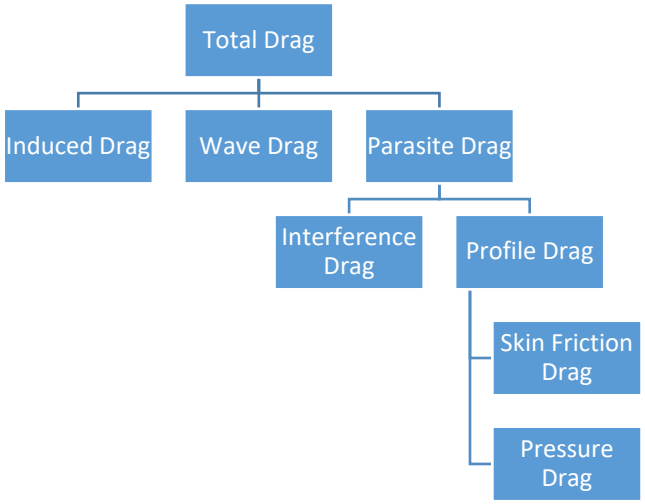

Figure 5. Source of drag on aircraft.

Induced drag arises when a lift-generating and streamlined object redirects fluid from a high-pressure region to low-pressure region. It is sometimes called "vortex drag," because the air leaks from the high pressure region to the lower pressure region creating a

trailing vortex system shown in Figure 6. The leaking air “induces” a net force in the direction opposite to the motion of the object, which is drag. Induced drag scales inversely with flow velocity, but it does not decay to zero. Winglets are sometimes used to prevent leakage and reduce induced drag.

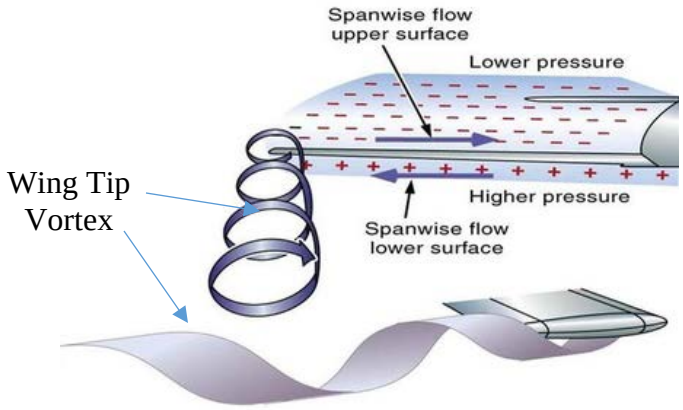

Figure 6. Wing tip vortex due to induced drag.[4]

Wave drag occurs in transonic and supersonic flow due to the formation of shock waves. The shock waves lead to early flow separation and increase in pressure directly behind the shock front. Wave drag is mentioned here for completeness only. It will not be considered further since the focus of this paper is on objects in fully subsonic flow.

Parasitic drag, also known as the zero lift drag, is a major contributor to the total drag of an aircraft. Often, the geometry of a designed object is driven by the need to reduce parasitic drag. This source of drag is comprised of two types of drag, profile drag and interference drag.

Profile drag is further comprised of skin friction drag, which arises due to viscous forces acting on the object, and pressure drag, which arises due to an imbalance of pressure forces acting on the object. The profile drag is the component of pressure and viscous forces

that acts *parallel* to that object's flight path. Profile drag varies directly with the flow velocity and it is generally present in flows of practical engineering interest.

The second component of parasitic drag is interference drag, which is the major focus of this thesis. Consider two bodies located such that they touch each other, penetrate each other, or are located in close vicinity to each other. These two bodies will experience a drag different than the sum of the drag of each individual body (Eq. 1). This difference in drag is called *interference drag* (Eq. 2).

$$D_{1+2} \neq D_1 + D_2. \qquad \textit{Eq. 1}$$

$$D_{interference} = D_{1+2} - D_1 + D_2. \qquad \textit{Eq. 2}$$

The diversion of streamlines from their normal paths over the contour of each object element and the mixing of boundary-layers gives rise to interference drag.[5] Interference drag can have a negative value, meaning objects can be placed in proximity to each other such that the resulting drag on both objects is less than the sum of the drag of the bodies in isolation. This study is the beginning of an attempt to use CFD to gain understanding about placement of multiple objects with the goal of minimizing the interference drag.

Previous Works on Interference Drag

Why focus on interference drag? Considerable research is available on how to minimize induced drag, profile drag and wave drag. This is because viscous drag accounts for about 50% of the total drag while interference drag only accounts for about 5%. Total drag reduction has been achieved through new technologies such as (1) airfoils with leading and trailing edge geometries that reduce profile drag, (2) wing sweeps that delay the onset of wave drag, (3) devices such as slotted flaps, split flaps and fowler flaps that increase lift during takeoff and landing without increasing profile and induced drag in cruise conditions,

and (4) modifying wing twist and wing aspect ratios to influence viscous drag.[6] Studies focused on minimizing interference drag and the technologies derived from their results are not as prolific, especially for subsonic, compressible, aerospace applications.

The review that follows summarizes existing literature on interference drag on two or more wall-mounted objects. The topics to be discussed encompass sports and meteorology. Note that the Reynolds and Mach numbers studied in these applications vary considerably and are not the same as those of this thesis.

Interference drag of fully submerged objects has been studied as early as the 1933. The National Advisory Committee for Aeronautics (NACA) published reports on the drag of pairs of solid cylinders and streamlined objects located in tandem, side-by-side and intersecting positions.[7] The data collected from wind tunnel tests shows that streamlined struts placed in tandem experience an overall increase in drag due to interference effects. The total drag on individual objects varies as much as fourfold as the distance between the objects changes. The drag of the rear strut increases due to the presence of the front strut. Conversely, the drag of the front strut is reduced by almost an equal amount due to the presence of the rear strut. The data illustrating these effects is shown in Figure 7. Because these studies did not account for the presence of walls, it is difficult to relate the results to the interference drag on wall-mounted obstacles.

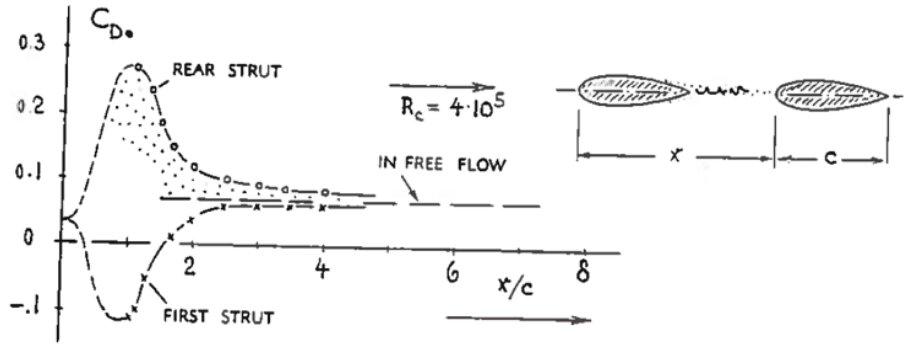

Figure 7. Drag vs. distance on a pair of fully submerged struts, one behind the other. [8]

In 1965, Hoerner published experimental data analyzing the interference drag of a single body mounted on a wall and compared it to the drag when no wall was present. [9] Hoerner provided a way to quantify interference drag between a single body and the wall by calculating its sensitivity ratio. The sensitivity ratio is a ratio of the drag of the body mounted on a wall to the drag of the body in freestream. For example, if a square plate mounted on a wall has a sensitivity ratio of 2, it means the square plate will have twice as much drag on a wall than if it was fully immersed in free stream flow. This lends itself to the idea that if the sensitivity ratio of simple objects, such as hemispheres, are calculated, that sensitivity can be leveraged to predict sensitivity ratios of more complex and realistic shapes. Hoerner also presents two parameters to represent the shape of his three-dimensional bodies: the fineness ratio, h/l and the thickness ratio, b/l. The dimensions used to calculate the fineness and thickness ratio are identified in Figure 8.

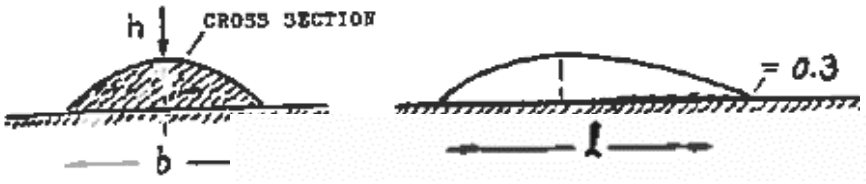

Figure 8. Basic dimension of obstacle shapes studied by Hoerner.[8]

Furthermore, Hoerner's research shows that to reduce drag of streamlined bodies, it is best to lengthen and flatten their geometry, that is, to increase the fineness ratio. These results are presented in Figure 9. Hoerner's work on the interference drag of wall-mounted objects provides the foundation for parametrizing problems involving obstacle geometry and interference drag.

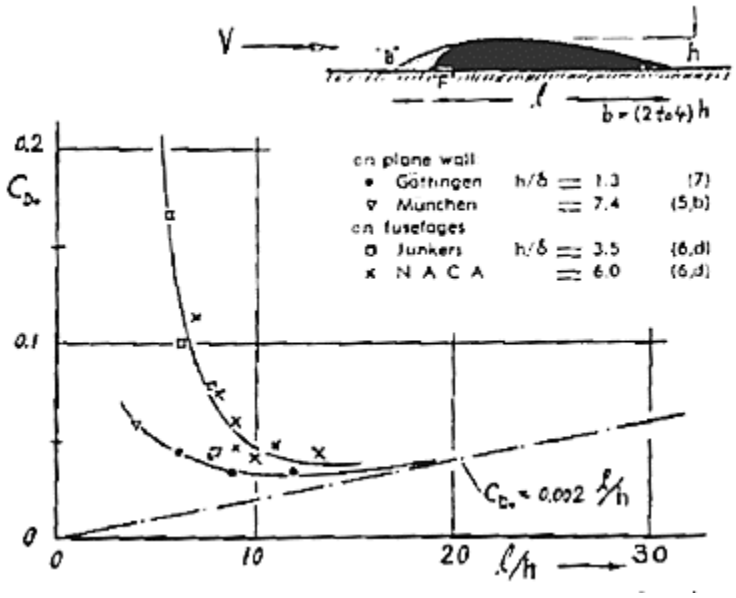

Figure 9. Drag coefficient of fairings as a function of their fineness ratio.[8]

In 1984, a NASA report analyzed the interference drag between a wing and fuselage structure.[10] The wing and fuselage were modeled as flat plates joined together in a perpendicular junction. Data was collected in a wind tunnel at a Reynolds number of approximately 9.9×10^5. The report concluded that the interference drag caused by bringing the two plates together is small, around -3%. The negative sign indicates a favorable result, which means that the total drag was 3% less than the sum of the individual drag on the two plates in isolation. The report also concluded that the disruption of the boundary-layer was limited to a space in the juncture about 2.6 times the width of the strut along one plate and

0.9 times the width of the strut along the perpendicular plate. The findings of this study show that it is possible to isolate regions within a flow that contribute most to the interference drag.

The field of competitive cycling also has researched interference drag of multiple bicyclists. “Drafting” is a phenomenon used by two or more cyclists to increase their aerodynamic efficiency. In general, drafting is the term used to describe the phenomena that occurs when two bluff objects are placed in tandem in a free stream flow, such that the trailing object experiences a reduction in aerodynamic drag. In 2015, Barry et al. examined the effects of the riding position of a leading cyclist on three trailing cyclists.[11] The data was gathered in a wind tunnel environment. Four cyclists in generic riding positions with identical bicycles and teardrop shaped helmets were placed 4.7 inches apart in a wind tunnel test section. The most robust finding showed that changing the geometry of the trailing rider, by either changing the head and elbow positions, affects the upstream riders both positively and negatively. Positive or negative variations in interference drag were attributed to individual differences in athlete body shape during tests. The authors mentioned that performing CFD studies of interference drag due to geometric changes was too computationally expensive for multiple riders. A second finding suggested that decreasing the frontal area of the lead rider, by lowering the head position, increased the drag of the rider immediately behind. This is expected since the trailing rider is exposed to more of the free stream flow. Barry’s study on interference drag between obstacles (cyclists) mounted on a wall (the road) is geometrically similar but not physically similar to the problem studied in this thesis. All tests were conducted at an estimated Mach number

of 0.05 and a Reynolds number of approximately 2 $x10^6$ (based on the average height of the cyclists). The tested regime is not readily applicable to aeronautical fields.

A study on refueling tankers, by Dogan, Blake and Haag examined the aerodynamic interaction of two large aircraft in proximity to each other during refueling flight tests. [12] The interference effect is noticeable enough to alter the path of the vehicles and cause several handling problems for large, sluggish aircraft, such as the C-17, B-2 and a KC-125. The paper considers several flow mechanisms that cause this interference effect including the upwash from the trailing aircraft or the presence of the trailing aircraft acting as a new boundary and affecting the flow around the leading aircraft. While the Mach number and Reynolds number of Dogan's study are similar to the focus of this thesis, Dogan's study primarily investigates the mechanisms that cause interference and not ways to reduce interference drag.

Interference drag has also been studied at larger scales in urban environments and mountainous terrain. In the paper "Surface pressure distribution and pressure drag on mountains," Emeis calculated surface pressure distribution on mountains using a numerical model[13]. Among the many scenarios analyzed, the most relevant to this thesis is the steady-state pressure drag on two mountains, characterized by a sinusoidal wave. The distance between two mountains was varied from a fraction of the mountain's wavelength to multiple wavelengths apart. In the paper, the parameter Fr_2 is specifically defined to represent a non-dimensionalized spacing between mountains.

Emesis studied total drag, but it is possible to infer the role of interference drag from the results. The data in Figure 10 shows that the total drag on the mountain varied

with the separation distance and there exists a distance where the drag is a minimum (at $Fr_2 = 4.5$).

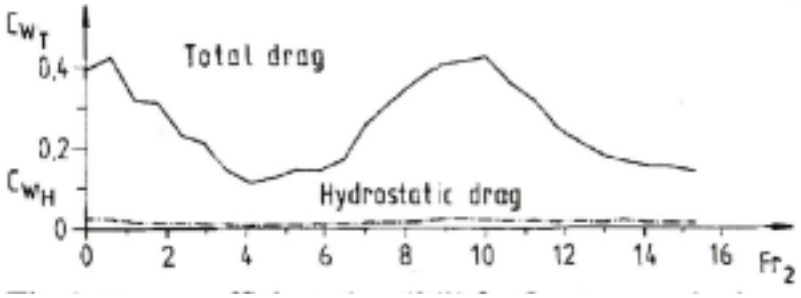

Figure 10. Drag coefficient vs Froude number for obstacles at various distances. [13]

Summary of Literature Review

Table 1 presents a comparison of the Mach and Reynolds number regimes examined in the studies that were reviewed. While none of the studies are physically similar to the problem analyzed in this paper, their results confirm that there exist physical parameters which engineers can control to potentially minimize interference drag in aerospace applications.

Author	Year	Description	Mach No.	Reynolds No.
Biermann and Herrnstein	1933	Struts in various combinations	0.1*	1 x 10^5 to 4 x 10^5
Hoerner	1965	Single wall-mounted object	0.25 to 0.58	2.5 x 10^6 to 4.8 x 10^6
NASA	1984	Two struts in a juncture	0.04*	9.9 x 10^5
Barry et al	2015	Tandem Cyclists in a wind tunnel	0.05*	2 x10^6
Dogan et al	2013	Aerial refueling	0.6	2 x 10^{8*}
Emeis		Two mountains at varying distances	0.02*	5x 10^{10*}
Ramekar	2018	Two hemispheres mounted on a wall (this thesis)	0.44 to 0.48	1.9 x $10^{7\dagger}$

Table 1. Mach and Reynolds regimes examined in the literature review.

* Value is not explicitly stated in reference paper and is estimated based on published data.
† Reynolds number is the average of all the cases studied in paper and reference length is the mean aerodynamic chord of a King Air 300 aircraft

Useful concepts from this literature review can be condensed into four points. First, for a given Reynolds number, the interference drag can be affected by changing the geometry of one or both objects. The fineness ratio and thickness ratio are two parameters used to categorize those geometric changes.

Second, the interference drag can be affected by changing the distance between two or more objects. Hoerner's wind tunnel data and Emeis' computational data indicate that there exists a distance where the interference drag is a minimum. The NASA study of plates in a juncture reveals that the boundary-layer disruptions, that give rise to interference drag, occur in a confined area. This suggests that the distance where interference drag is minimized is on the same scale as the length of the objects. The separation distance for minimum drag can be non-dimensionalized by using an object's characteristic length.

Third, the incoming flow conditions changes both the interference drag and parasitic drag simultaneously. The literature suggests that there are instances where there is a net decrease in total drag even though the parasitic component increases. It is important, therefore, to consider total drag instead of solely interference drag when studying the effects of Mach and Reynolds number.

Finally, the interference drag can be quantified using a sensitivity ratio and it will be used to present the results in this paper.

Chapter 3: Problem Definition

Introduction

This chapter assesses the operating environment of Intelligence, Surveillance and Reconnaissance (ISR) aircraft in order to establish initial conditions and boundary conditions of the problem. This chapter also examines some external modifications made to aircraft in order to establish the size and shape of the obstacles needed for the study. Additionally, this chapter presents the assumptions made to implement the Navier-Stokes equations at high Reynolds numbers. All dimensions and quantities in this paper are in English units, as American aircraft design engineers use English measurement systems.

King Air 300 and Common Modifications

The King Air 300 (KA300) (Figure 11), is a low-wing, twin-turboprop aircraft, and is often heavily modified for ISR missions. The modified versions of the KA300 include the C-12 Huron (Figure 12), onto which several antennas are added on the top and bottom surfaces. Another popular modification to a KA300 is the installation of an infrared camera underneath the aircraft (Figure 13) measuring 15 to 20 inches in diameter, depending on the camera model. Another common modification is a long aerodynamic fairing, or a pod, which is installed on the aircraft's underside (Figure 14).

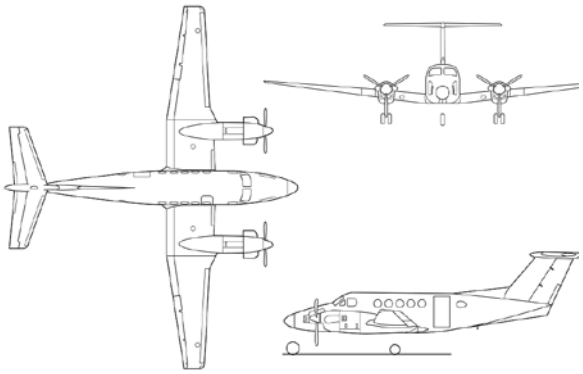

Figure 11. 3-view drawing of a KA300 aircraft.

Figure 12. Photograph of a C-12 Huron.

Figure 13. An MX-18 infrared camera modification underneath the aircraft. [14]

Figure 14. A modified KA300 with a pod installed on the belly.

International Standard Atmosphere

The initial and boundary conditions in this study are determined by the typical flight conditions of a KA300. According to the KA300's aircraft flight manual (AFM),[15] the highest cruising altitude allowable with one engine inoperative is 25,000 feet. In order to determine the properties of air at 25,000 feet above mean sea level, aviation engineers and pilots use the international standard atmosphere (ISA) model. The ISA standard is defined by the International Civil Aviation Organization and it states the conditions of a fixed representation of the earth's atmosphere. [16]

By using ISA conditions, measurements from tests conducted at different times can be compared without introducing variations due to local weather phenomena. The following equations provide ISA pressure, temperature and density as a function of altitude:

$$\rho = \rho_0(1 - 6.873 \times 10^{-6}\, z)^{4.26} \quad \text{slug/ft}^3 \qquad \textit{Eq. 3}$$

$$P = P_0(1 - 6.873 \times 10^{-6}\, z)^{5.26} \quad lb \cdot ft^2 \qquad \textit{Eq. 4}$$

$$T = T_0 - 3.57 \times 10^{-3}\, z \ ^\circ F \qquad \textit{Eq. 5}$$

In Eq. 3 to Eq. 5 , z is the altitude in ft; ρ_0 is the density at sea level, which is 0.002378 $slug/ft^3$; $P_0$is the pressure at sea level, which is 2116.22 $lb \cdot ft^2$; and T_0 is the temperature at sea level, which is 59 $^\circ F$. Figure 15 shows how these properties vary with altitude and these properties will be used to define the initial and boundary conditions of the problem.

Additionally, the dynamic viscosity of air at a certain height in the atmosphere is calculated according to Sutherland's law,[17] where T is the temperature in Fahrenheit at that height.

$$\mu = 3.58 \times 10^{-7} \left(\frac{T}{151.66} - 1.68\right)^{3/2} \frac{383.55}{1.8T + 349} \ psf \cdot s \qquad \textit{Eq. 6}$$

Navier-Stokes Equations

Computational Fluid Dynamics (CFD) analysis provides insight into a flow behavior without having to recreate, test and measure it in a laboratory. CFD analysis is the solution of the governing laws of fluid motion by specially developed algorithms that can be automated on computers. A complex set of partial differential equations (PDEs), which are defined over a spatial domain, is solved on discrete volume elements in space,

represented by a mesh. The equations in the rest of this chapter give the mathematical basis for computer codes used in this study.

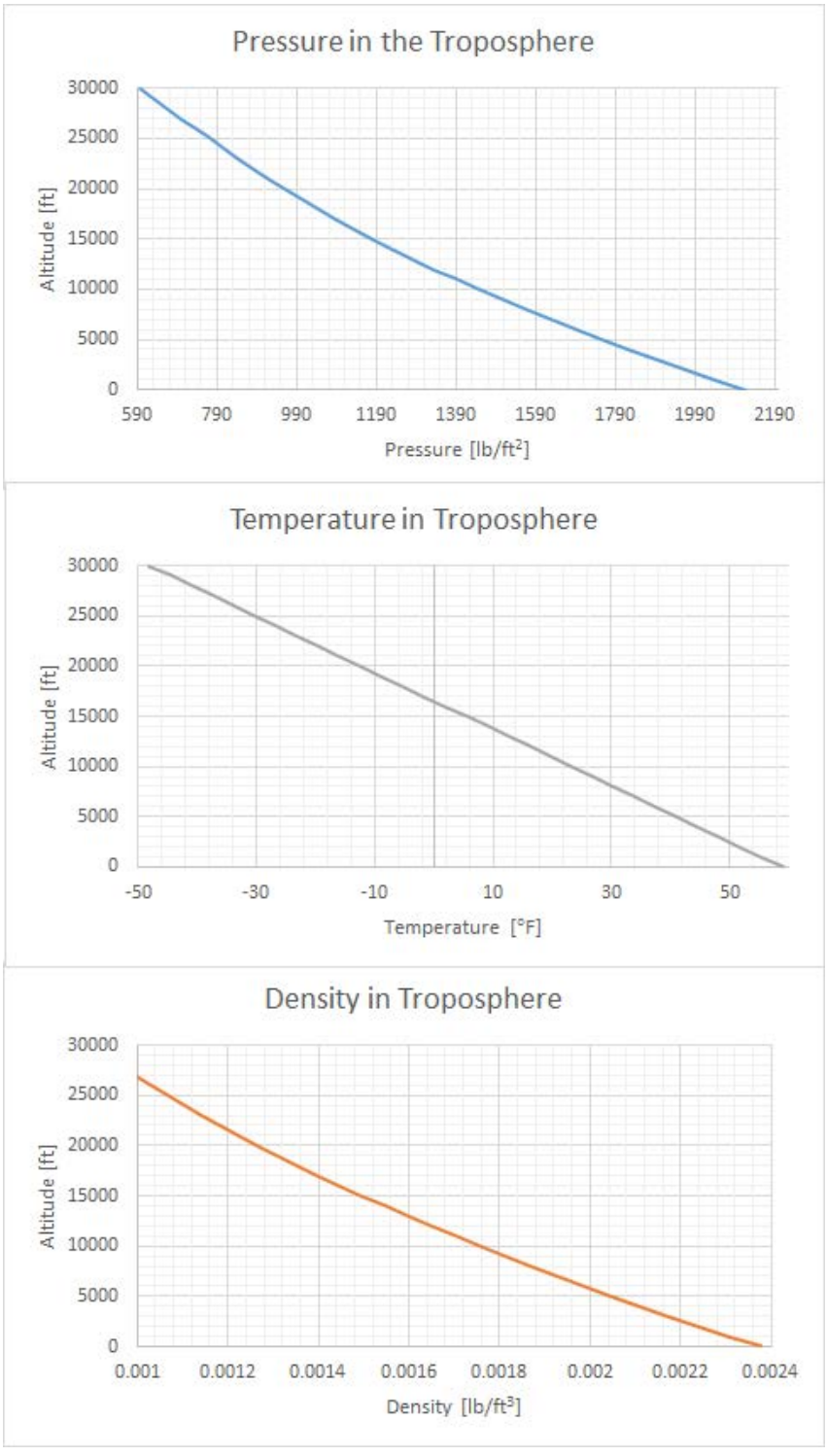

Figure 15. Atmospheric properties at various altitudes.

The Navier-Stokes equations represent the motions of fluids and are derived from the basic principles of conservation of mass, momentum and energy. The derivation of these equations from conservation laws is present in most fluid dynamics books, notably *Fundamental of Aerodynamics* by John D. Anderson.[18] The full set of three-dimensional Navier-Stokes equations is shown below:

$$\frac{\partial \rho}{\partial t} + \nabla \cdot (\rho \boldsymbol{U}) = 0 \qquad \textit{Eq. 7}$$

$$\frac{\partial (\rho \boldsymbol{U})}{\partial t} + \nabla \cdot (\rho \boldsymbol{U}\boldsymbol{U}) + \nabla P + \nabla \cdot \hat{\tau} = 0 \qquad \textit{Eq. 8}$$

$$\frac{\partial (E)}{\partial t} + \nabla \cdot \big((E + P)\boldsymbol{U}\big) + \nabla \cdot (U \cdot \hat{\tau}) + \nabla \cdot (K \nabla T) = 0 \qquad \textit{Eq. 9}$$

$$\hat{\tau} = \rho \nu \left(\frac{2}{3} (\nabla \cdot \boldsymbol{U}) \hat{I} - (\nabla \boldsymbol{U}) - (\nabla \boldsymbol{U}) \right) \qquad \textit{Eq. 10}$$

$$P = \rho R T \qquad \textit{Eq. 11}$$

$$E = \frac{P}{(\gamma - 1)} + \frac{\rho U^2}{2} \qquad \textit{Eq. 12}$$

The equations model nonreactive, continuous, viscous and compressible motion of fluids in space. Body forces, such as gravity, are not included here. In the Navier-Stokes equations, the unknown variables are pressure (p) density (ρ), temperature (T), the three components of velocity (u,v,w), and six components in the stress tensor($\tau_{xx}, \tau_{yy}, \tau_{zz}, \tau_{xy}, \tau_{xz}, \tau_{yz}$). Time ($t$) and spatial coordinates (x, y, z) are the independent variables. A first-order partial derivative in time and a second-order partial derivative in space model the transport and diffusion processes, respectively.

The Mach number, M, (Eq. 13), is often used to determine whether the compressible behavior of the fluid can be ignored. For reference, the Mach number of a KA300 aircraft traveling at 450 ft/s, at sea level is 0.40.

$$M = \frac{V}{a} = \frac{450\frac{ft}{s}}{\sqrt{\rho RT}} \qquad \textit{Eq. 13}$$

The Reynolds number, Re, is often used to indicate whether the flow is laminar or turbulent. The Reynolds number is the ratio of viscous to inertial forces, and a high Reynolds number signifies a dominance of inertial forces (Eq. 14).

$$Re = \frac{\rho VL}{\mu} \qquad \textit{Eq. 14}$$

The characteristic length, L, is 5.4 ft, which is the mean aerodynamic chord on a KA300 wing. At sea level, the Reynolds number is 1.6 x 10^7 and the flow is therefore turbulent.

Solving the Navier Stokes equation for high-Reynolds number flows requires a fine mesh to accurately capture information on all scales, but this can be time consuming. Direct numerical simulation (DNS) is an approach for solving the Navier-Stokes equations in which all scales relevant to the physics are resolved. The computational cost of finding the numerical solution can be shown to scale with the Re^3.[19] The cost of solving the Navier-Stokes equations for very high Reynolds numbers using DNS techniques is usually not possible.

RANS Approximation

To circumvent the costs involved when solving the Navier-Stokes equations by DNS techniques, the following categories of approximations can be used: (1) Large Eddy Simulations (LES), which computes large scale properties and models the small scale properties; or (2) Reynolds Averaged Navier-Stokes (RANS), which compute the average of flow-field properties. For flows of practical engineering interest, e.g., flows over airplanes, RANS assumptions are usually used.[20]

The RANS equations calculate mean flow properties. These equations are derived from the Navier-Stokes equations by decomposing the instantaneous, dependent variables into a time-fluctuating (unsteady) component (signified with an apostrophe) and a mean (steady) component (signified with a bar). To derive the RANS equations, the Reynolds decomposition is applied to the mass, momentum and energy conservation equations. Eq. 15 to Eq. 18 are substituted into the momentum equation, Eq. 8, which results in Eq. 19.

$$\boldsymbol{U} = \bar{U}_\iota + u_i' \qquad \textit{Eq. 15}$$

$$P = \bar{P} + p' \qquad \textit{Eq. 16}$$

$$T = \bar{T} + T' \qquad \textit{Eq. 17}$$

$$\rho = \bar{\rho} + \rho' \qquad \textit{Eq. 18}$$

$$(\bar{\rho} + \rho')\left(\frac{\partial(\bar{U}_\iota + u_i')}{\partial t} + \frac{\partial\left((\bar{U}_\iota + u_i')(\bar{U}_\iota + u_i')\right)}{\partial x_j}\right) = \frac{\partial}{\partial x_j}\left(\mu\frac{\partial(\bar{U}_\iota + u_i')}{\partial x_j}\right) - \frac{\partial(\bar{P} + p')}{\partial x_i} \qquad \textit{Eq. 19}$$

Distribution of the terms in Eq. 19 results in Eq. 20:

$$(\bar{\rho}+\rho')\left(\frac{\partial(\bar{U}_\iota)}{\partial t}+\frac{\partial(u_i')}{\partial t}+\frac{\partial\left(\bar{U}_J\bar{U}_\iota\right)}{\partial x_j}+\frac{\partial\left(\bar{U}_J u_i'\right)}{\partial x_j}+\frac{\partial\left(u_j'\bar{U}_\iota\right)}{\partial x_j}+\frac{\partial\left(u_j'u_i'\right)}{\partial x_j}\right)$$
$$=\mu\left(\frac{\partial^2(\bar{U}_\iota)}{\partial x_j^2}+\frac{\partial^2(u_i')}{\partial x_j^2}\right)-\frac{\partial\bar{P}}{\partial x_i}-\frac{\partial p'}{\partial x_i} \qquad \textit{Eq. 20}$$

To further simplify Eq. 20, the mean properties given by Eq. 21 to Eq. 28 are used. These substitutions can be made since the average of the fluctuating term by definition is zero, and the average of a mean quantity is simply the mean itself.

$$\overline{u_\iota'}=0 \qquad \textit{Eq. 21}$$

$$\overline{p'}=0 \qquad \textit{Eq. 22}$$

$$\overline{\rho'}=0 \qquad \textit{Eq. 23}$$

$$\overline{\bar{U}}=\bar{U} \qquad \textit{Eq. 24}$$

$$\overline{\bar{P}}=\bar{P} \qquad \textit{Eq. 25}$$

$$\overline{\bar{\rho}}=\bar{\rho} \qquad \textit{Eq. 26}$$

$$\overline{\bar{U}_J u_\iota'}=0 \qquad \textit{Eq. 27}$$

$$\overline{u_j'\bar{U}_\iota}=0 \qquad \textit{Eq. 28}$$

Taking the average of Eq. 20 and substituting Eq. 21 through Eq. 28 into the resultant provides the following:

$$\bar{\rho}\left(\frac{\partial(\bar{U}_\iota)}{\partial t}+\frac{\partial\left(\bar{U}_J\bar{U}_\iota\right)}{\partial x_j}+\frac{\partial\left(\overline{u_j'u_\iota'}\right)}{\partial x_j}\right)=\mu\frac{\partial^2(\bar{U}_\iota)}{\partial x_j^2}-\frac{\partial\bar{p}}{\partial x_i} \qquad \textit{Eq. 29}$$

Rearranging Eq. 29 results in the RANS equation (Eq. 30).

$$\bar{\rho}\frac{\partial(\bar{U}_\iota)}{\partial t}+\bar{\rho}\frac{\partial(\bar{U}_\iota)}{\partial x_j}=\frac{\partial}{\partial x_j}\left(\overline{\rho u_j'u_\iota'}+2\mu\frac{\partial(\bar{U}_\iota)}{\partial x_j}-\bar{p}\right) \qquad \textit{Eq. 30}$$

The term $\rho\overline{u_\iota' u_j'}$ is the Reynolds stress. Because the Navier-Stokes equations are non-linear, these velocity fluctuations still appear in the RANS equation. The relation of fluctuating quantities to the mean quantities is known as the turbulence closure problem. The Reynolds stress is related to the mean quantities, $\overline{U}_\iota$ using additional equations which constitute a turbulence model.

Turbulence Models

Many turbulence models have been developed for specific problems. The three models are discussed in this section, the Spallart-Allmaras, *k-ε,* and *k-ω,* have been used in compressible aerospace applications.

All three models are based on the Boussinesq eddy-viscosity assumption, which relates the Reynolds stress to the eddy viscosity, μ_t, and the mean rate of deformation, S_{ij} (Eq. 31).

$$\rho\overline{u_\iota u_J} = 2\mu_t S_{ij} - \frac{2}{3}\rho k\delta_{ij} \qquad \textit{Eq. 31}$$

$$where\ S_{ij} = \frac{1}{2}\left(\frac{\partial \overline{U}_\iota}{\partial x_j} + \frac{\partial \overline{U}_J}{\partial x_i}\right) - \frac{1}{3}\frac{\partial \overline{U_k}}{\partial x_k}\delta_{ij} \qquad \textit{Eq. 32}$$

$$k = \frac{1}{2}\left(\overline{(u_1')^2} + \overline{(u_2')^2} + \overline{(u_3')^2}\right) \qquad \textit{Eq. 33}$$

The Boussinesq eddy-viscosity assumption has no physical basis and the relationship is used because the dimensions of the parameters match. Mathematics requires the $\frac{2}{3}\rho k\delta_{ij}$ term (Eq. 31) for the 2-equation turbulence models, and the δ_{ij} is the kronecker delta function. Each of the three turbulence models defines the eddy viscosity differently. The advantages and limitations of each turbulence model are explained below.

Spallart-Allmaras

The Spallart-Allmaras turbulence model is based on the Boussinesq eddy viscosity assumption and is a one-equation model that introduces only one new variable, $\tilde{\nu}$, to achieve closure. It defines the eddy viscosity as

$$\mu_T = \rho\tilde{\nu}f_{v1} \qquad \textit{Eq. 34}$$

where ρ the local density. The $\tilde{\nu}$, and f_{v1} terms are defined using numerous auxiliary equations and constants shown below.

$$\frac{\partial\tilde{\nu}}{\partial t} + u_j\frac{\partial\tilde{\nu}}{\partial x_j} = c_{b1}(1-f_{t2})\hat{S}\tilde{\nu} - \left[c_{w1}f_w - \frac{c_{b1}}{\kappa^2}f_{t2}\right]\left(\frac{\tilde{\nu}}{d}\right)^2 + \frac{1}{\sigma}\left[\frac{\partial}{\partial x_j}\left((\nu+\tilde{\nu})\frac{\partial\tilde{\nu}}{\partial x_j}\right) + c_{b2}\frac{\partial\tilde{\nu}}{\partial x_i}\frac{\partial\tilde{\nu}}{\partial x_i}\right] \qquad \textit{Eq. 35}$$

$$f_{v1} = \frac{\chi^3}{\chi^3+c_{v1}^3}, \text{where } \chi = \frac{\tilde{\nu}}{\nu},\ c_{v1} = 7.1 \qquad \textit{Eq. 36}$$

$$f_{v2} = 1 - \frac{\chi}{1+\chi f_{v1}} \qquad \textit{Eq. 37}$$

$$f_{t2} = c_{t3}\exp(c_{t4}\chi^2)\ \text{, where } c_{t3} = 1.2\text{ , } c_{t4} = 0.5 \qquad \textit{Eq. 38}$$

$$f_w = g\left[\frac{1+c_{w3}^6}{g^6+c_{w3}^6}\right]^{1/6}\ \text{, where } c_{w3} = 2 \qquad \textit{Eq. 39}$$

$$g = r + c_{w2}(r^6 - r), \text{where } c_{w2} = 0.3 \qquad \textit{Eq. 40}$$

$$r = \min\left(\frac{\tilde{\nu}}{\hat{S}\kappa^2 d^2}, 10\right)\text{, where } \kappa = 0.41 \qquad \textit{Eq. 41}$$

$$\hat{S} = \Omega + \frac{\nu}{\kappa^2 d^2}f_{v2} \qquad \textit{Eq. 42}$$

$$\Omega = \sqrt{2W_{ij}W_{ij}} \qquad \textit{Eq. 43}$$

$$W_{ij} = \frac{1}{2}\left(\partial U_i/\partial x_j - \partial U_j/\partial x_i\right) \qquad \textit{Eq. 44}$$

$$c_{w1} = \frac{c_{b1}}{\kappa^2} + \frac{1+c_{b2}}{\sigma}, \text{where } c_{b1} = 0.1355, c_{b2} = 0.622, \sigma = 0.622 \qquad \textit{Eq. 45}$$

Eq. 35 was devised to model the transport, production, diffusion and to remove kinematic eddy turbulent viscosity in the system.[21] Spallart and Allmaras tested and calibrated this model on a transonic airfoil, and their model is often used for compressible aerospace applications. It performs well for boundary-layers with adverse pressure gradients, but not when the flow changes abruptly from wall-bounded to free shear-flows, e.g., when exhaust air exits a nozzle.

k- ϵ Model

The k-ϵ model is based on the Boussinisq eddy viscosity assumption.[22] In this model, two variables—the turbulent dissipation, ϵ, and the turbulent kinetic energy, *k*—are introduced to achieve closure and to define the eddy viscosity μ_t.

$$\mu_t = \rho C_\mu \frac{k^2}{\epsilon} \qquad \textit{Eq. 46}$$

$$C_\mu = 0.09 \qquad \textit{Eq. 47}$$

The two new variables are accompanied by two new equations, Eq. 48 and Eq. 49, and several constants, Eq. 50.

$$\frac{d}{dt}(\rho k) + \frac{\partial}{\partial x_j}(\rho k U_j) = \frac{\partial}{\partial x_j}\left[(\mu + \mu_T/\sigma_k)\frac{\partial k}{\partial x_j}\right] + 2\mu_T S_{ij} S_{ij} - \rho\epsilon \qquad \textit{Eq. 48}$$

$$\frac{\partial(\rho\epsilon)}{\partial t} + \frac{\partial(\rho\epsilon u_i)}{\partial x_i} = \frac{\partial}{\partial x_j}\left[\left(\mu + \frac{\mu_t}{\sigma_\epsilon}\right)\frac{\partial \epsilon}{\partial x_j}\right] + C_{1\epsilon}\frac{\epsilon}{k}2\mu_t S_{ij} S_{ij} - C_{2\epsilon}\rho\frac{\epsilon^2}{k} \qquad \textit{Eq. 49}$$

$$\sigma_k = 1.00 \qquad \sigma_\epsilon = 1.30 \qquad C_{1\epsilon} = 1.44 \qquad C_{2\epsilon} = 1.92 \qquad \textit{Eq. 50}$$

Eq. 48 and Eq. 49 are partial differential equations (PDEs) which model processes observed in fluids such as diffusion and transport of fluid elements. The k-ϵ model

performs well away from walls in free shear-flows and large wakes, but not when a flow contains large adverse-pressure gradients.[23]

In an RNG version of the k-ϵ model, the constant $C_\mu$has a value of 0.0845. The RNG k-ϵ model's limitations are the same as those of the standard k-ϵ model, though some users claim it offers improved accuracy in rotating flows, such as rotating cavities. Because of this, the RNG k-ϵ model is often used for indoor air simulations.[24]

Another version of the k-ϵ turbulence model is the realizable k-ϵ model. The constant C_μ is defined according to Eq. 51 and a few additional equations.

$$C_\mu = \frac{1}{A_0 + A_s \frac{kU^*}{\epsilon}} \qquad \textit{Eq. 51}$$

$$A_0 = 4.04 \qquad \textit{Eq. 52}$$

$$A_s = \sqrt{6}\cos\left(\frac{1}{3}\cos^{-1}\sqrt{6}W\right) \qquad \textit{Eq. 53}$$

$$W = \frac{S_{ij}S_{jk}S_{ki}}{\left(S_{ij}S_{ij}\right)^{3/2}} \qquad \textit{Eq. 54}$$

$$\widetilde{\Omega}_{ij} = \overline{\Omega}_{ij} - 3\epsilon_{ijk}\omega_k \qquad \textit{Eq. 55}$$

The quantity $\overline{\Omega}_{ij}$ is the mean rate of rotation tensor viewed in the rotating reference frame and ω_k is the angular velocity. The equation for the turbulent dissipation rate is also modified to Eq. 56.

$$\frac{\partial}{\partial t}(\rho\epsilon) + \frac{\partial}{\partial x_i}(\rho\epsilon u_i) = \frac{\partial}{\partial x_j}\left[\left(\mu + \frac{\mu_t}{\sigma_\epsilon}\right)\frac{\partial \epsilon}{\partial x_j}\right] + \rho C_1 S\epsilon - C_2\rho\frac{\epsilon^2}{k+\sqrt{\nu\epsilon}} + C_{1\epsilon}\frac{\epsilon}{k}C_{3\epsilon}P_b + S_\epsilon \qquad \textit{Eq. 56}$$

$$C_1 = max\left[.43\frac{\eta}{\eta+5}\right] \qquad \textit{Eq. 57}$$

$$\eta = S\frac{k}{\epsilon} \qquad \textit{Eq. 58}$$

$$S = \sqrt{2S_{ij}S_{ij}} \qquad \textit{Eq. 59}$$

$$\sigma_k = 1.0 \qquad \sigma_\epsilon = 1.2 \qquad C_{1\epsilon} = 1.44 \qquad C_2 = 1.9 \qquad \textit{Eq. 60}$$

This version of the model is the most computationally expensive version of all the k- ϵ models. According to studies by Marzouk,[25] it is also unable to predict radial velocity well. However, it can predict flows in boundary-layer regions with better accuracy than the original k-ε model.

k-ω Model

The *k-ω* turbulence model is a two-equation model based on the Boussinesq eddy viscosity assumption. For this model, Eq. 61 defines the eddy viscosity:

$$\mu_T = \frac{k}{\omega} \qquad \textit{Eq. 61}$$

Two new variables — the specific dissipation rate of energy per unit volume in time, ω, and the turbulent kinetic energy, k — are introduced here, which require Eq. 62 and Eq. 63 to achieve closure:

$$\frac{dk}{dt} + U_j\frac{\partial k}{\partial x_j} = \tau_{ij}\frac{\partial U_i}{\partial x_j} - \beta^* k\omega + \frac{\partial}{\partial x_j}\left[(\nu + \nu_T\sigma_k)\frac{\partial k}{\partial x_j}\right] \qquad \textit{Eq. 62}$$

$$\frac{\partial(\rho\omega)}{\partial t} + \frac{\partial\left(\rho u_j\omega\right)}{\partial x_j} = \frac{\gamma\omega}{k}P - \beta\rho\omega^2 + \frac{\partial}{\partial x_j}\left[\left(\mu + \sigma_\omega\frac{\rho k}{\omega}\right)\frac{\partial\omega}{\partial x_j}\right] + \frac{\rho\sigma_d}{\omega}\frac{\partial k}{\partial x_j}\frac{\partial\omega}{\partial x_j} \qquad \textit{Eq. 63}$$

$$\alpha = \frac{5}{9} \qquad \beta = \frac{3}{40} \qquad \beta^* = \frac{9}{100} \qquad \sigma = \frac{1}{2} \qquad \sigma^* = \frac{1}{2}$$

Like the *k*-ϵ PDE, the *k*-ω PDE contains mathematical expressions known to model observable fluid motion, like unsteadiness, transport and diffusion.[26] This PDE has no turbulence production term, which reflects Kolmogorov's hypothesis that specific dissipation does not occur at large scales with large eddy motions but occurs only at the small scales of the flow. Nor does this version of the *k*-ω model have a dissipation term; the model therefore works best when applied to high Reynolds number flows in which transport phenomena dominate over diffusion.

Wilcox (1988) and Speziale (1990) introduced another version of the *k*-ω model which includes production and cross-diffusion terms into the *k*-ω equation to capture diffusion physics and predict flows near boundary-layers and walls. The coefficients for the newer models were found empirically and have been updated over the decades based on experimental data. The latest closure coefficients can be found in Wilcox (2008).[5]

Wall Functions

CFD uses a set of equations, called wall functions, to obtain boundary conditions for the Navier-Stokes equations in the near-wall region. The advantage of using wall functions is in the computational savings they provide, since the mesh in the near-wall region can be coarse and it is not necessary resolve the boundary-layer. However, the coarseness of the mesh in the near wall region has a limit, which is expressed by a $y+$ value.

To use wall functions, assumptions about the velocity distribution in the boundary-layer are expressed using a dimensionless velocity, $u+$, and a dimensionless distance parameter, $y+$.

$$y^+ = \frac{yu_\tau}{\nu} \qquad \textit{Eq. 64}$$

$$u^+ = \frac{u}{u_\tau} \qquad \textit{Eq. 65}$$

$$u_\tau = \sqrt{\frac{\tau_w}{\rho}} = \sqrt{\frac{\mu}{\rho}\left(\frac{\partial u}{\partial y}\right)_{y=0}} \qquad \textit{Eq. 66}$$

Eq. 66 defines the friction velocity, u_τ where τ_w is the shear force, μ is the dynamic viscosity of air, and $\left(\frac{\partial u}{\partial y}\right)_{y=0}$ is the velocity gradient at the wall.

The behavior of $u+$ in a boundary-layer is divided into three regions:

1. the viscous sublayer;
2. the buffer layer; and
3. the log-law region.

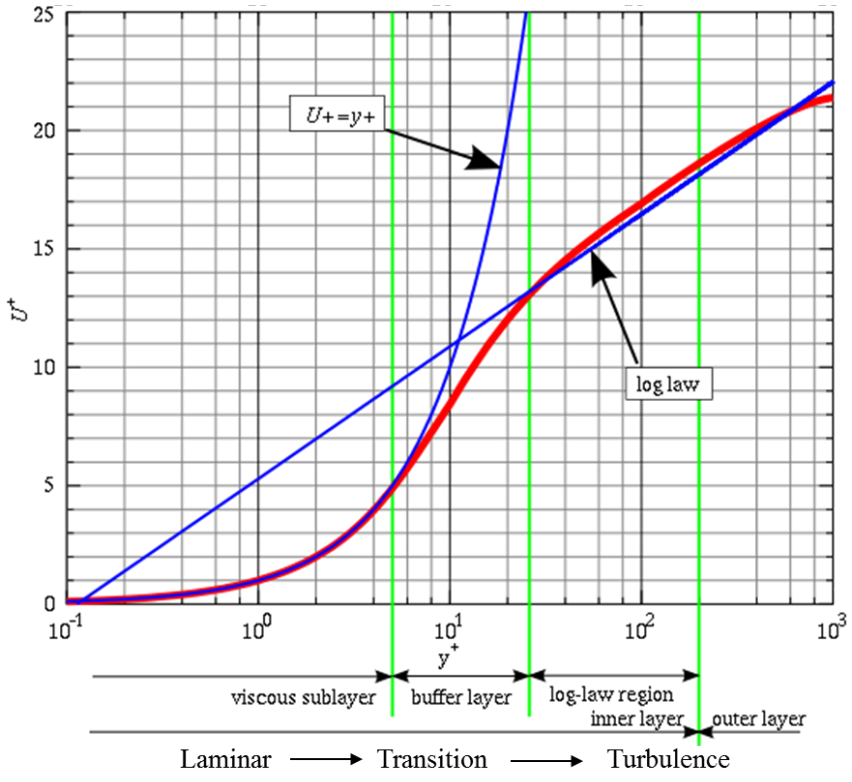

Figure 16. Boundary-layer y+ and u+ distribution.

Using experimental data, Eq. 67 and Eq. 68 state an empirical relationship between $u+$ and $y+$:

$$u^+ = y^+ \text{ for } y^+ < 5 \qquad \textit{Eq. 67}$$

$$u^+ = \frac{1}{\kappa}\ln y^+ + C^+ \text{ for } y^+ > 30, \qquad \textit{Eq. 68}$$

$$C^+ \approx 5.1 \text{ and } \kappa \approx .41 \qquad \textit{Eq. 69}$$

In the buffer layer, for $5 < y^+ < 30$, CFD codes use functions to "blend" the gap between the viscous layer and log-law region. Some wall functions have slope discontinuities between the laminar and log-law regions. In this study, however, the buffer layer is represented with a "two layer all $y+$ wall treatment," which smoothly connects the dimensionless velocity in the viscous sublayer to that in the log-law region.[27] According to the wall function this thesis implements, the dimensionless distance of the centroid of the cell closest to the wall should be between 30 and 50 for accurate results. (Chapter 4 revisits this requirement.) Once the target $y+$ value is established through a mesh of appropriate coarseness, the $u+$ and velocity can be calculated in the near wall region with no need to resolve the entire boundary-layer.

Discretizing and Finite Differences

Discretization means that a function defined continuously over a domain is converted to an algebraic expression defined over a grid. The discretization of the Navier-Stokes equation allows implementation of a numerical solution on a computer. To illustrate, a first- and second-order differential operators, similar to the terms in the Navier-Stokes equations, are discretized over a 2D domain. A similar concept can also be applied to a 3D domain.

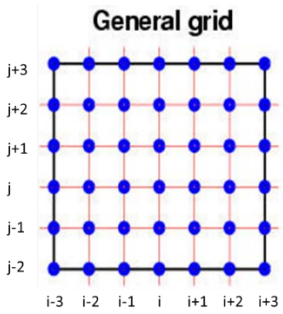

Figure 17. A 2D grid over which continuous function are discretized.

The grid contains nodes identified by (i, j) coordinates. Each node is assigned a property, like velocity, which is annotated as $u_{i,j}$. The velocity on two adjacent nodes, (i, j) and ($i+1$, j), can be related to each other using a Taylor series expansion (Eq. 70):

$$u_{i+1,j} = u_{i,j} + \left(\frac{\partial u}{\partial x}\right)_{i,j} \Delta x - \left(\frac{\partial^2 u}{\partial x^2}\right)_{i,j} \frac{\Delta x^2}{2!} + \left(\frac{\partial^3 u}{\partial x^3}\right)_{i,j} \frac{\Delta x^3}{3!} - \cdots \qquad \textit{Eq. 70}$$

Rearranging Eq. 70 for the first-order partial differential operator, $\left(\frac{\partial u}{\partial x}\right)_{i,j}$, results in Eq. 71.

$$\left(\frac{\partial u}{\partial x}\right)_{i,j} = \underbrace{\frac{u_{i+1,j} - u_{i,j}}{\Delta x}}_{\text{Finite difference representation}} + \underbrace{O(\Delta x)}_{\text{Truncation error}} \qquad \textit{Eq. 71}$$

$$\text{where, } O(\Delta x) = -\left(\left(\frac{\partial^2 u}{\partial x^2}\right)_{i,j} \frac{\Delta x^2}{2!} + \left(\frac{\partial^3 u}{\partial x^3}\right)_{i,j} \frac{\Delta x^3}{3!} + \cdots\right) \qquad \textit{Eq. 72}$$

$$\text{and } \Delta x = x_{i+1,j} - x_{i,j} \qquad \textit{Eq. 73}$$

The $\left(\frac{\partial u}{\partial x}\right)_{i,j}$ term represents the velocity transport in the *x*-direction which can now be related to an algebraic equivalent (with a finite error). It should be noted the algebraic equivalent shown here is not unique to the operator because the same continuous operator can be discretized using different nodes, (*i, j*) and (*i-1, j*), shown in Eq. 75. This particular expansion is called a backward-biased scheme.[28]

$$u_{i-1,j} = u_{i,j} - \left(\frac{\partial u}{\partial x}\right)_{i,j} \Delta x + \left(\frac{\partial^2 u}{\partial x^2}\right)_{i,j} \frac{\Delta x^2}{2!} - \left(\frac{\partial^3 u}{\partial x^3}\right)_{i,j} \frac{\Delta x^3}{3!} + \cdots \qquad \textit{Eq. 74}$$

$$\boxed{\left(\frac{\partial u}{\partial x}\right)_{i,j} = \frac{u_{i,j} - u_{i-1,j}}{\Delta x} + O(\Delta x)} \qquad \textit{Eq. 75}$$

Another alternative is the central difference scheme which has the advantage of having a smaller truncation error (Eq. 77).

$$u_{i+1,j} - u_{i-1,j} = 2\left(\frac{\partial u}{\partial x}\right)_{i,j} \Delta x + 2\left(\frac{\partial^3 u}{\partial x^3}\right)_{i,j} \frac{\Delta x^3}{3!} + \cdots \qquad \textit{Eq. 76}$$

$$\boxed{\left(\frac{\partial u}{\partial x}\right)_{i,j} = \frac{u_{i+1,j} - u_{i-1,j}}{2\Delta x} + O(\Delta x^2)} \qquad \textit{Eq. 77}$$

Furthermore, a PDE can be discretized with different orders of accuracy, which generally involve sampling more grid points. For example, a second-order partial differential equation, which represents the diffusion process in the Navier-Stokes equations, can be written as a central finite difference of fourth-order accuracy (Eq. 78) using information at five nodes: (*i+2, j*), (*i+1, j*), (*i, j*), (*i-1, j*), (*i-2, j*).

$$\left(\frac{\partial^2 u}{\partial x^2}\right)_{i,j} = \frac{-u_{i+2,j} + 16u_{i+1,j} - 30u_{i,j} + 16u_{i-1,j} - -u_{i-2,j}}{12(\Delta x)^2} + O(\Delta x)^4 \qquad \textit{Eq. 78}$$

Higher-order schemes have a smaller truncation error, but the cost of their implementation is high. Choosing the right numerical scheme for the Navier-Stokes equations depends on: (1) the physics involved, (2) the geometry of the problem, (3) the

minimum level of accuracy required, and (4) the computational power available. The numerical scheme also determines the stability and rate of the computation's convergence.

Discretization has several disadvantages:

1. Some information about the state of a fluid, as the Navier-Stokes Equations describe it, is lost in the discretized version.
2. Numerical errors are thus introduced, since a discretized equation does not exactly represent the original continuous differential equations.
3. Consequently, the numerical error is manifested in forms of additional diffusion, insufficient diffusion, and faster-than-actual or slower-than-actual wave velocities.

These errors, however, can be managed. They can be prevented from influencing the accuracy of the calculated solution by carefully choosing the type numerical scheme best suited for the problem and maximizing the use of available computational resources.

Pressure Drag Calculation

Chapter 2 contained a detailed discussion of the sources and different types of aerodynamic drag. This section shows how the calculation of profile drag from pressure and shear forces is performed. The calculation starts by decomposing the aerodynamic force (a combination of lift and drag) on an object, denoted by the vector R in Figure 18.

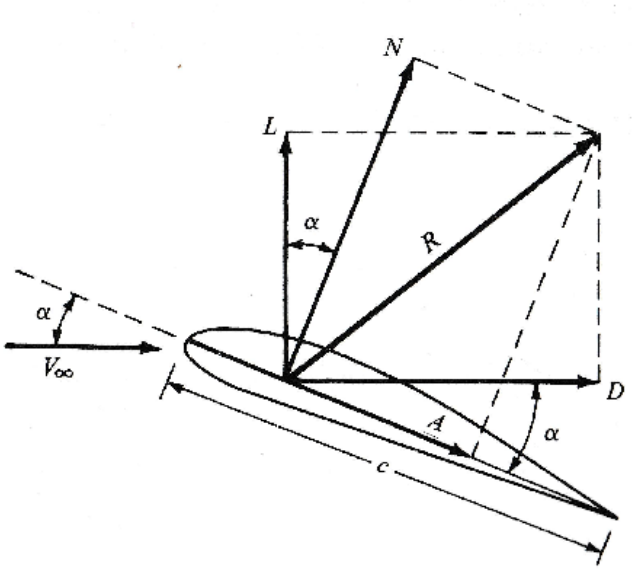

Figure 18. Resultant aerodynamic force and the components into which it splits.

The vector R can be decomposed into the force vectors *N* and *A*, called the normal and axial forces, and they run perpendicular and parallel to the object's chord (*c*), an imaginary line that connects the leading edge (LE) of an object to its trailing edge (TE). The vector R can also be decomposed into force vectors *L* and *D*, called the lift and drag forces and they run perpendicular and parallel to the incoming velocity. The two sets of forces are related to each other using the angle of attack, α (Eq. 79 and Eq. 80)[9]:

$$L \equiv -A \sin\alpha + N\cos\alpha \qquad \textit{Eq. 79}$$

$$D \equiv N \sin\alpha + A\cos\alpha \qquad \textit{Eq. 80}$$

For rotationally symmetric objects (e.g., a sphere) the normal and axial forces are always equal to the lift and drag forces, as the object's chord is always collinear with the freestream velocity.

Since the profile drag force is the sum of pressure and shear forces in the direction opposite the object's motion, the second decomposition of the vector R is used. The drag force varies for different geometries, and minimizing it is of particular interest to aircraft

designers and engineers. On aircraft, the drag force changes when the landing gear is retracted, speed brakes are deployed, or flaps and other control surfaces are lowered. When such complex shapes as external aerodynamic fairings on aircraft platforms are installed, the change in drag is difficult to calculate analytically. However, when complex shapes are approximated as a collection of smaller, simpler shapes, we can numerically calculate the value of drag as the sum of each of those individual components. Once the pressure and shear force around an object are known, through either experimental data or CFD results, the drag force can be calculated[9]:

$$D' = \int_{LE}^{TE} (-p_u \sin\theta + \tau_u \cos\theta) ds_u + \int_{LE}^{TE} (p_l \sin\theta + \tau_l \cos\theta) ds_l \qquad \textit{Eq. 81}$$

The subscript u indicates the quantity along the object's upper surface. The subscript l indicates the quantity along the object's lower surface. The chord line separates the upper and lower surfaces. The angle θ is the angle between the horizontal axis and the line tangent to the local surface.

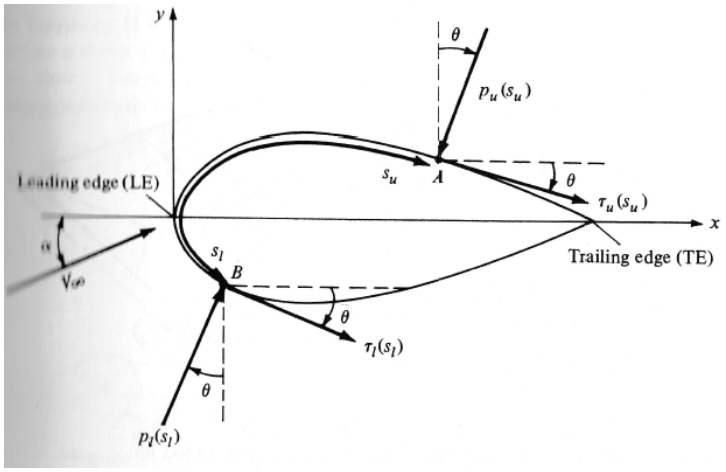

Figure 19. Nomenclature for the integration of pressure and shear forces.

Drag is also a function of the object's speed, surface area, and density. To compare the drag of an object traveling in different freestream conditions, it is helpful to normalize the drag force by a reference area, *A*, and the dynamic pressure of the fluid, q_∞[29]:

$$C_d = \frac{D}{q_\infty A} \qquad \textit{Eq. 82}$$

$$q_\infty = \frac{1}{2}\rho_\infty V^2 \qquad \textit{Eq. 83}$$

Similarly, a pressure coefficient can be defined to scale the pressure force felt along a point *'a'*:

$$C_{p,a} = \frac{p_a - p_\infty}{q_\infty} \qquad \textit{Eq. 84}$$

The pressure coefficient indicates whether flow has separated along an object's surface.

Now that the relevant equations are defined, this study now proceeds to examining how the drag coefficient changes with the various layouts and sizes of aerodynamic modifications.

Chapter 4: Modeling Approach: Geometry, Grids and Algorithm

Introduction

The objective of this study is to find relationships between design parameters available to engineers working on aircraft modifications and the drag coefficient. This chapter describes the scenarios studied using the software tool STAR-CCM+. There are two main categories of computational geometry considered, (1) two hemisphere obstacles, and (2) one hemisphere obstacle and one pod-shaped obstacle. Both sets of shapes are analyzed for a range of free-stream conditions, sizes, and distance between the obstacles. Each configuration tested will be referred to as a "case."

STAR-CCM+ Software Tool

The software suite STAR-CCM+, by CD-adapco, is a CFD tool used to perform calculations on a variety of flows by academia and industry. This software was chosen for this study because of its ability to automate changes in geometry and boundary conditions. The automation is possible because STAR-CCM+ internally links the computer aided design (CAD) geometry to the mesh. The mesh, the initial conditions, the boundary conditions, the physics models and the solver settings are all linked to the final output in single graphical user interface (GUI), shown in Figure 20. A general outline of the automated workflow is shown in Figure 21.

The first step to constructing a simulation in STARCCM+ is to divide the domain into "regions". A region is a distinct subdomain where a set of physics models are used. For subsonic flow around an airplane, for example, one region can encompass the airflow around the aircraft's outer mold line (OML), a second region can encompass the flow inside

an engine compressor, and a third region can encompass the engine combustor. All the cases studied in this paper utilize just one region encompassing the external fluid flow around the aircraft.

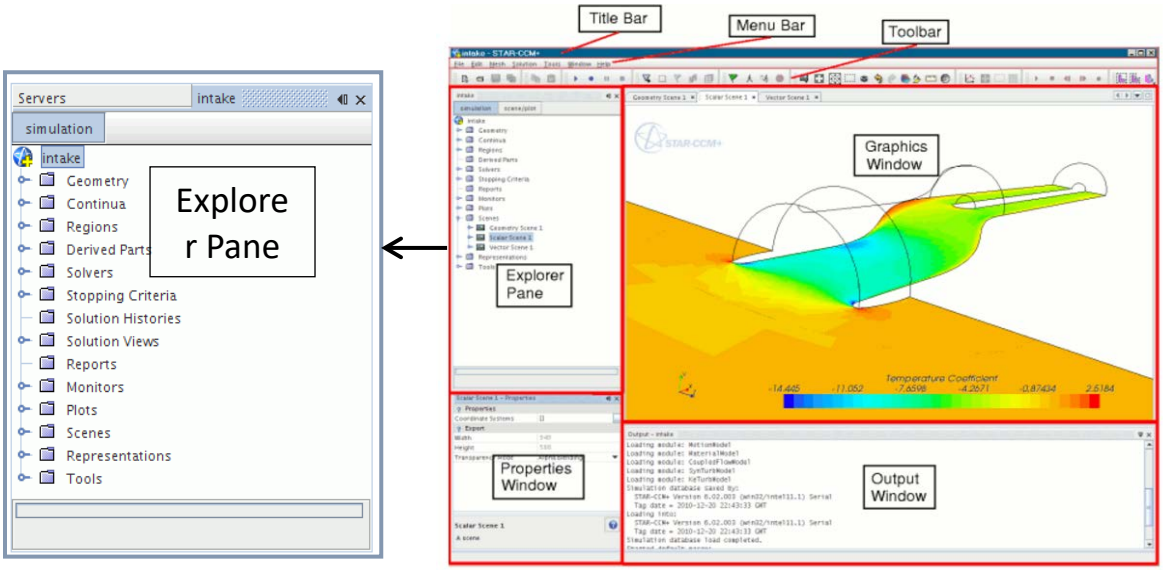

Figure 20. STAR-CCM+ GUI and a detailed view of explorer pane.

The second step in setting up a simulation is constructing the computer representation of the geometry. STAR-CCM+ has a built-in parametric-solid modeler that can be used to create geometry, such as aircraft surfaces and obstacle walls.

The third step in setting up a simulation is assigning boundary conditions at the edges of the regions identified in the first step. The boundary conditions for this study are the inlet conditions, outlet conditions, wall conditions and symmetric boundary conditions.

The fourth step is generating a “volume mesh” to represent the 3D model surfaces. A volume mesh is a mathematical representation of the region over which the Navier-Stokes equations are calculated. The representation of the physical boundaries of the

problem are defined in a volume mesh. Details about mesh quality is provided in a later section of this chapter.

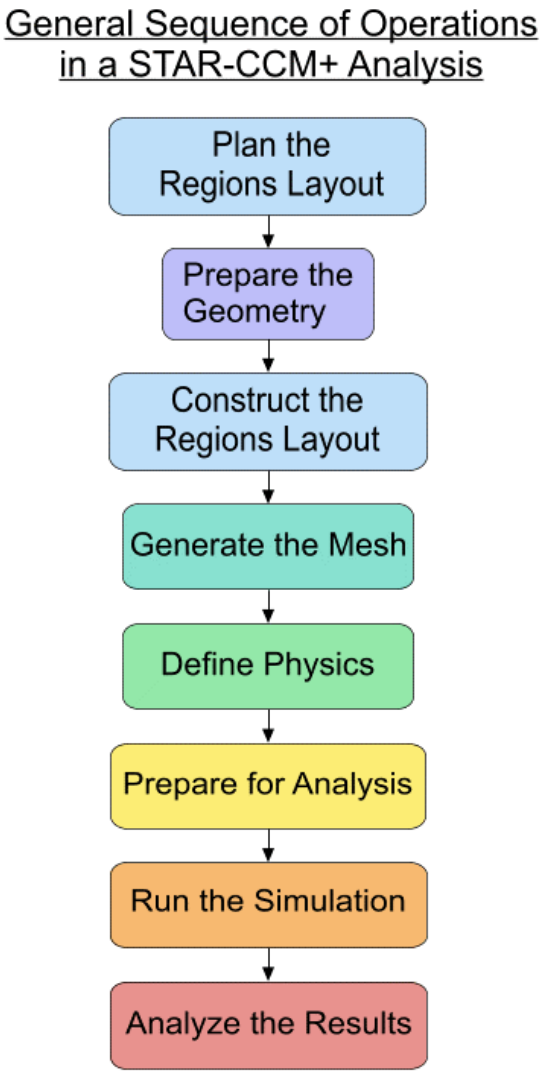

Figure 21. General steps for setting up a simulation in STAR-CCM+.

After creating a mesh, the next step is choosing physical models to represent the phenomena of interest. The user selects the models from a variety of physics models preloaded into STAR CCM+ software, shown in Figure 22. The physical models chosen for this study are described in a later section of this chapter.

The next step is preparing the workspace within STAR-CCM+ for analysis. This includes defining force coefficients, residual errors, maximum and minimum velocities, maximum and minimum temperature in areas of interest. This step also includes setting up figures and graphics.

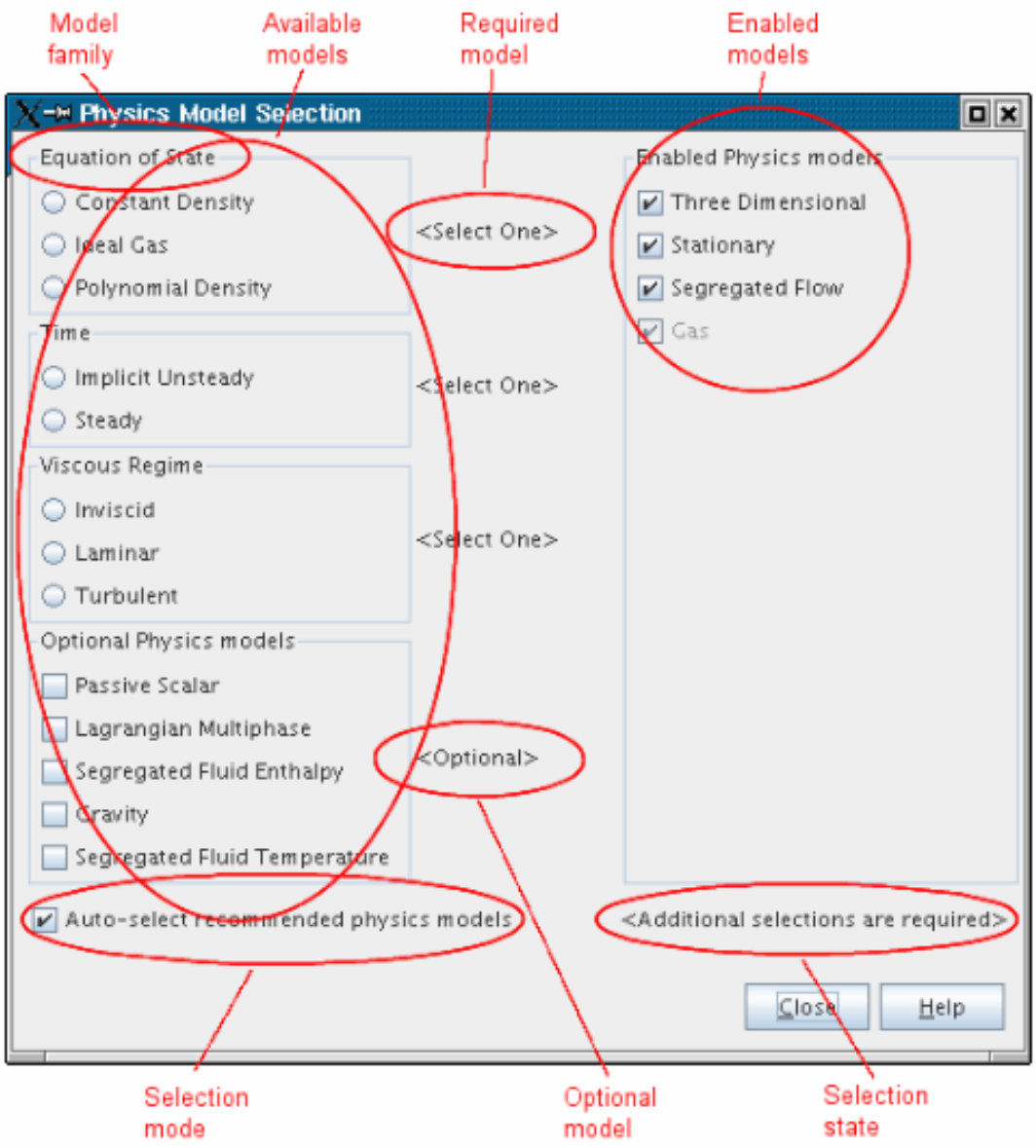

Figure 22. Physics Model selection dialogue within STAR-CCM+.

Obstacle Geometry

Antennae, cameras, and pod fairings attached to an aircraft surface can be approximated as simple shapes placed flush against a flat wall, as shown in Figure 23.

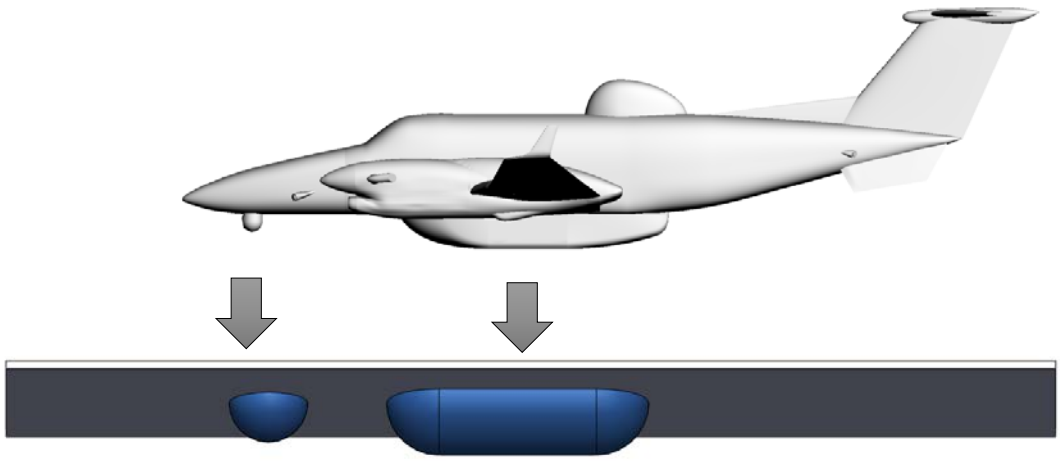

Figure 23. Simplified model of aircraft components.

The belly of the aircraft is modeled as a 2D flat surface instead of a 3D curved surface. This simplification is valid since the fuselage of a KA300 has a large diameter with respect to the obstacles mounted onto it and when the radius of curvature of a surface is significantly larger than the obstacles mounted on that surface, the curved surface can be locally approximated as a flat plane.

Two kinds of protrusions are studied, a hemisphere and a pod-like shape. The first protrusion is a hemisphere which approximates the shape of a camera modification shown in Figure 13. The hemisphere has a diameter of 1.5 ft in most cases. The second protrusion approximates the geometry of a pod fairing, shown in Figure 14, and consists of a half-cylinder shape capped on both ends with a quarter-spherical shape.

The flat fuselage section of a KA300 aircraft is approximately 40 feet long. The initial length of the domain should, therefore, be at least 40 feet. The center of the first obstacle is positioned 10ft behind the inflow plane for all cases studied. This distance ensures that the pressure disturbances due to the first obstacles does not propagate upstream and interfere with the user-specified inflow boundary condition.

Figure 24 shows that the dimensions of the domain, obtained after preliminary tests, is 40 ft x 10 ft x 10 ft. This choice of domain size minimizes interference with the inflow boundary conditions, the symmetry boundary conditions on the side and the outlet boundary conditions.

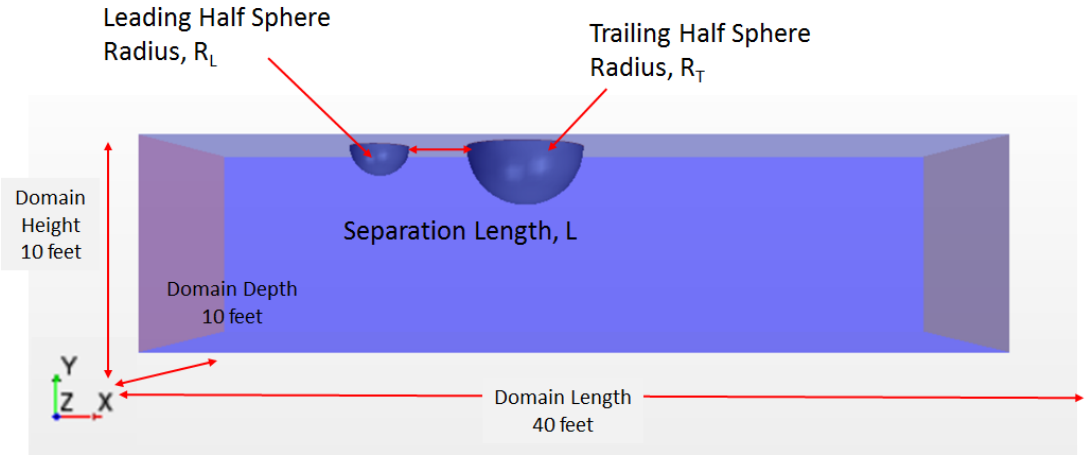

Figure 24. Computational domain description with design parameters.

The following calculation confirms that the effect on the drag on the obstacle due to the wall boundary-layer development at a point 10 ft downstream is small. The effective dynamic pressure[9] of a wall-mounted object due to presence of boundary-layer is given by,

$$q_{effective} = q\left(1 - 0.25\frac{\delta}{h}\right), \qquad \textit{Eq. 85}$$

where δ is the boundary-layer height and h is the height of the object, which in this case is the radius of the turret, or 0.75 ft. Thus, the approximate value of the boundary-layer height

on the aircraft is 2% of the distance from the origin of the aircraft. At 10 ft from the origin, the boundary-layer thickness is 0.2 ft. In the worst case, the smallest object analyzed effectively experiences a 6.25% change in dynamic pressure. For larger obstacles, the change in dynamic pressure is less.

Initial and Boundary Conditions

The operating conditions of the KA300 are used to define the initial and boundary conditions. The cruising altitude of the KA300 is 25,000 ft and the free-stream conditions can be calculated according to the ISA equations:

25,000 ft density: $\rho_\infty = 1.065\ slug/ft^3$

25,000 ft pressure: $p_\infty = 770.4\ lb/ft^2$

25,000 ft temperature: $T_\infty = -30.2\ °F$

Similar calculations were performed for the free-stream conditions at 5000 ft, 10,000 ft, 15,000 ft and 20,000 ft (Table 2).

Altitude	P	T	rho	mu
[ft]	[lb/ft^2]	[°F]	[slug/ft^3]	[lbf ·s/ft^2]
Sea Level	2116	59	2.378E-03	3.50E-07
5000	1755	41.1	2.049E-03	3.50E-07
10000	1445	23.3	1.756E-03	3.50E-07
15000	1181	5.4	1.496E-03	3.50E-07
20000	958	-12.4	1.267E-03	3.50E-07
25000	770	-30.2	1.065E-03	3.50E-07

Table 2. ISA conditions at altitude for KA300 aircraft.

The aircraft flight manual also recommends a cruising speed of 289 knots, which is equivalent to 487 ft/s. This is rounded down to 450 ft/s for convenience. At sea level, the cruise speed represents a Mach number of 0.40 and a Reynolds number of 1.64 x 10^7. At

25,000 ft, the cruise speed represents a Mach number of 0.44 and a Reynolds number of 7.34 x 10^6. The Mach and Reynolds numbers are tabulated in Table 3 for all the tested altitudes. The reference length for the Reynolds number calculation is 5.4 ft, which is the mean aerodynamic chord of the KA300 wing.

Altitude	Mach	Re
[ft]	[-]	[-]
Sea Level	0.40	1.64E+07
5000	0.41	1.41E+07
10000	0.42	1.21E+07
15000	0.43	1.03E+07
20000	0.43	8.73E+06
25000	0.44	7.34E+06

Table 3. Mach and Reynolds numbers at altitude for KA300 aircraft.

Since the Mach number is greater than the 0.3, the compressibility effects of air cannot be ignored for calculating accurate lift and drag forces around the obstacles. Although there is no sharp cutoff on the Reynolds number that indicates whether a fluid flow is turbulent or laminar, at approximately Re = 4000, there is a transition between turbulent and laminar flow. The flow is therefore turbulent for all the cases presented in this paper.

The conditions along the boundaries of the domain must be specified in order to calculate the flow properties and are shown in Figure 25. Some boundaries, such as the top wall, correspond to actual physical boundaries, like the skin of the aircraft. Other boundaries, such as the inflow and outflow, correspond to an imaginary boundary where uniform-velocity air enters the domain and air with uniform pressure exits the domain.

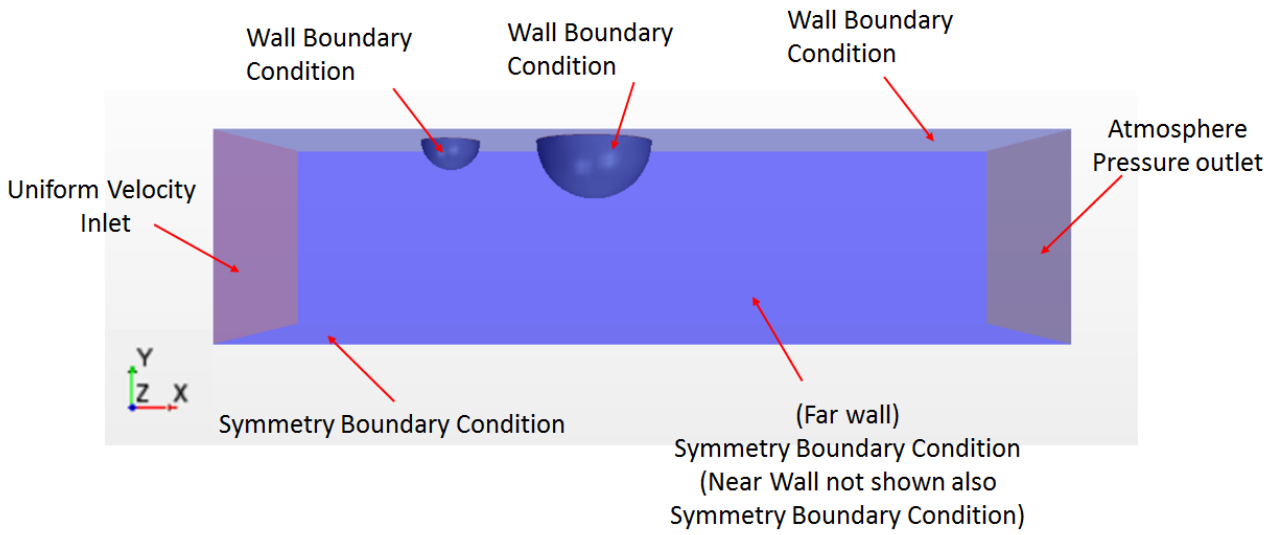

Figure 25. Boundaries include walls, velocity inflow, pressure outflow, and symmetry planes.

Wall Boundary

The top wall and the surfaces of the obstacles are assigned a no-slip, wall condition. No fluid penetrates the boundary and tangential velocity at the wall is zero due to viscous forces.

Inflow Boundary

The velocity specified at the inflow boundary is 450 ft/s, which is the approximate magnitude of air velocity experienced by a KA300 aircraft during cruise conditions.

Outflow Boundary

For most cases, the outflow boundary is assigned the ISA pressure and temperature at sea-level altitude. In other cases, the outflow boundary is assigned the ISA pressure and temperature at the various altitudes, as shown in Table 2.

Symmetry Boundary

The remaining three boundary conditions are assumed to be symmetry boundaries in order to model zero-shear, slip condition. This assumption simulates a free-stream

boundary condition since there is insignificant shear stress in the normal direction. This assumption, however, is only valid if the symmetry boundaries are placed far enough away from the wall-mounted objects. To verify that the symmetry planes do not interference with the flow around the wall-mounted objects, the blockage value of the obstacles is calculated and compared to an acceptable value found through prior experimentations.

According to Low Speed Wind Tunnel Testing[30], a blockage value of 5% will produce a velocity error of 1.3% and a dynamic pressure error of 2.6%. A single hemisphere, with 1.5 ft diameter, has a frontal area of 1.76 ft^2. This means the blockage value of this particular obstacle in a flow of cross section 100 ft^2 (10 ft x 10ft) is 1.76%. One can assume, therefore, the symmetry boundaries will have a negligible effect since the blockage value of 1.76% is less than the 5% threshold.

Three-dimensional Model

Calculating the drag coefficient using a 2D simulation would be faster and less computationally expensive than running 3D simulations. However, three dimensionality is an important feature of this problem. Many radomes, fairings and other aircraft protrusions are three dimensional rather than 2D and axis-symmetric like cylinders. A sphere and a finite length cylinder of equivalent size produce different drag forces because the third spatial dimension allows for pressure relief between areas of high and low pressure. In order to accurately calculate the drag of aircraft protrusions, a 3D model is implemented.

Steady-state

The presence of turbulence around aircraft means there are time-varying fluctuations in the flow. Since the desired output of this CFD calculation is the average drag force, time variations are not important. A steady-state calculation of the Navier-

Stokes equations averages the fluctuations and so that the resulting drag calculation is time-independent. Additionally, a steady calculation is less expensive and converges faster than an unsteady calculation because the time-derivative terms in the Navier-Stokes equations can be ignored.

Reynolds-Averaged Navier-Stokes

The flow being studied is turbulent and the Reynolds number is on the order of 10^6. Resolving the turbulent motion around the obstacles is computationally expensive, and a direct numerical solution of such high Reynolds number flow is beyond the computational resources available. Since an averaged solution is sufficient for a drag calculation, a RANS model is used.

Ideal Gas Assumption

The air in the earth's atmosphere, at the altitude ranges from sea level to 25,000ft, can be approximated as an ideal gas, which simplifies the equation of state. The assumption provides a relationship between independent variables in the Navier-Stokes equations, such as pressure, density and temperature. The ideal gas assumption is also traditionally applied to flow fields around subsonic aircraft and it is used in this CFD calculation as well.

Realizable 2 Layer k-ε Turbulence

The k-ε turbulence model, explained in Chapter 3 is used in all the calculations. Table 4 summarizes the constants used within the model.

Parameter	Value	Units
Turbulence Intensity	0.01	-
Turbulence Velocity Scale	3.28	ft/s
Turbulent Viscosity Ratio	10.00	-
C_μ	0.09	-
C_{1e}	1.44	-
C_{2e}	1.9	-
C_t	1.0	-
σ_k	1.0	-
σ_e	1.2	-

Table 4. Values of constants in the k-ε turbulence model.

Two Layer All Y+ Wall Treatment

A STAR-CCM+ model called 'two layer all Y+ wall treatment' provides the greatest flexibility for resolving the boundary-layer in the domain. It is a combination of the low and high y+ wall treatment equations. This model gives similar results to those obtained from both fine meshes that resolve the viscous sub layer and coarse meshes that fall in the turbulent portion of the boundary-layer. The STAR-CCM+ user guide recommends this model since it is the most encompassing wall treatment model available for external aerodynamic flows.

Convergence Criteria

The solution is converged when the computed drag coefficient from subsequent iterations varies by less than 1%. An example of a converged solution is shown in Figure 26. This pattern of convergence is typical for all the cases studied.

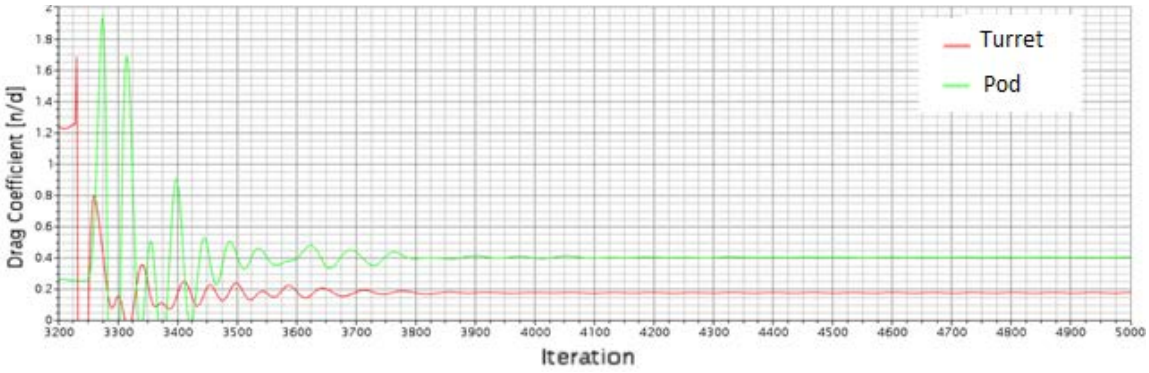

Figure 26. Drag vs iteration number of two hemispheres 6.57 ft apart.

Residuals are errors in mass, momentum and energy flux. When the residuals stabilize, the solution is converged, as shown in Figure 27. Generally, the cases studied had residuals on the magnitude of 10^{-3} in less than 3000 iterations.

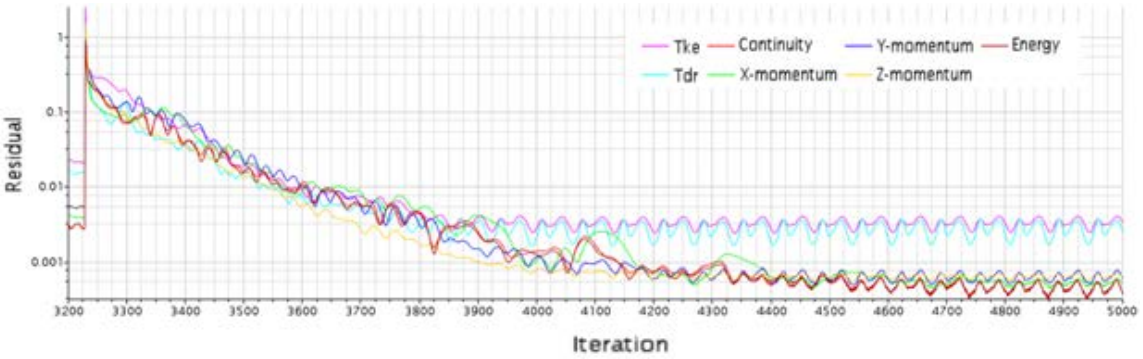

Figure 27. Residuals showing converged solution of two hemispheres 6.57 ft apart.

Mesh Generation

A mesh is a computational representation of the geometry of the physical domain on which the Navier-Stokes equations are solved. The mesh consists of cells of uniform or varying shape and size. The problem studied in this paper uses unstructured, or irregularly shaped cells. Most of the mesh is composed of tetrahedral cells shown in Figure 28(a). The target size of the tetrahedral cells was 0.5ft.

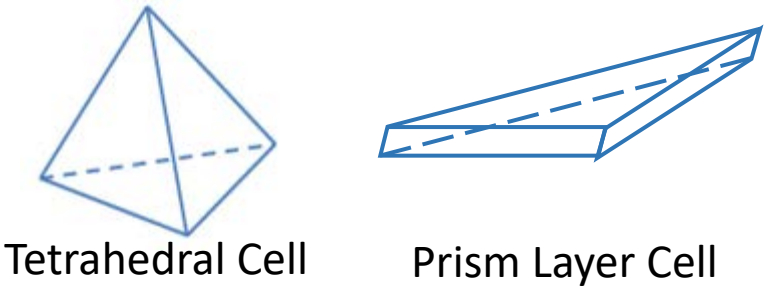

(a) (b)

Figure 28. Basic cell shapes used in the unstructured mesh for the study.

A “good” mesh allows for (1) solution accuracy, (2) greater range of convergence, and (3) faster computational time. A poorly defined mesh can create numerical errors. To ensure solution accuracy and convergence, a mesh is designed to resolve regions adequately where spatial gradients are high. Such regions occur where the mean flow changes rapidly, such as in areas of turbulence and areas where boundary-layers exist.

The size of the cells in the mesh should be as small as needed to reasonably resolve important features of the flow however too fine a mesh is computationally prohibitive. For this study, the mesh is coarse in the regions far away from the obstacles and becomes finer, with cells approximately three to four times smaller than the coarse regions, near the obstacles where turbulence is expected.

Fine resolution is also needed when there are boundary-layers. “Prism layer cells,” shown in Figure 28(b), are shaped so that their size in the wall-normal direction is much smaller than their size in the wall-parallel direction. The large size of the cell in the wall-parallel direction is allowable because the velocity gradient in that direction is much smaller than the velocity gradient in the wall-normal direction. In contrast, the size of this cell in the wall-normal direction is small, resulting in a flat shape. This shape satisfies both accuracy and cost constraints by reducing the number of cells required to resolve the

boundary-layer. The prism cell's thickness, 0.07ft, is determined by the wall functions, explained in Chapter 2. In the calculations presented here, five layers of prism cells are used in the mesh at all the wall boundaries.

Wall functions are used to obtain boundary conditions for the Navier-Stokes equations in the near-wall region. The advantage of using wall functions is the significant savings in terms of near-wall mesh resolution. In order for the wall equations to be accurate, however, the centroid of the first prism cell must lie within the log-law region of the boundary-layer.

Figure 29 shows y+ values along all the surfaces designated as a wall. Since majority of the y+ values are around 30-50, as recommended by the 'two layer all y+ treatment' model, the location of the centroid of the first prism layer is deemed acceptable.[18]

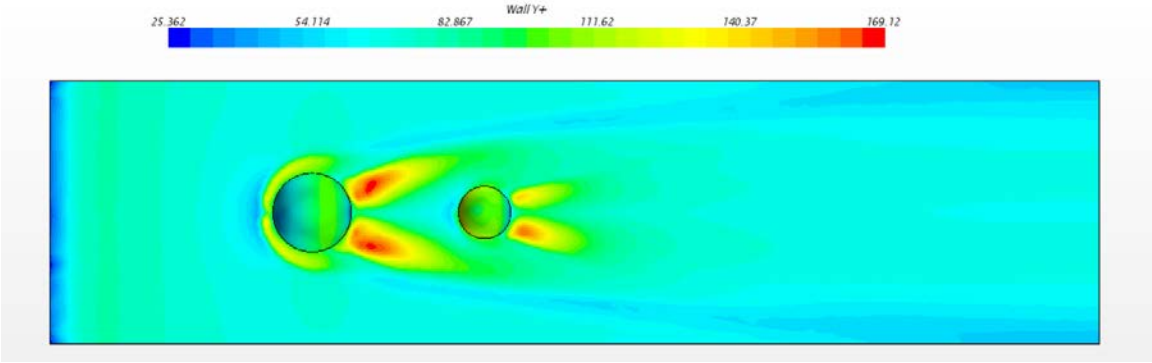

Figure 29. Wall Y+ values along wall surfaces within the domain.

STAR-CCM+'s mesh generation algorithm creates a mesh that satisfies the user-specified inputs, such as the size of the tetrahedral and prism layer cells. The mesh is also restricted by the size differences between adjacent cells. No two adjacent cell volumes are allowed to be more than 1.15 times larger or smaller than each other. This ratio is recommended to eliminate numerical errors when information is exchanged between two

cells.[31] The mesh shown in Figure 30 is typical of the meshes utilized in this study. The mesh consists of approximately 9.5 x 10^5 tetrahedral and prism layer cells.

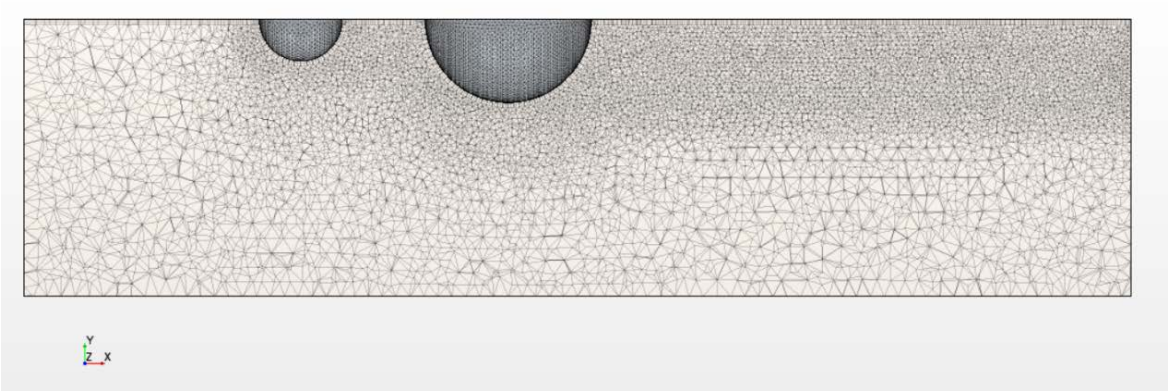

Figure 30. Overview of a typical mesh.

An inspection of

Figure 31 shows that the mesh might not be of good quality because of the significant differences in size and shape of adjacent cells. The view in

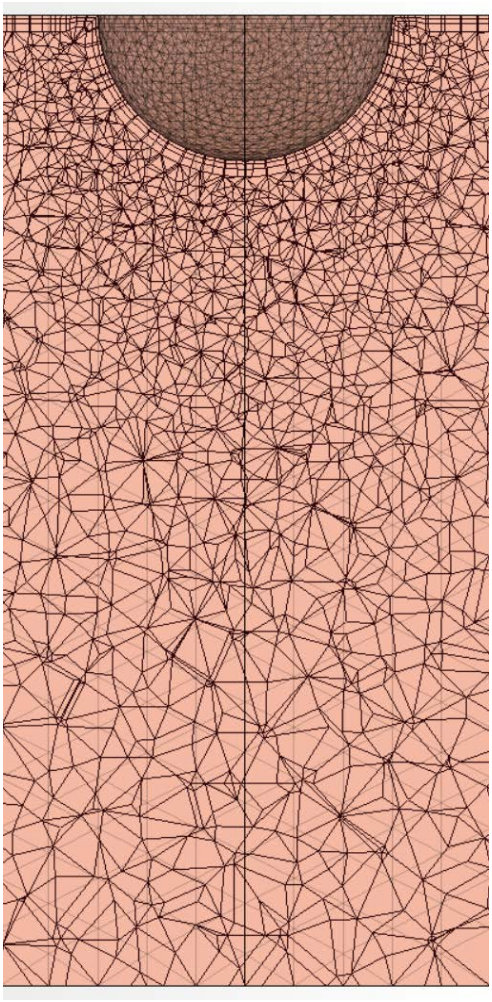

Figure 31, however, is a *planar* cut that bisects through 3D cells. To better visualize the cells within the mesh, an *isoplanar* cut, shown in Figure 32, is required which reveals the satisfactory quality of the cells.

These meshes are tested to ensure that they do not influence the CFD solution. The results of the validation tests are presented in the next section.

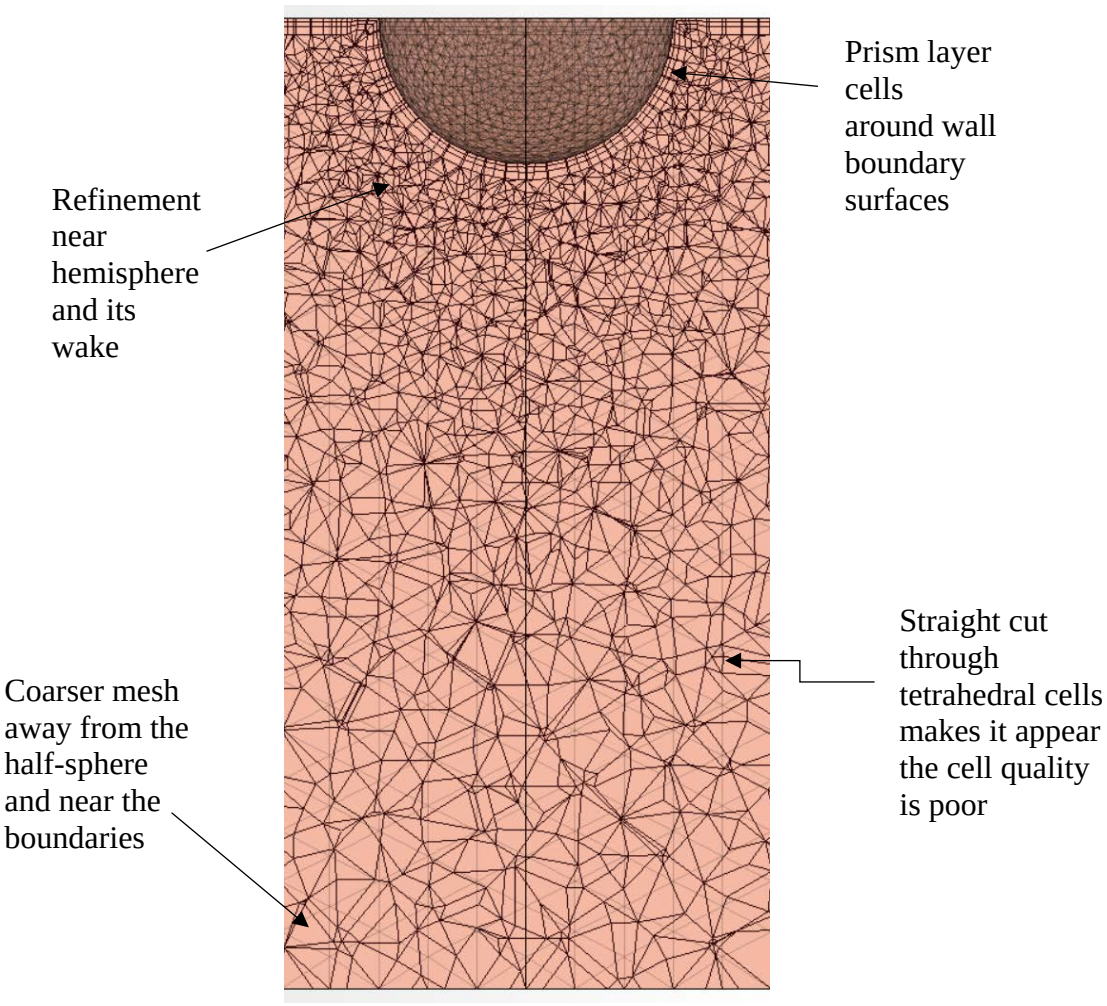

Figure 31. Near field and far field mesh in the vicinity of the obstacle.

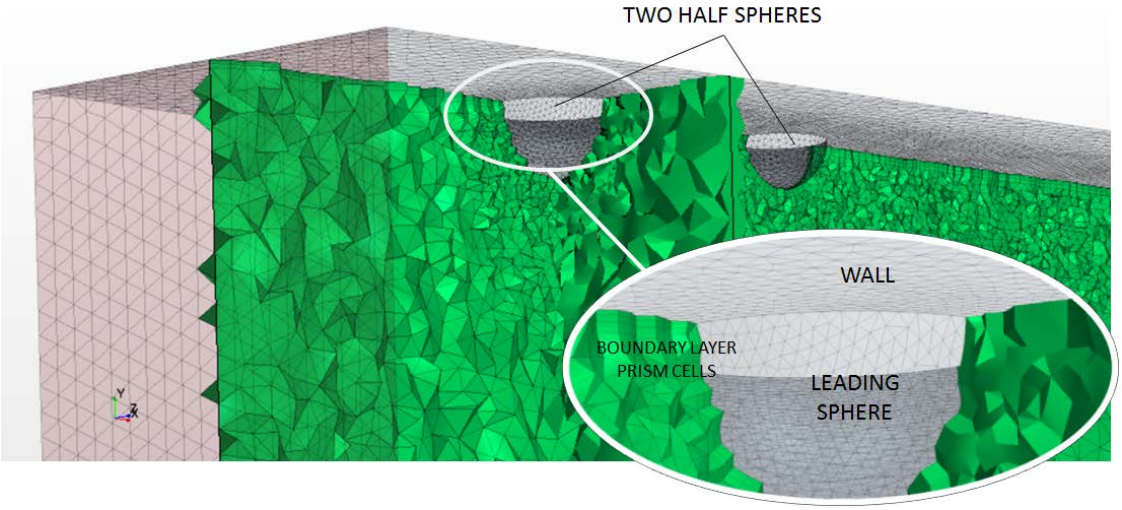

Figure 32. An isoplanar cut through mesh revealing 3D nature of tetrahedral cells.

Test Cases

Tests were performed to validate the STAR-CCM+ meshes and code. The tests include checking for (1) mesh independence and (2) accuracy of the coefficient of drag compared to wind tunnel data at low Reynolds numbers.

First the sensitivity of drag coefficient was investigated for meshes of varying cell densities, shown in the Figure 33. All the meshes represent a single hemisphere mounted on a wall and the drag coefficient was calculated for an inflow velocity of 450 ft/s at sea-level conditions. The results are presented in Table 5 and Figure 33.

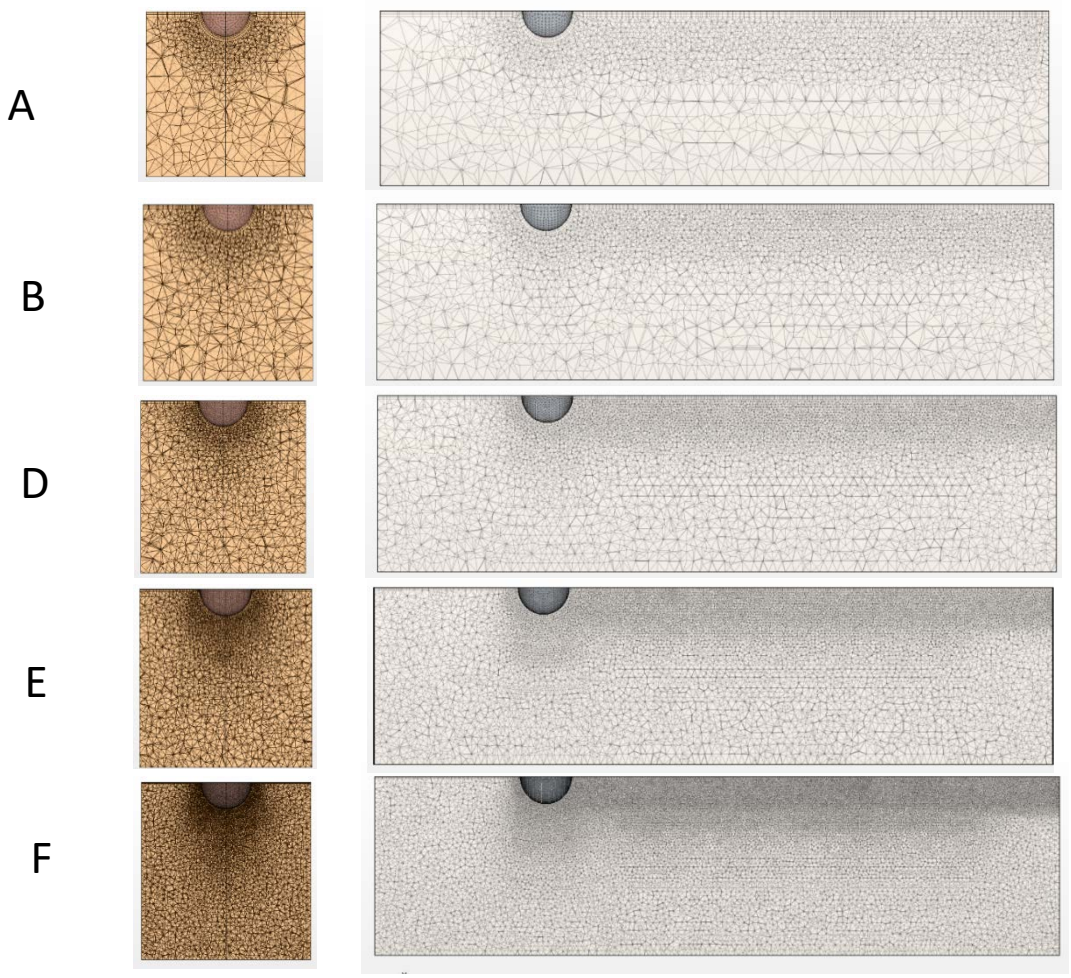

Figure 33. Various meshes of same geometric domain but different cell density.

Mesh ID	Total Cells	Base Size ft	Cd	Time to compute
[n/d]	*[n/d]*	*[ft]*	*[n/d]*	*[hrs]*
A	167816	1	0.232	0.3
B	315893	0.75	0.167	0.4
C	468295	0.625	0.234	1.5
D	~793000	0.5	0.436	3
E	~1,700,000	0.375	0.505	10
F	~5,000,000	0.25	0.480	120

Table 5. Mesh sensitivity analysis results.

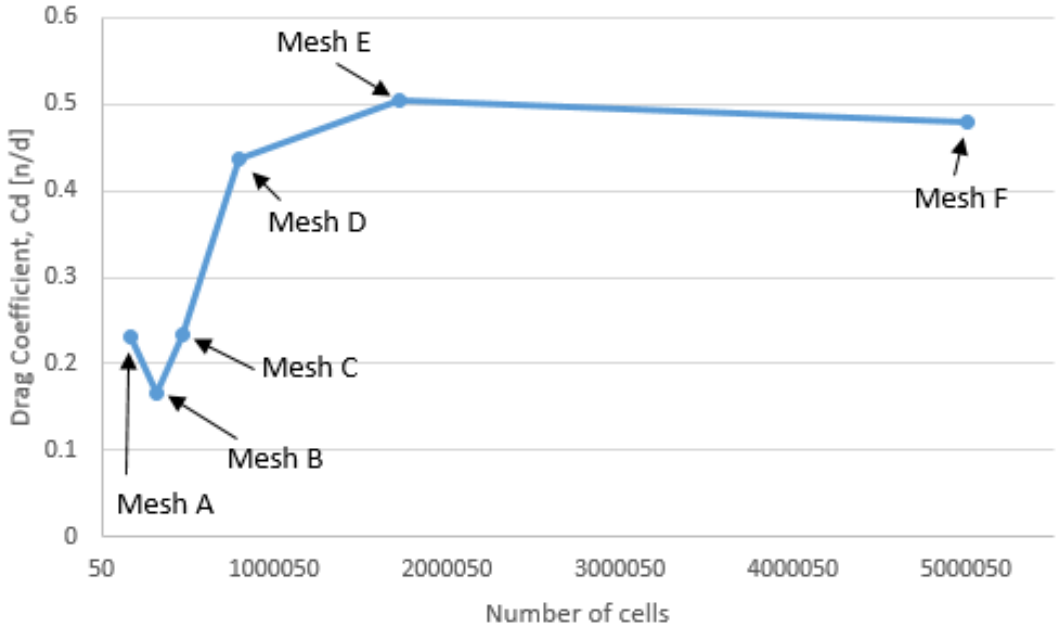

Figure 34. Calculated drag coefficient on various meshes.

The results show the calculated drag coefficient starts to plateau for meshes with densities greater than those of Mesh D. Solving the Navier-Stokes equations on finer meshes does not significantly alter of value of the drag coefficient suggesting the drag coefficient, and pressure field from which the drag coefficient is calculated, is independent of the mesh. No wind tunnel data is available to test the accuracy of the drag coefficient of a sphere mounted on a wall in such a configuration. If one assumes the calculation of the drag coefficient on Mesh F, the densest mesh, is the true drag coefficient, then the drag

coefficient calculated using Mesh D and Mesh E differ from the true drag coefficient by -10.0% and +5.2% respectively.

The drag coefficient calculated using Mesh E is more accurate than the one calculated on Mesh D but at a significant cost. Figure 35 presents the approximate time needed to calculate a converged solution on meshes of varying densities. Since over fifty cases are needed for this study, the shortest possible computational time is highly desired. Mesh D takes 3 hours to converge, and if -10% drag inaccuracy is acceptable, the calculations can be performed three times faster than on Mesh E and forty times faster than on Mesh F.

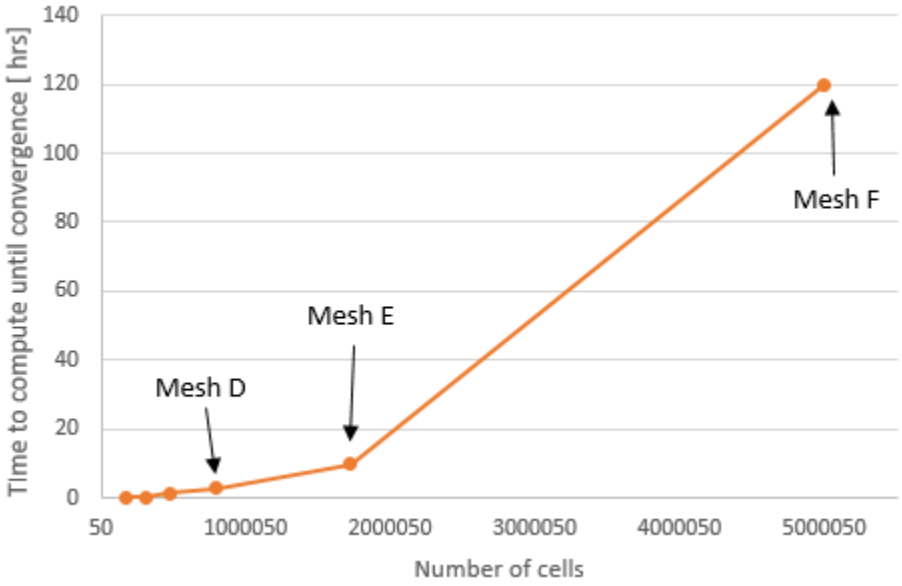

Figure 35. Time to calculate drag coefficient on various meshes.

No known experimental results have been published for the drag of a single hemisphere *mounted on a wall* for high Reynolds numbers. To calculate the accuracy of the drag coefficient on Mesh D, the calculated value is compared to half the value of the drag coefficient of a suspended sphere measured in experiments for various Reynolds

numbers. The reference length for the Reynolds number is a diameter of the hemisphere, 1.5 ft. The results are presented in Figure 36.

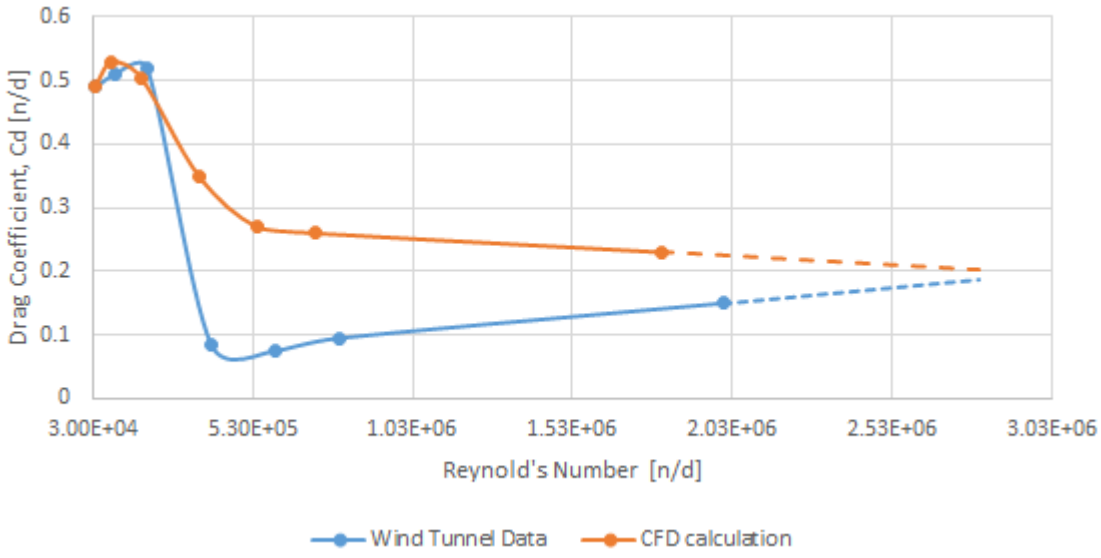

Figure 36. Drag coefficient of a single sphere for various Reynolds numbers,

The results show good agreement for the lower Reynolds numbers around 3 x 10^4. The agreement in drag coefficient exists despite the clear differences in the flow around a free floating sphere and a hemisphere mounted to a wall.

The results show the worst agreement for Reynolds numbers in the drag crisis range. Drag crisis is when the laminar boundary-layer transitions to a turbulent boundary-layer and the size of the turbulent wake behind the obstacle lessens. As a result, there is a notable drop in the drag coefficient of the obstacle. The deviation of the calculated drag coefficient from the experimental drag coefficient shows that the turbulence model poorly captures the transition from a laminar to turbulent boundary-layer. It is also probable that the presence of the wall boundary in the CFD calculation increases the drag coefficient of the hemisphere as the Reynolds number is varied in the drag crisis range.

Attempts to calculate additional drag coefficients in the drag crisis range resulted in a failure to achieve convergence. This suggests the k-ε turbulence model has difficulty converging while trying to capture effects of the drag crisis. Since the cases of interest have a Reynolds number much higher than the Reynolds number of the drag crisis, the turbulence model selected should be adequate.

A linear extrapolation of the experimental and calculated drag coefficients shows that at higher Reynolds numbers the wind tunnel and CFD data should converge. There is no known experimental data for flow over a single sphere in Reynolds numbers higher than 2×10^6 to verify this extrapolation.

To further test for mesh independence, another sensitivity study was performed using meshes that represent the geometry of two hemispheres in a freestream flow of 0.40 Mach and 1.6 x 10^7 Reynolds number. The results are presented in Table 6 and Figure 37.

Mesh ID	Total Cells	Base Size	Cd Trailing	Cd Leading	Time to Compute
[n/d]	*[n/d]*	*[ft]*	*[n/d]*	*[n/d]*	*[hrs]*
G	~180000	1	0.280	0.281	0.5
H	~950000	0.5	0.436	0.416	3
J	~2,000,000	0.375	0.448	0.358	24

Table 6. Mesh sensitivity results for two hemisphere obstacles.

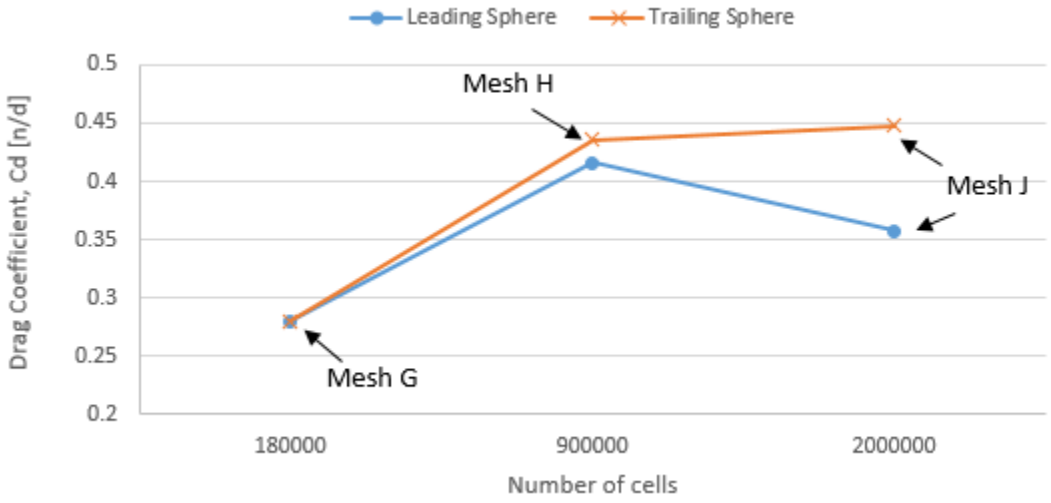

Figure 37. Mesh sensitivity study of two hemispheres mounted on a wall.

The data presented in shows that the drag coefficient of the trailing hemisphere plateaus starting at Mesh H, indicating the calculation is independent of the mesh. The drag coefficient of the leading hemisphere is reduced 14 % as the mesh is refined. The reason for this is unclear. The flow behind a sphere is unstable and the pressure fluctuations vary greatly. The steady calculation of an unsteady pressure field causes the unexpected decrease in drag coefficient. This problem is inherent to the study because a steady solution is being imposed on a phenomenon that is fundamentally unsteady in nature.

Chapter 5: Results

This chapter presents the numerically derived drag coefficients of two wall-mounted obstacles in various configurations. The first section presents data on two hemispheres on a wall, as shown in Figure 38. The second section presents data of one hemisphere and an oblong pod shape mounted on a wall, as shown in Figure 39.

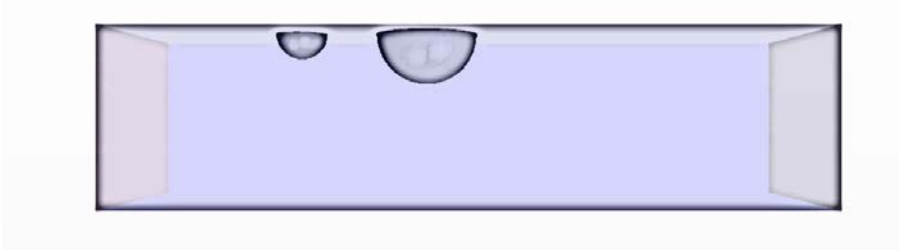

Figure 38. Two hemispheres geometry.

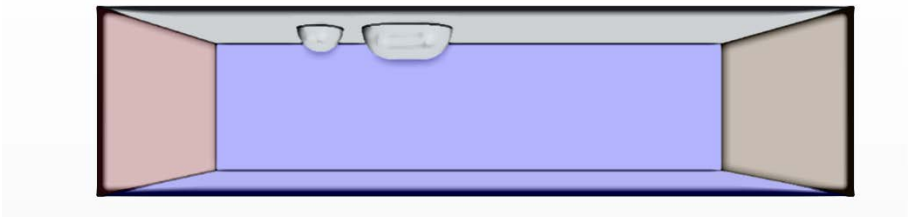

Figure 39. One hemisphere and oblong pod geometry.

Two Hemispheres

Data was collected to study the effects of Mach and Reynolds numbers on drag coefficient for the two hemispheres mounted on a wall, as shown in Figure 40. The range of Reynolds number and Mach number studied represent the range of flows encountered by a KA300 aircraft during cruise at various altitudes. The inflow velocity was held to a constant 450 ft/s to simulate the approximate cruising speed of a KA300. The reference length for the Reynolds number calculation was the diameter of the leading hemisphere.

Figure 41 and Figure 42 show the calculated drag coefficients of the leading and trailing hemispheres as a function of Mach number and Reynolds number.

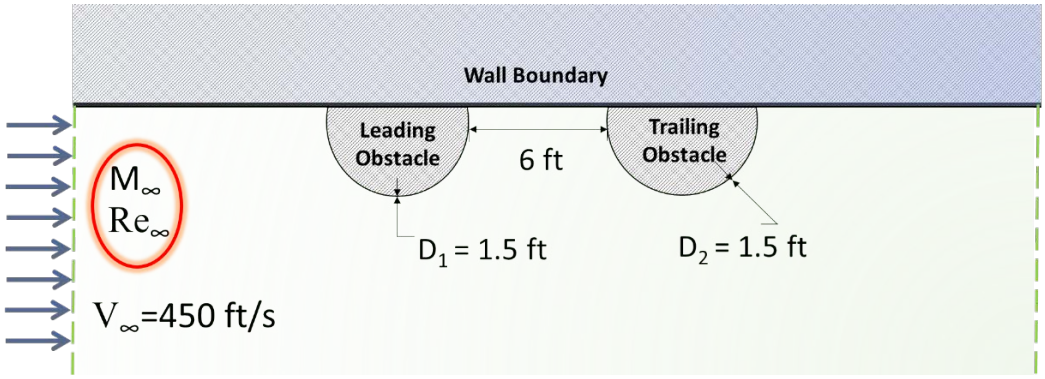

Figure 40. All parameters fixed except freestream Mach and Reynolds number.

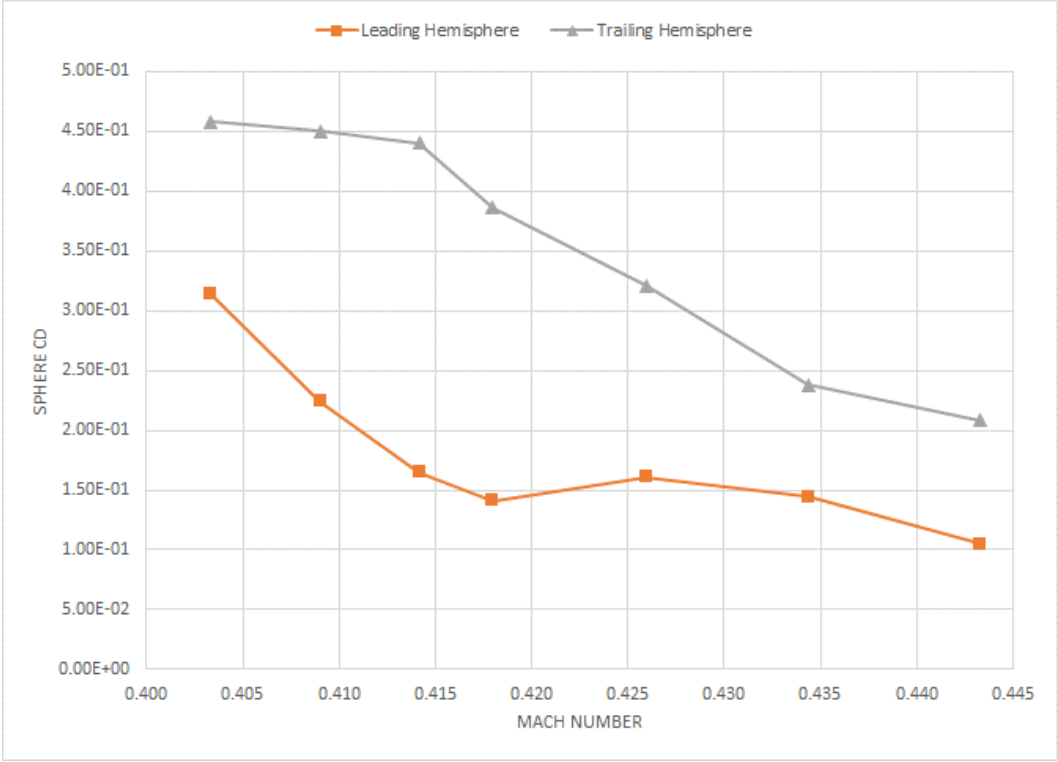

Figure 41. Drag coefficient of two hemispheres as a function of Mach number.

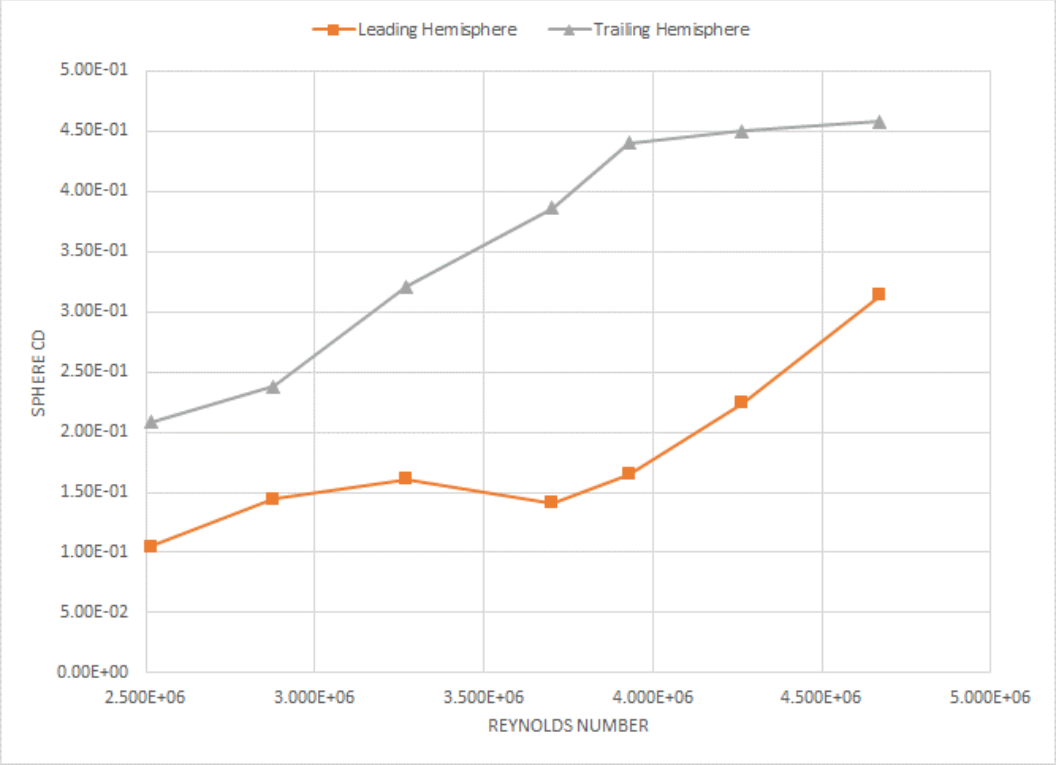

Figure 42. Drag coefficient of two hemispheres as a function of Reynolds number.

The drag coefficient of each hemisphere generally decreases with increasing Mach number and generally increases with increasing Reynolds number. At sea level, where the Mach number is the lowest and the Reynolds number is the highest, the computed drag coefficient of the leading hemisphere is 0.31 and the computed drag coefficient of the trailing hemisphere is 0.46.

Next, data was collected to study the effects of the size of the trailing obstacles on the drag coefficient of two hemispheres mounted on a wall as shown in Figure 43. The leading hemisphere diameter was held constant at 1.5 ft and the diameter of the trailing hemisphere varied from 1 ft to 3 ft. This range of diameter represents the possible diameter of obstacles that can fit underneath a KA300 without striking the ground during operations. In order to keep the separation distance between obstacles a constant as the size of trailing

obstacles increased, the centroid of the trailing obstacle was moved aft such that the shortest distance between the two hemispheres was constant at 5.25 ft.

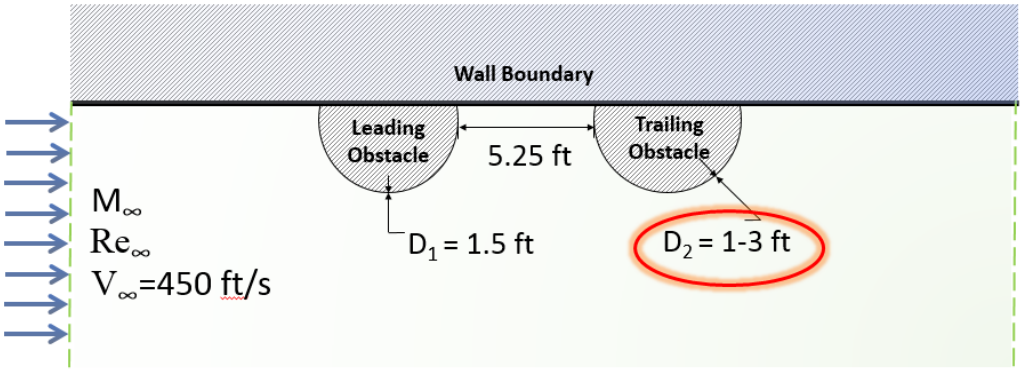

Figure 43. All parameters fixed except size of trailing sphere.

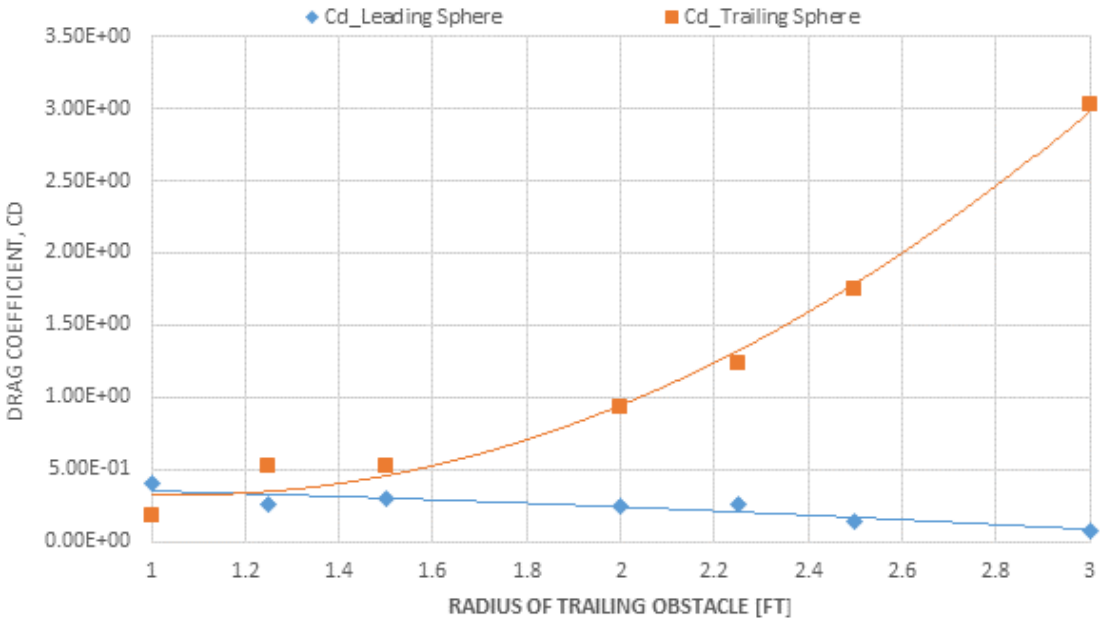

Figure 44. Drag coefficient vs. size of trailing hemisphere.

Figure 44 presents the calculated drag coefficients of the leading and trailing hemispheres as the size of the trailing hemisphere changes. The results show that the drag coefficient of the trailing hemisphere increases with increasing diameter. The drag

coefficient of the leading obstacle decreases by 80% from 0.40 to 0.079 as the trailing obstacle becomes larger.

Additional data was collected to study the effects of separation length on the drag coefficients of two hemispheres mounted on a wall as shown in Figure 45. For each test case, the diameter of the leading and trailing obstacles was 1.5 ft and the obstacles were subject to an inflow velocity of 450 ft/s flow at sea-level conditions.

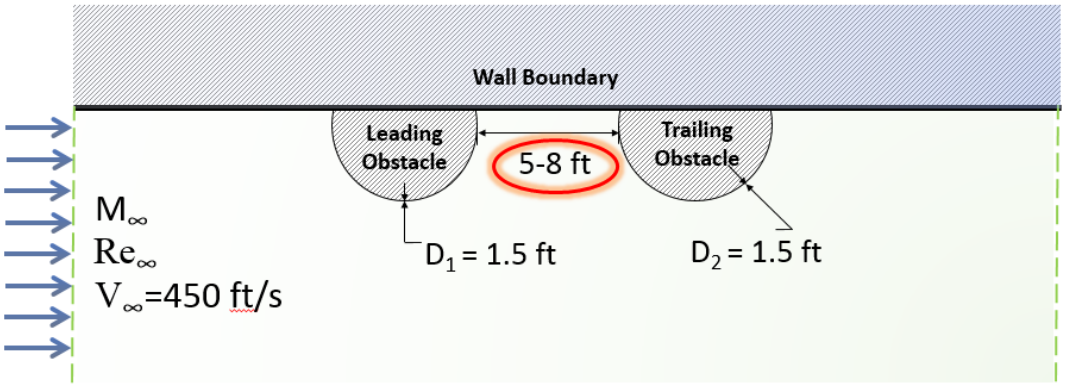

Figure 45. All parameters fixed except separation distance.

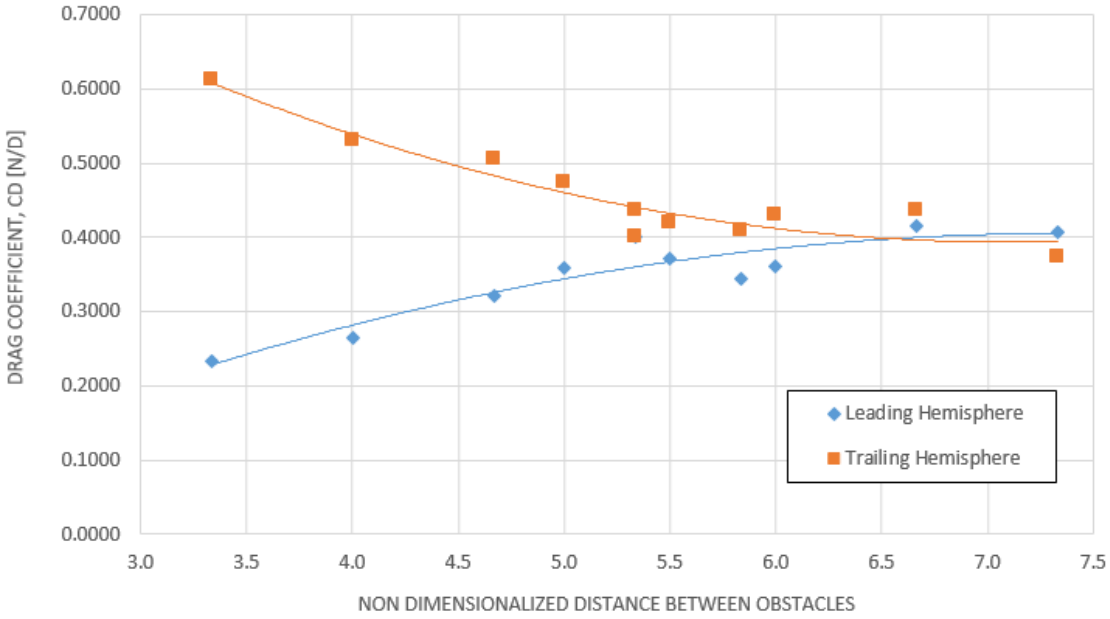

Figure 46. Drag of two hemispheres at different distances.

Figure 46 presents the drag coefficient for the leading and trailing hemispheres at different separation distances. The drag coefficient of the leading hemisphere generally increases as the separation length increases. The drag coefficient of the leading hemisphere is 0.23 when the two obstacles are closest and 0.40 when the obstacles are farthest apart. The change in the drag coefficient of the leading hemisphere corresponds to an 85% increase in drag. The drag coefficient of the trailing hemisphere decreases as the separation length increases. For both hemispheres, the drag coefficients remain unchanged around the non-dimensional separation distance of 6.0 and higher.

Next, data was collected to examine the effect of the size of the trailing obstacle and the separation distance between obstacles on the computed coefficient of drag on both obstacles, as shown in Figure 47. The cases studied include separation distances of 3.5 ft and 5.5 ft. The diameter of the trailing obstacle varied from 1 ft to 3 ft. When the obstacles were separated by 3.5 ft, computations for trailing hemisphere with diameters above 2 ft were attempted, but the calculations did not converge. For all cases, the inflow velocity was 450 ft/s and the leading hemisphere had a constant diameter of 1.5 ft.

The data in Figure 48 shows that the drag coefficient of the leading hemisphere decreases and the drag on the trailing hemisphere increases as the size of the trailing obstacle increases. This result is consistent with the results presented in Figure 44 where *only* the size of the trailing obstacle varied. When the obstacles are placed further apart, the interference effects seems less pronounced.

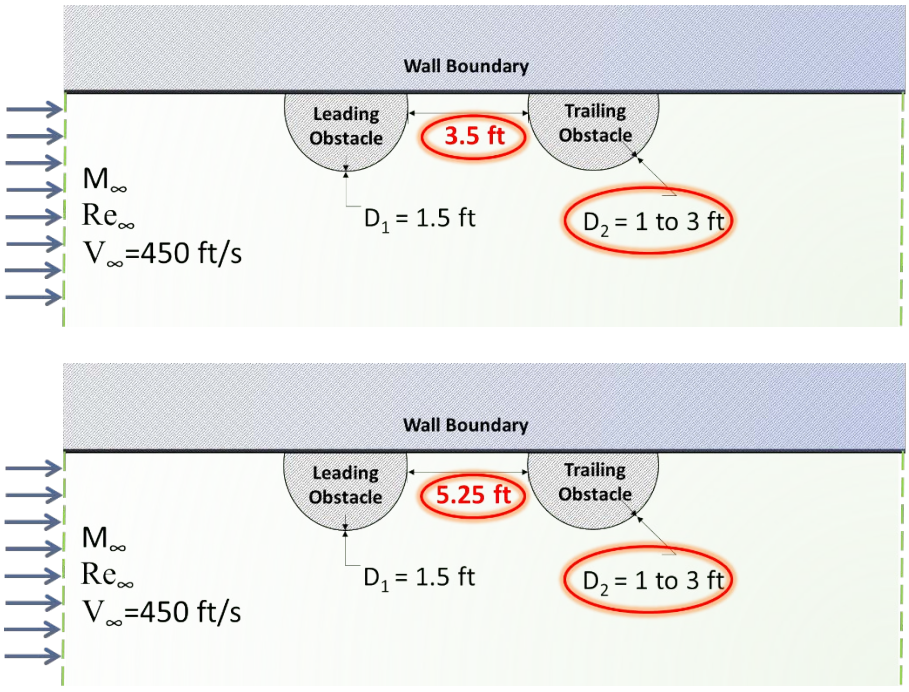

Figure 47. All parameters fixed except the size of the trailing obstacle and separation distance.

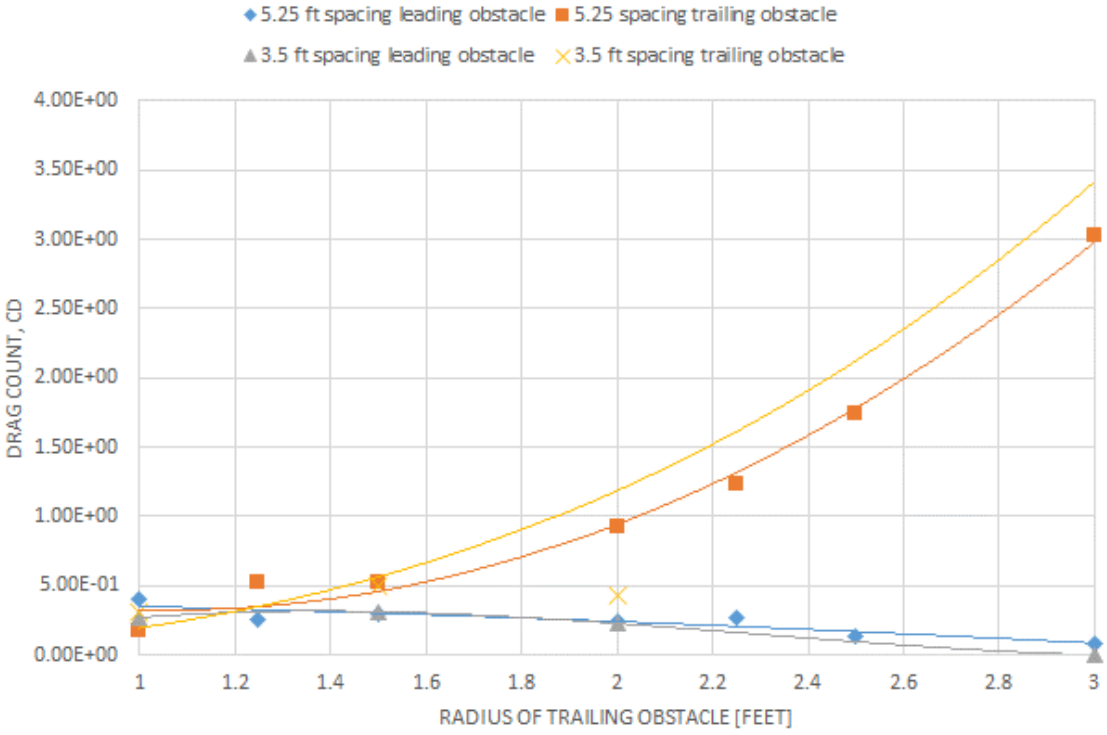

Figure 48. Drag of two hemispheres separated by different lengths.

One Hemisphere and Oblong Pod

Data was collected to study the effects of separation distance on the calculated coefficient of drag of a leading hemisphere and an oblong pod mounted on a wall in a tandem configuration, as shown in Figure 49. For all the cases, the diameter of the leading hemisphere was 1.5 ft and the fineness ratio for the trailing pod shape was 2.33. The pod had a 1.5-ft diameter and 2-ft-long straight section. The two obstacles were subject to inflow of 450 ft/s at sea-level conditions. For this study, the distance between the two obstacles was varied.

The leading hemisphere has the lowest drag coefficient when it is closest to the oblong pod. The drag coefficient of the leading hemisphere increases, however, as the distance from the pod increases. The drag coefficient of the leading hemisphere increases approximately 20% and then starts to plateau at a value of 0.46 when the separation length is 5.5D ft, or 5.5 times the length of the leading obstacle.

The oblong pod has the highest drag when it is closest to the leading hemisphere. The drag coefficient of the pod decreases, however, as the distance from the hemisphere increases. The drag coefficient of the pod decreases approximately 30% to 0.37 and remains at that value when the separation length is greater than 5.5D.

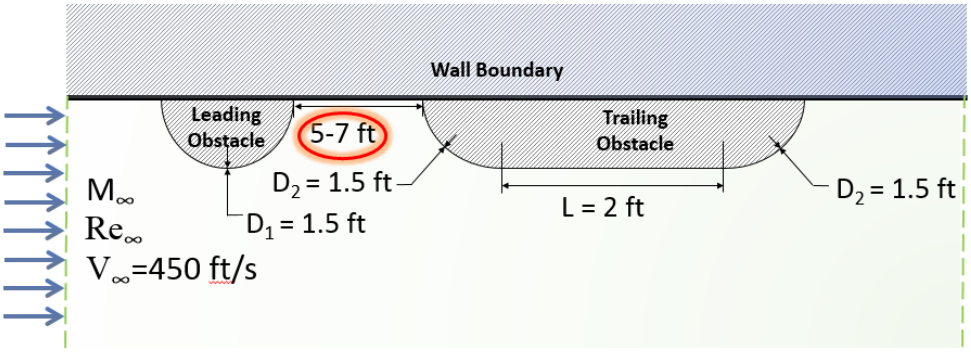

Figure 49. All parameters fixed except separation distance.

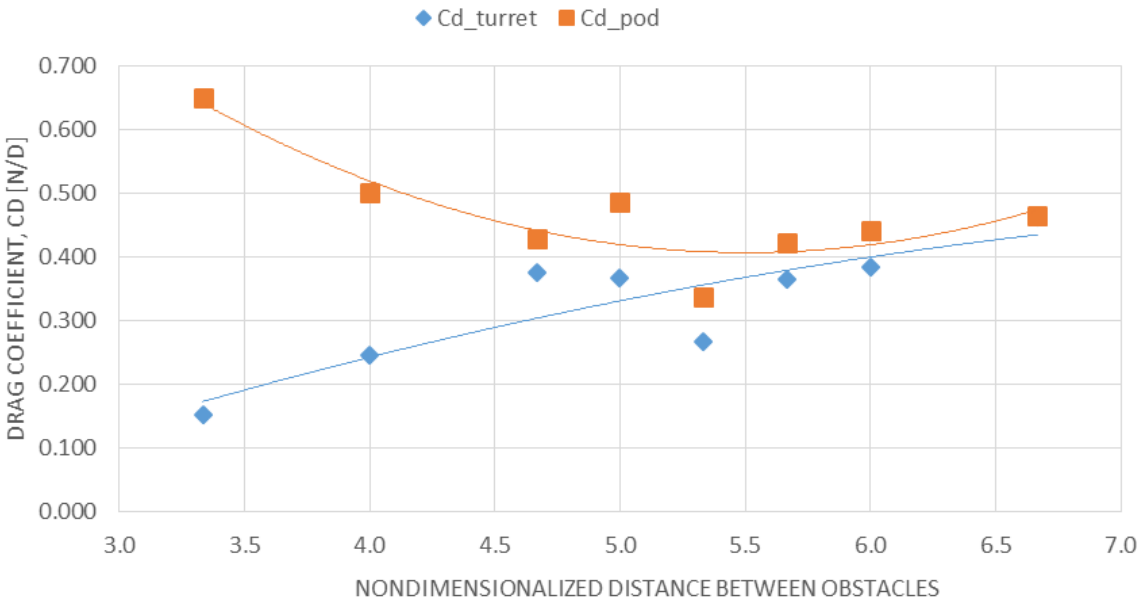

Figure 50. Drag of a hemisphere and pod at varying separation lengths.

Chapter 6: Analysis & Discussion

This chapter presents an analysis and discussion of the computational results shown in Chapter 5.

Effect of Mach and Reynolds Numbers

Figure 51 and Figure 52 present data on two hemispheres mounted on a wall as a function of Mach number and Reynolds number. The two hemispheres were separated by a distance of 4D, or four times the reference length of the leading obstacle. The results are presented in terms of sensitivity value, which is a measure of the aerodynamic-interference effect and is defined as the ratio of an object's drag coefficient in an isolated setting to its drag coefficient when subject to interference effects. The theoretical drag coefficient with no interference effects is represented by a sensitivity of 1.0 for all Mach and Reynolds numbers. The theoretical drag coefficient of a single wall-mounted hemisphere was calculated in CFD for sea-level atmospheric conditions and then adjusted for varying Reynolds and Mach numbers.

The results show the sensitivity of the leading obstacle is on average 0.73, meaning the interference effects cause the leading obstacle to experience a 27% lower drag than it would experience in an isolated setting. Since the value of sensitivity is less than unity, it indicates that the leading obstacle is located favorably. The greatest reduction in the drag coefficient occurs at the low Mach numbers and high Reynolds numbers.

The sensitivity value of the trailing obstacle is on average 1.45, indicating that the trailing obstacle experiences about 45% higher drag because of its placement with respect

to the leading obstacle. The increase in drag is not as pronounced at the higher Mach numbers and at the lower Reynolds numbers.

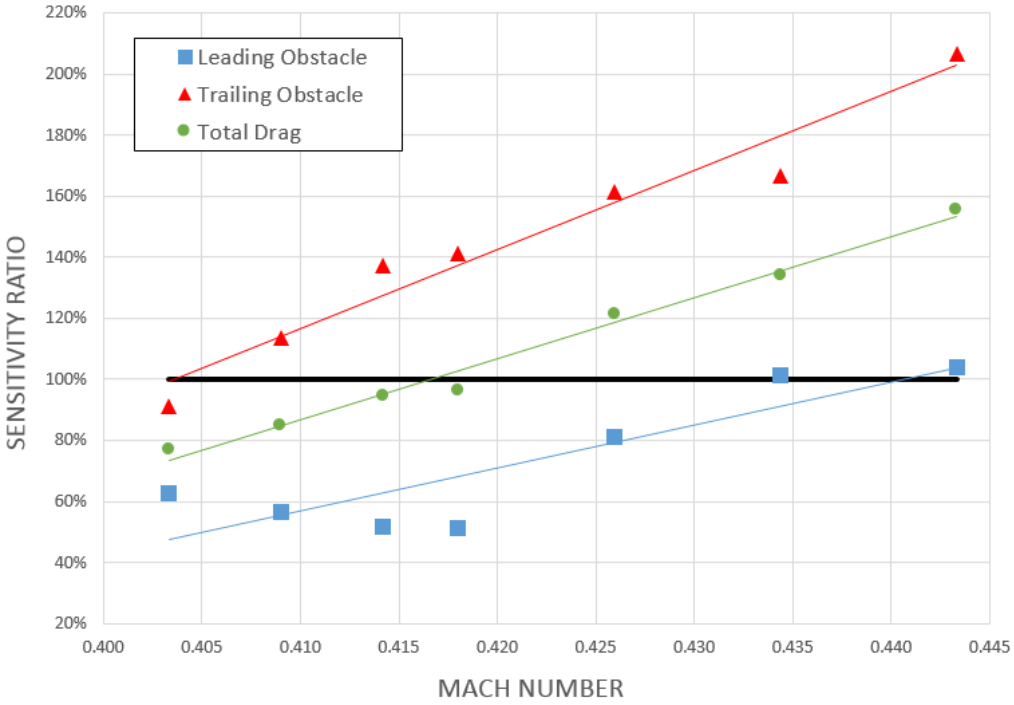

Figure 51. Mach effects on drag coefficient of two hemispheres separated by distance 4D.

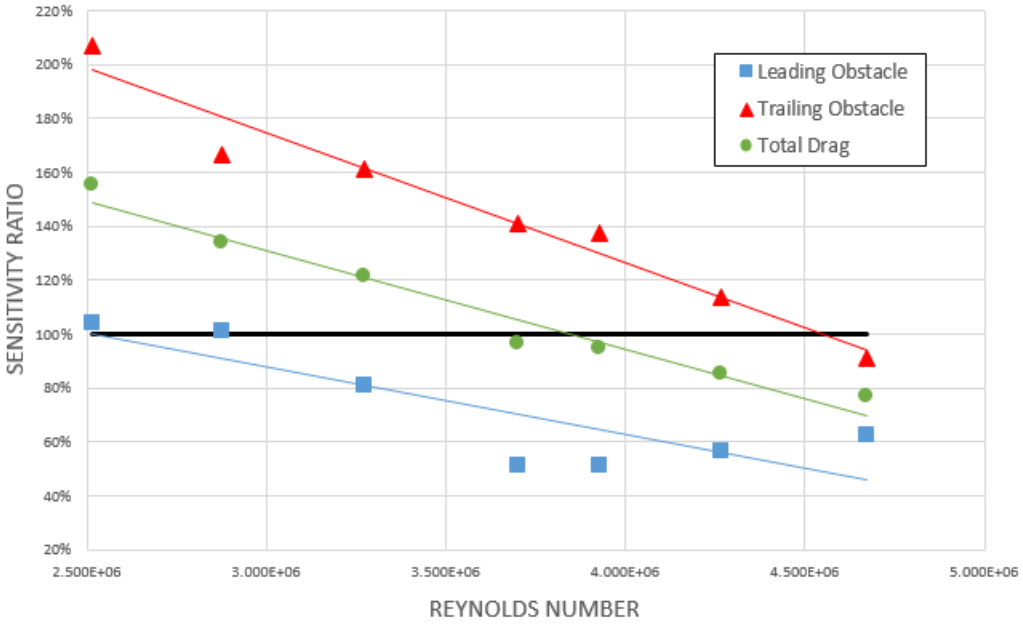

Figure 52. Reynolds effects on drag coefficient of two hemispheres separated by distance 4D.

For the lower Mach numbers (and higher Reynolds numbers), the interference effects reduce the total drag coefficient of both obstacles. At the lower Mach numbers, the unfavorable interference drag on the trailing obstacle is offset by the favorable interference effects on the leading obstacle. The average sensitivity is 0.88.

For the higher Mach numbers (and lower Reynolds numbers), the trends are reversed, and it is unfavorable to place two obstacles in tandem and 4D distance apart. Due to interference effects, the sum of the drag coefficients of both two obstacles is on average 37% greater than the sum of the drag coefficients when the obstacles are isolated. To investigate why the interference effects are dependent on Mach number, streamlines around the two hemispheres were calculated for low Mach number and high Mach number. The streamline calculations are presented in Figure 53 and Figure 54.

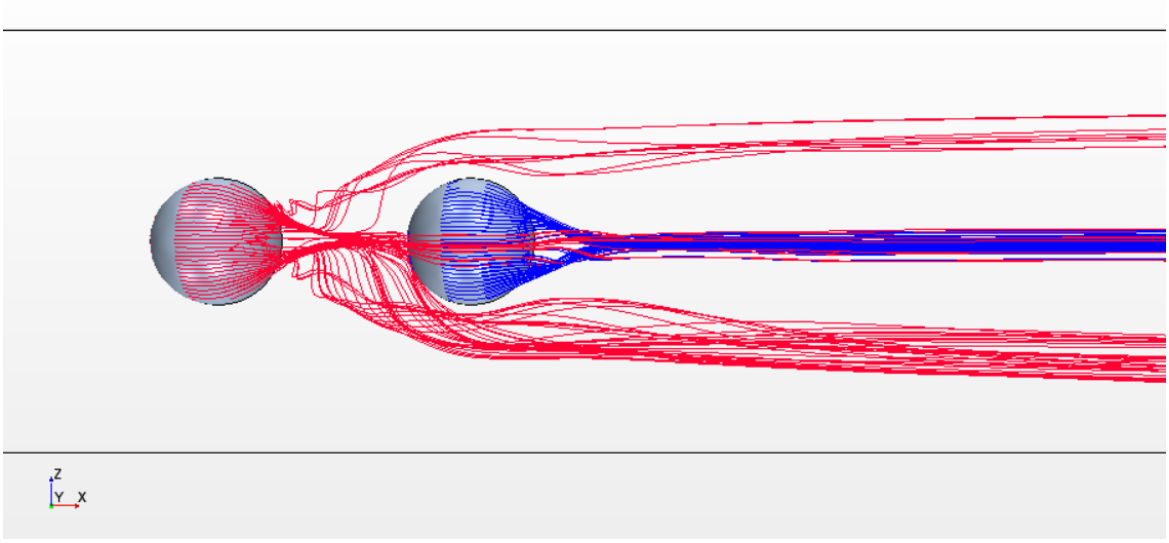

Figure 53. Streamlines of two wall-mounted hemispheres in tandem at lower Mach number.

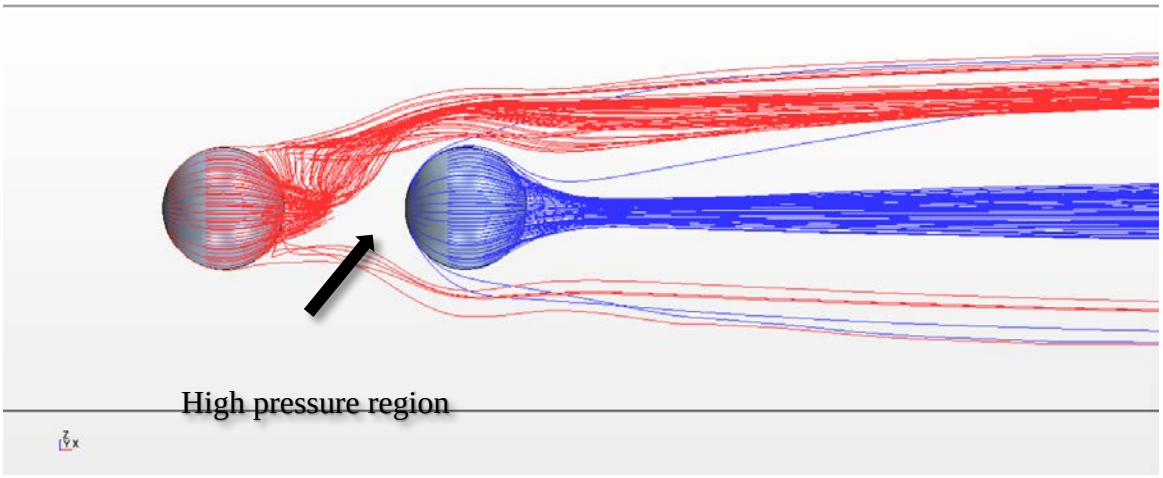

Figure 54. Streamlines of two wall-mounted hemispheres in tandem at higher Mach number.

For all the Mach numbers studied, the flow behind the trailing hemisphere remain largely unchanged since the streamlines appear in the same place. At the higher Mach number, streamlines from the leading hemisphere do not penetrate the region just ahead of the trailing obstacle, when compared to streamlines in the same region at lower Mach number. As the Mach number is increased, the leading obstacle creates a higher-pressure region in its wake. This creates a favorable pressure gradient for the leading obstacle which results in the lower drag coefficient. To confirm this, pressure coefficients were calculated along the centerline of the hemispheres and the results are presented in Figure 55.

The x-axis in Figure 55 is the distance along the hemisphere's circumference. The data show that both obstacles experience about the same pressure in the rear half of their regions. For positions less than 0.2ft, the pressure coefficient on the leading obstacle is higher than that of the trailing obstacle, which is expected because the stagnation point of the flow, caused by the freestream air coming to a complete rest due to the presence of the leading obstacle, is located here. The front half of the trailing obstacle, however,

experiences a higher pressure than the front half of the leading obstacle for positions greater than 0.2 ft but less than 1.4 ft. This differential in pressures between the front half and rear half of the obstacle leads to a negative interference effect for the trailing obstacle and a positive interference effect for the leading obstacle.

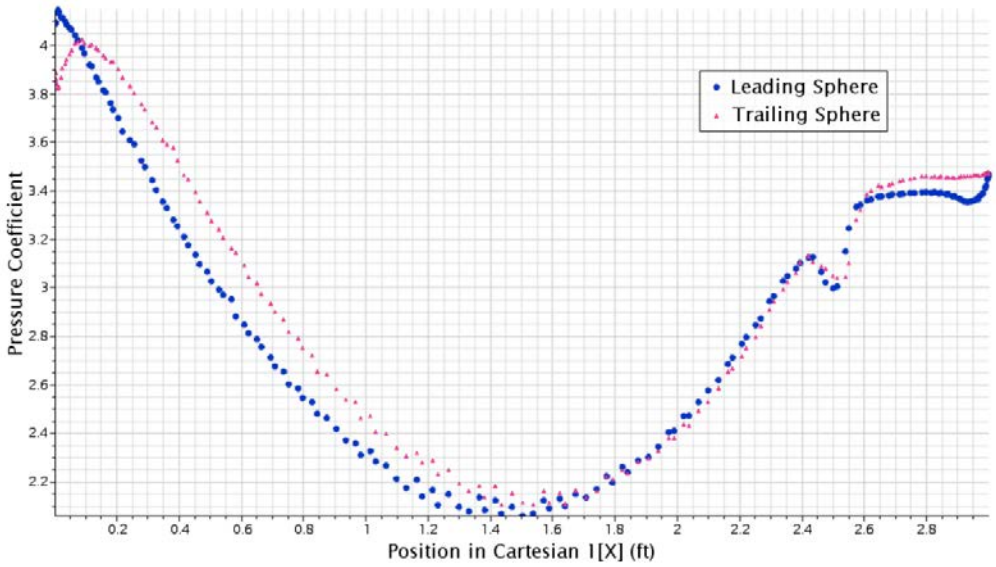

Figure 55. Pressure coefficient along hemisphere centerlines in 25,000 ft flow.

A similar interference phenomenon was observed in wind tunnel experiments conducted by Biermann and Herrnstein while studying interference effects between two struts lined up in tandem. Hoerner also observed a similar interference effect noting, "the fact that the drag of the first section is decreased is explained by increased static pressure between two struts pushing the first one forward, so to speak."[8]

Effect of Separation Distance

Figure 56 presents the coefficient of drag of two equally-sized hemispheres as a function of various separation distances. The separation distance between two hemispheres

is expressed in multiples of a reference dimension, which in this case is the diameter of the leading obstacle of 1.5 ft. The results show that when the obstacles are close to each other, the interference effects are most drastic since the calculated sensitivity values are furthest from unity. The set of distances that correspond to the most pronounced interference effects is named the *zone of influence*.

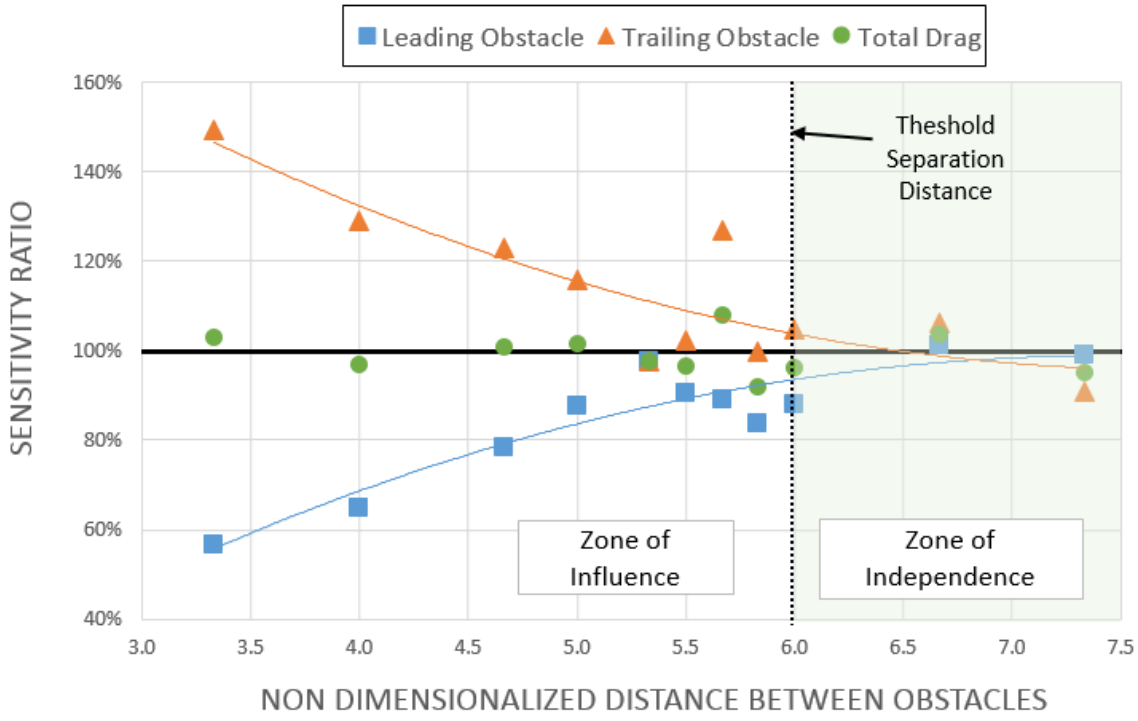

Figure 56. Drag coefficients of two wall-mounted hemispheres separated by various lengths.

When the obstacles are furthest apart, the sensitivity values of each obstacle vary very little from unity and these distances define the *zone of independence*. The drag coefficient of both obstacles changes very little in the zone of independence. The threshold between the zone of influence and zone of independence is shown by the vertical dotted line in Figure 56, and is approximately 6.0 times the reference length of the leading

obstacle. The transition into that zone is gradual, and the drag coefficients plateau and approach a stable value. The *threshold distance* is defined as the separation distance where the sensitivity of both obstacles, according to the trend lines, are within 10% of unity.

The average sensitivity value of the total drag coefficient of both obstacles for all the distances studied is 0.99 which indicates that there is little *net* advantage to locating two obstacles of similar sizes in the zone of independence or the zone of influence. If a *local* reduction in drag forces is desired, however, (1) placing the leading obstacle as close as possible to the trailing obstacle will lower the drag on the leading obstacle and (2) placing the trailing obstacle at a distance greater than the 6D distance away will lower the drag on the trailing obstacle.

The drag coefficient of the trailing obstacle increases when placed closer to the leading obstacle. This effect appears to contradict a popularized phenomenon known as "drafting." In road bicycle races, drafting occurs when two cyclists travel directly behind each other, inches apart, to reduce drag and achieve better performance.[32] The benefits of drafting occur because the region directly behind the leading obstacle is an area of low pressure, which acts like a vacuum. The trailing obstacle is pulled forward slightly, due to the suction and this leads to a reduction in drag. In the cases studied in this paper, however, there exists a region of high pressure between the obstacles which leads to increased drag.

The incongruity between the benefits of drafting and the results of this study can be attributed to the differences in the magnitude of separation distances. For drafting to occur, the trailing obstacle must be within inches of the leading obstacle whereas the separation distance in this study are few orders of magnitude higher than the distances necessary for drafting.

Figure 57 shows the drag coefficient of a leading hemisphere and trailing pod-like shape at various separation lengths. The trends of the sensitivity values of the hemisphere and pod-shape are similar to those of two hemispheres positioned in tandem. When the objects are closest to each other, the leading obstacle experiences reduced drag forces, indicated by sensitivity values less than one, and the trailing obstacle experiences higher drag forces, indicated by sensitivity values greater than one. At distances greater than approximately 5.5D, the sensitivity values are close to one indicating the interference effects are negligible.

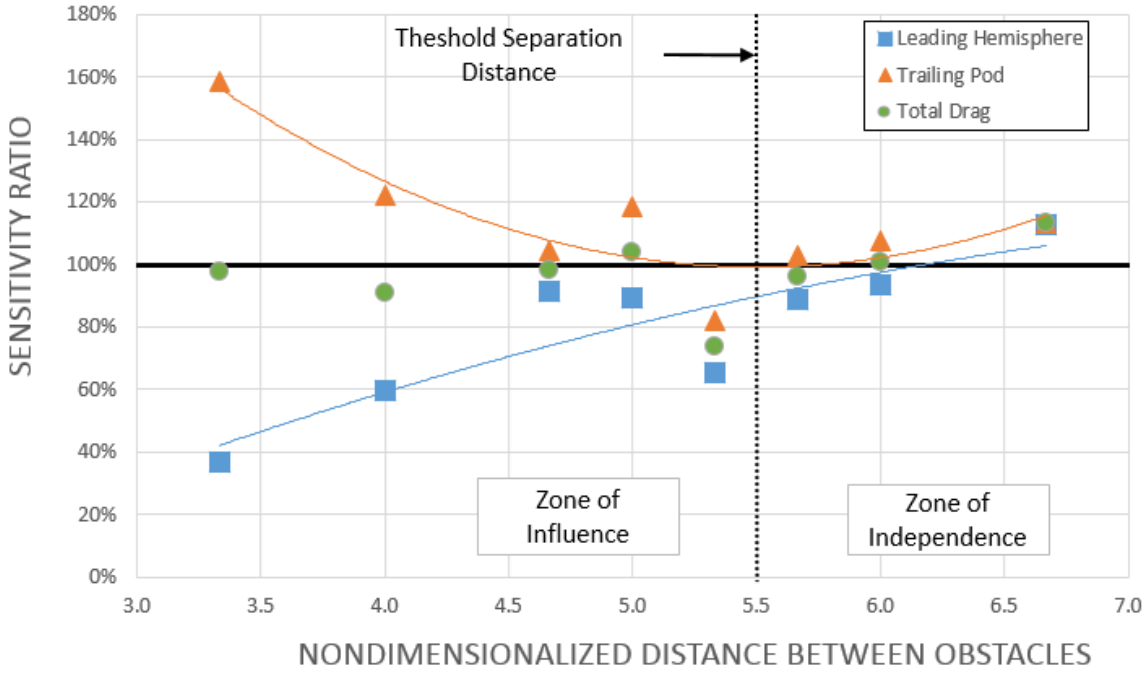

Figure 57. Drag coefficient of a hemisphere and pod shape separated by various lengths.

The sensitivity of both obstacles is on average 0.97, which indicates that there is no significant advantage to placing the hemisphere and pod-shape in either the zone of influence or zone of independence. Similar to the two-hemisphere case, placing the pod-shape further away from the leading obstacle locally reduces the drag force on the pod.

Conversely, placing the leading hemisphere closest to the pod locally reduces the drag force on the hemisphere.

Effect of Trailing Obstacle Shape

Figure 58 presents data comparing the calculated sensitivities of two hemispheres in tandem and a hemisphere and pod-shape in tandem. In all cases, the obstacles are in 0.40 Mach and 1.6 x 10^7 Reynolds number flow.

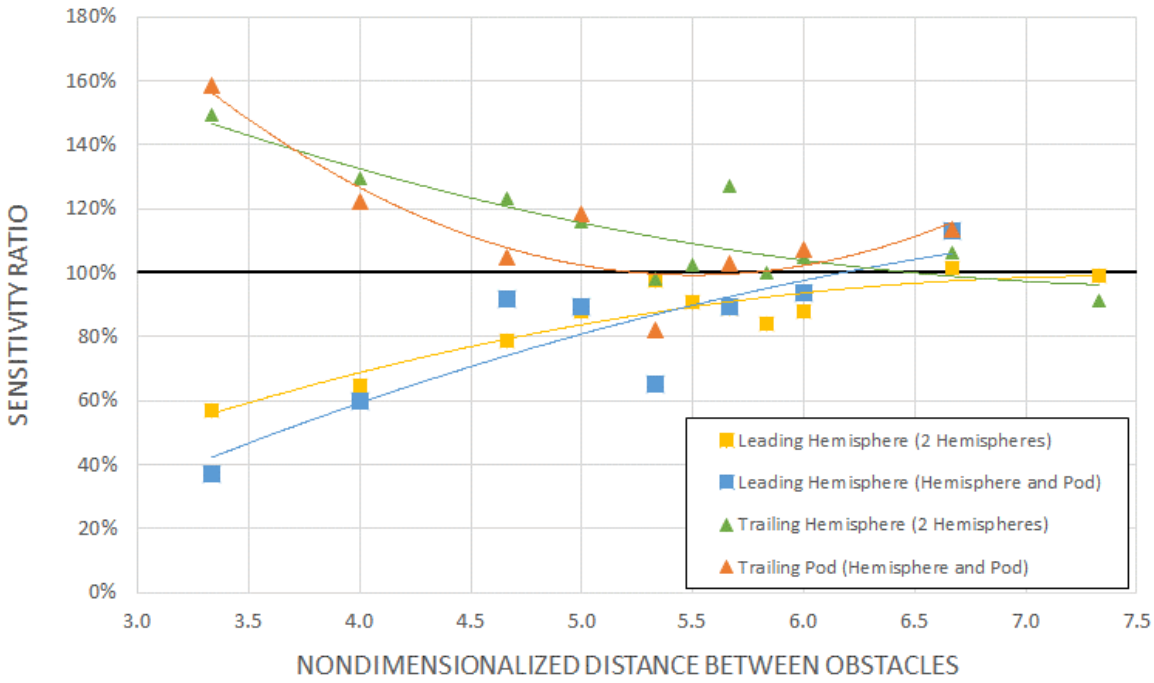

Figure 58. Comparison of sphere and pod drag coefficients.

The interference effects experienced by a trailing hemisphere is similar in magnitude to a trailing pod even though the pod has a larger surface area and more skin friction drag. This indicates that the additional viscous drag caused by a pod's larger surface area is compensated by a favorable interference-drag effect. This finding is useful for engineers seeking to design ISR modifications that encapsulate a greater volume for a negligible drag penalty.

Also, when the obstacles are closer together, the interference effects are approximately 10% more favorable to the hemisphere that precedes a pod-shape than the hemisphere that precedes another hemisphere.

The threshold distance where interference effects become negligible occurs at a smaller distance for a trailing pod shape than a trailing hemisphere shape. This indicates that obstacles with higher fineness ratios have smaller zones of influence. The pod shape, which has a fineness ratio of 2.33, has a threshold separation distance of 5.5D, or 5.5 times the characteristic leading obstacle length. The threshold separation distance for a trailing hemisphere, which has a fineness ratio of 1, is 6.0D. The threshold distance is defined as the separation distance where the sensitivity of both obstacles is within 10% of unity.

On small aircraft, where space is limited, the trailing obstacle's shape can be altered to avoid adverse interference effects. The same interference effect on drag coefficient can be achieved as placing the two obstacles in the zone of independence and by increasing the fineness ratio of the trailing obstacle. Additional data is necessary to understand exactly how the fineness ratio affects the threshold separation distance.

Effect of Trailing Obstacle Size

Figure 59 presents the drag coefficient of two hemispheres of unequal size placed 3.5D distance apart and in 0.40 Mach and 1.6×10^7 Reynolds number flow. As the diameter of the trailing obstacle increases, its sensitivity increases. Simultaneously, the sensitivity of the leading obstacle decreases.

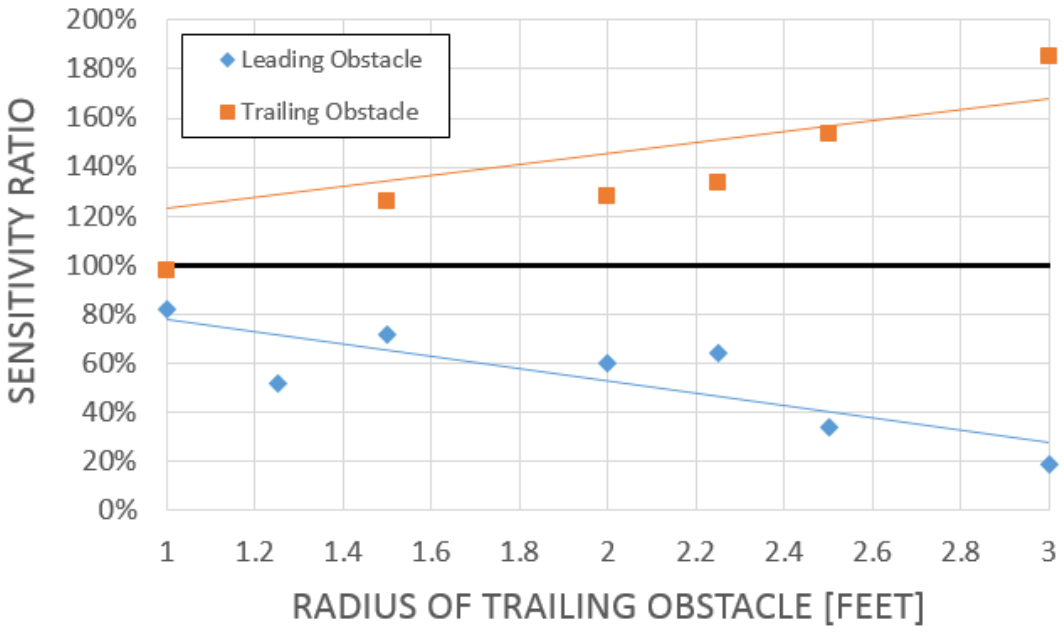

Figure 59. Sensitivity values of two hemispheres as a function of trailing obstacle size.

To investigate why the leading obstacle experiences a reduction in drag, the streamlines are calculated around both obstacles for when the trailing obstacle is small and large. The data on the calculated streamlines are presented in Figure 60 and Figure 61.

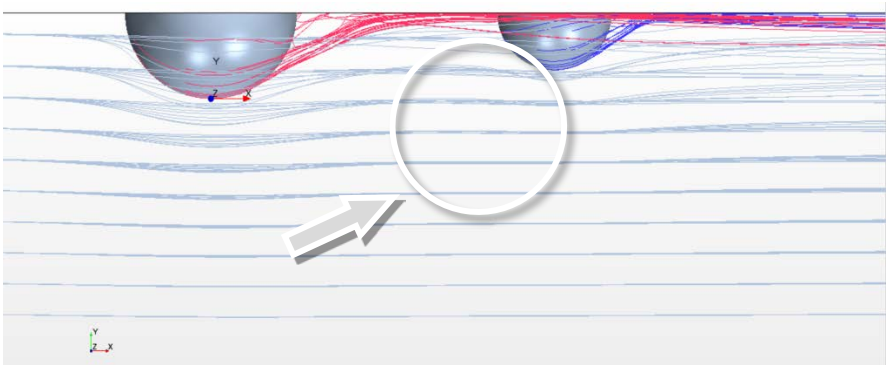

Figure 60. Streamlines around two hemispheres on a wall; trailing hemisphere 1ft diameter.

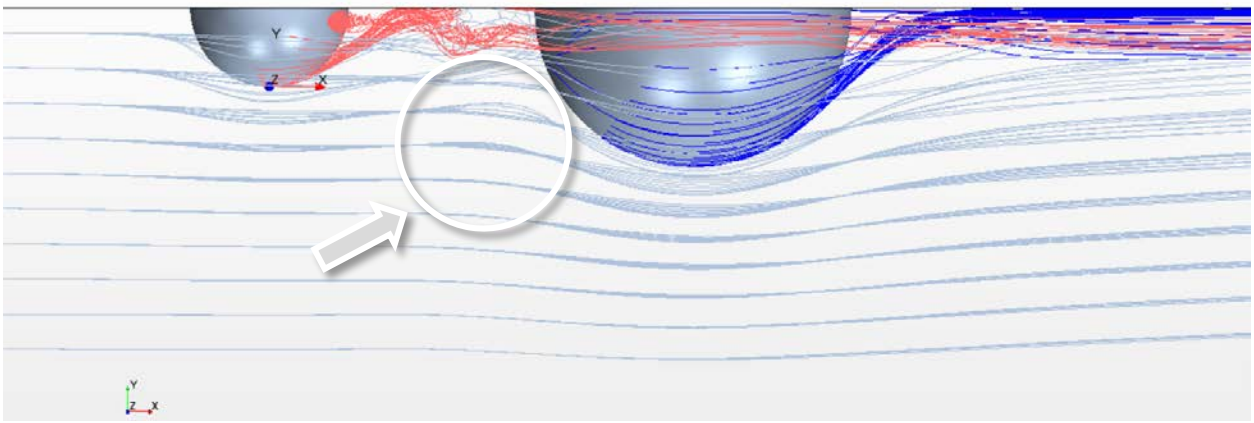

Figure 61. Streamlines around two hemispheres on a wall; trailing hemisphere 3 ft diameter.

In all cases, as the fluid approaches the leading obstacle, it also senses the presence of the downstream obstacle. Information about the trailing obstacle with a larger diameter however propagates further upstream, as shown by the downward deflection of the streamlines in the indicated region in Figure 61. The larger trailing obstacle pushes against the incoming flow and creates a high pressure region between the two obstacles. This high pressure region creates a stronger adverse pressure gradient for the incoming flow and leads to flow separation directly behind the leading obstacle as indicated by the turbulent streamlines in Figure 61.

The high pressure region between the two obstacles also creates a more favorable pressure differential for the leading obstacle and lowers its sensitivity. This favorable interference effect is sometimes called “shielding” because the trailing obstacle shelters the leading obstacle from experiencing high drag forces. The high pressure region between the two obstacles also creates an unfavorable pressure differential for the trailing obstacle and increases its sensitivity ratio.

The shielding effect is stronger when the trailing obstacle is largest. The shielding effect can be leveraged to decrease the aerodynamic load on protruding aerospace structures and potentially lead to structural weight and cost savings.

Effect of Trailing Obstacle Size and Distance

Previous results demonstrated that when two obstacles of equal size are close to each other, the sensitivity of the leading object drops below 1.0, and the sensitivity of the trailing obstacle rises above 1.0. Secondly, when two obstacles are placed further away from each other, the drag sensitivity of each should approach 1.0. Lastly, if two obstacles of equal size are co-located such that they occupy the same space, which is only possible theoretically, then the sensitivity of each should also equal unity because there would be no interference effects between the two objects (the air flows around each obstacle as if there is only one obstacle). All three of these trends are summarized in Figure 62. Figure 62 illustrates a generic trend of the sensitivity of each object as a function of separation distance for two objects of equal size.

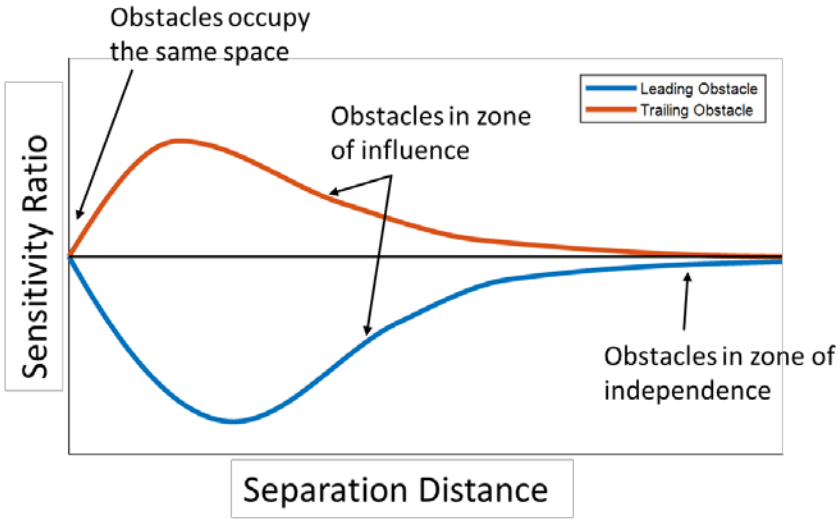

Figure 62. Generic trend of the drag sensitivity of two obstacles of equal size placed in tandem.

What happens to the sensitivity of each obstacle when the objects are of unequal size? The sensitivity of each obstacle would still trend to unity when they are located farther away, since placing objects far away from each other is the same as having them isolated. However as two unequally-sized objects occupy the same space, the situation becomes problematic. If a small obstacle is engulfed by a large obstacle at zero separation distance, does it experience zero drag? Or does it experience the same drag as the larger obstacle? This theoretical scenario can be resolved with CFD data, which is out of scope for this thesis and is suggested as an area for future research. To proceed with the analysis, and for simplicity, the author assumes that two obstacles, when collocated such that they occupy the same space, have a drag sensitivity of one, just like when two obstacles were of equal size. Data that were collected as part of this study are presented in Figure 63 and Figure 64 as a function of a non-dimensional separation distance.

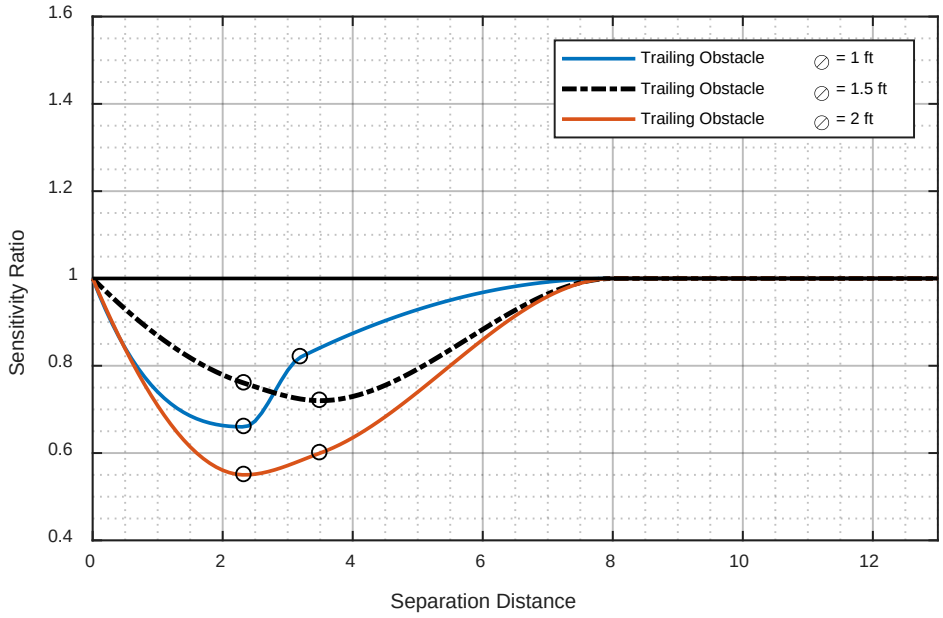

Figure 63. Sensitivity ratio of the leading obstacle for various distances and trailing obstacle size.

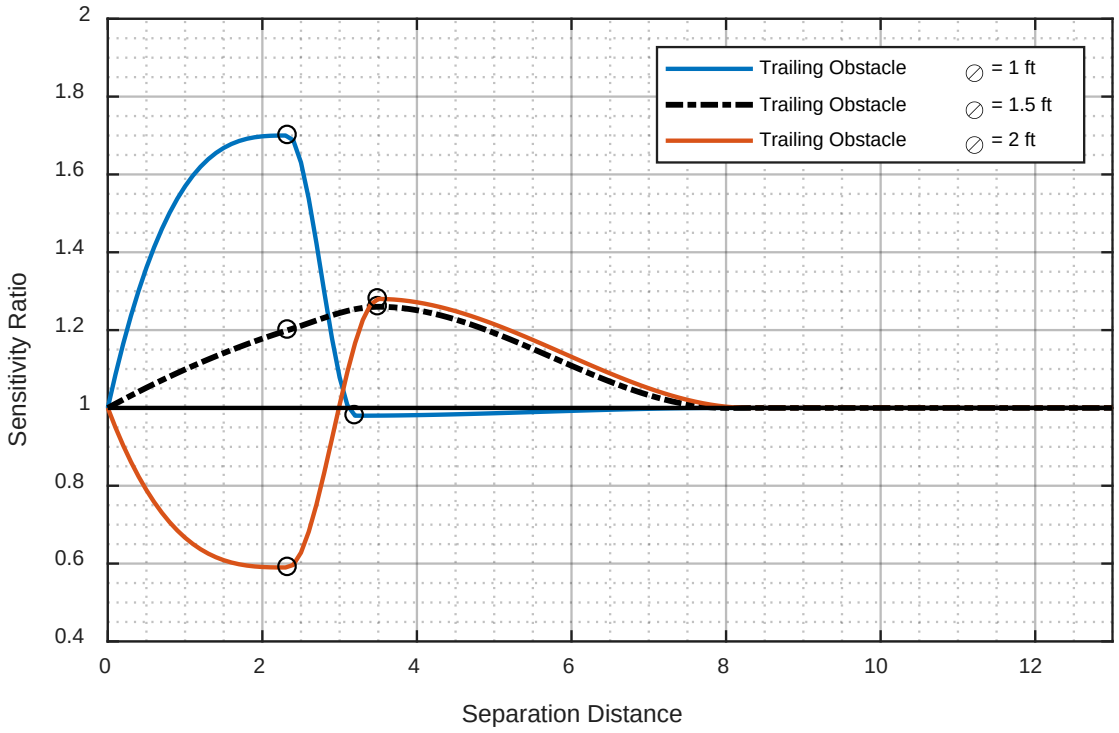

Figure 64. Sensitivity ratio of the trailing obstacle for various distances and trailing obstacle size.

The trends lines shown are a piecewise polynomial based on (1) two CFD calculations which are marked by circles, (2) the knowledge that the sensitivity trends to unity when the separation distance becomes infinitely great, and (3) the assumption that sensitivity trends to unity when the separation distance is zero. The curves illustrated in Figure 63 and Figure 64 are not unique solutions and additional data is necessary to fully determine the trends. Some general comments, however, are now presented.

Figure 63 shows the drag sensitivity of the leading obstacle for various trailing obstacles sizes. The data shows that there is a clear advantage to placing larger obstacles behind the leading obstacle for all separation distances. A subset of this observation was observed in a prior section in this thesis where the interference effect was called

“shielding.” The data shows that a larger trailing obstacle lowers the drag of the leading obstacle regardless of where it is positioned with respect to the leading obstacle.

The sensitivity trends of the trailing obstacle, shown in Figure 64, are harder to generalize. The data point at 2.3D separation distance and a trailing obstacle size of 2 ft is suspect. The first attempt at calculating the CFD solution at this data point failed because the case would not converge when the solution was initialized with a uniform flow field and CFL of unity. The failure is difficult to diagnose further because of the lack of transparency in the Star CCM+ code. Nonetheless, by examining the residual errors in mass, momentum, and energy equations, which increased above unity, the author speculates that resolving the turbulent flow near the separation region led to large instabilities. It is likely that the first attempt at calculating the answer was caused by imposing starting conditions that the mesh and models were ill-equipped to solve. On the second attempt, the solution was initialized with a high CFL (~50) and was ramped down to unity. This method led to a converged solution, which is recorded as the suspect point. A repeat calculation is necessary, perhaps with a finer mesh, to verify the data. Until this additional data is collected, nothing further can be generalized on the effects of separation distance and trailing obstacle size on the sensitivity of the trailing sphere.

Figure 65 and Figure 66 present the same data as Figure 63 and Figure 64 except the abscissa is different. The trend lines shown are a linear least-square fit corresponding to fixed separation distances. The trend lines intersect when the two obstacles are roughly of equal size at 1.5 ft. This indicates that there is a shift in trends depending on whether the trailing obstacle is smaller or larger than the leading obstacle. Again, the trends are based

on a very limited data set and more calculations are necessary to fully understand the interference effects.

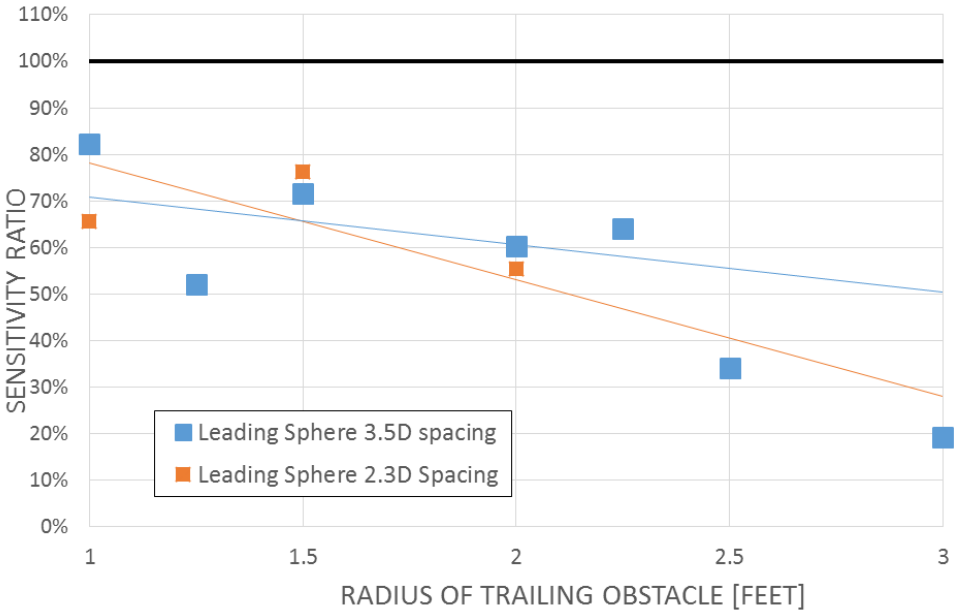

Figure 65. Effect of trailing obstacle size on the leading obstacle at varying separation distances.

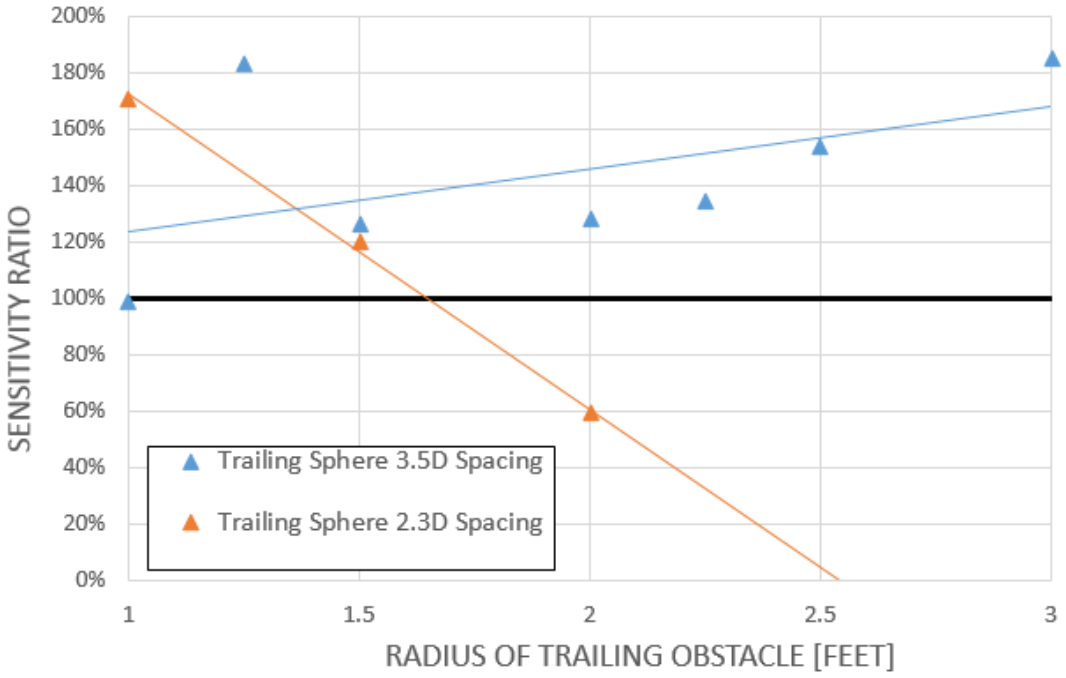

Figure 66. Effect of trailing obstacle size on the trailing obstacle at varying separation distances.

CFD Modeling and Scatter

There are two sources of error in the CFD calculations performed in this study. The first source of error is due to the iterative nature in which the discretized RANS equations are solved. In order to reduce computational cost and decrease time to compute, the iterations were stopped when the solution was within 1% of the previous iteration such that

$$\varepsilon = (\mathrm{C_{d,previous}} - C_{d,final})/C_{d,final} = .01 \qquad \textit{Eq. 86}$$

The second source of error is the discretization error, which in this case is the difference between the computed value and the true value of the coefficient of drag. This type of error stems from the type of numerical scheme used by the numerical algorithm and the fineness of the grid used to solve the exact partial differential equation. Discretization error can be quantified by comparing the solution of the exact Navier Stokes equations with the solution arrived through computational means.[33] Several scenarios, such as the computation of flow field in a lid-driven cavity and turbulent flow around a 2D cylinder, were performed to show that the discretization error is low and acceptable.

The scatter in the data is now addressed by understanding the types of uncertainties in this problem. In high Reynolds number (i.e., turbulent) flows, there are aleatory and epistemic uncertainties.[34] *Aleatory uncertainty* is due to inherent randomness of fluid particles. This type of randomness manifests itself in experimental data however it is not manifested in computational data. This is because real turbulent flows are non-deterministic flows. CFD flows are, by virtue of being implemented on a machine, repeatable, especially when a converged solution is required. It would seem looking for aleatory, or random, errors in a computational solution, is a paradoxical endeavor. Numerical error, which was discussed earlier, is an artificial, computer-generated

randomness which can be similar to natural randomness. Numerical errors, which arise due to the precision capabilities of a computer, can be thought of as a substitute for aleatory variability. Sometimes Monte Carlo methods are used to propagate such uncertainties. This study does not implement Monte Carlo methods and relies on numerical error to simulate the aleatory nature of real flows.

The second type of uncertainty is epistemic. *Epistemic uncertainty* is due to lack of knowledge about flow and the model being used to describe that flow. This type of error is also referred to as reducible uncertainty because the models can be changed to minimize epistemic uncertainty. In real flows, this type of error can be quantified by recreating the flow with the same initial conditions as precisely as possible and looking at the distribution of error in the final result.

To understand the distribution of aleatory and epistemic error in any CFD solution, each case must be calculated multiple times and the distribution of error in the solution analyzed. For this study, however, it was impractical to run each test case multiple times and determining the uncertainty in the results was not pursued thoroughly.

It is unknown how representative the computational scatter in the solutions is of the scatter in real flows. Since the epistemic errors were minimized as much as possible, it is likely the scatter stems from aleatory uncertainty. Ultimately, nothing can be done to reduce the numerical error due to precision capabilities of a computer, so there is no choice but to take precaution when analyzing data with scatter.

Figure 67 summarizes the many layers of separation between the real behavior of fluids observed in nature and the many layers of models found in CFD. Inherently CFD models are subject to epistemic uncertainty since natural phenomena is always

approximated. For example, the time and computational power available to generate a geometric mesh determines the fidelity of the model to reality. The time available, and therefore number of iterations performed to arrive at the solution, also contributes to the accuracy of the CFD solution. The choice of physics models, along with the fineness of the mesh, determines the scales of fluid behavior that are observed in the CFD solution. The numerical algorithm and computer's precision determines the accuracy of the final solution.

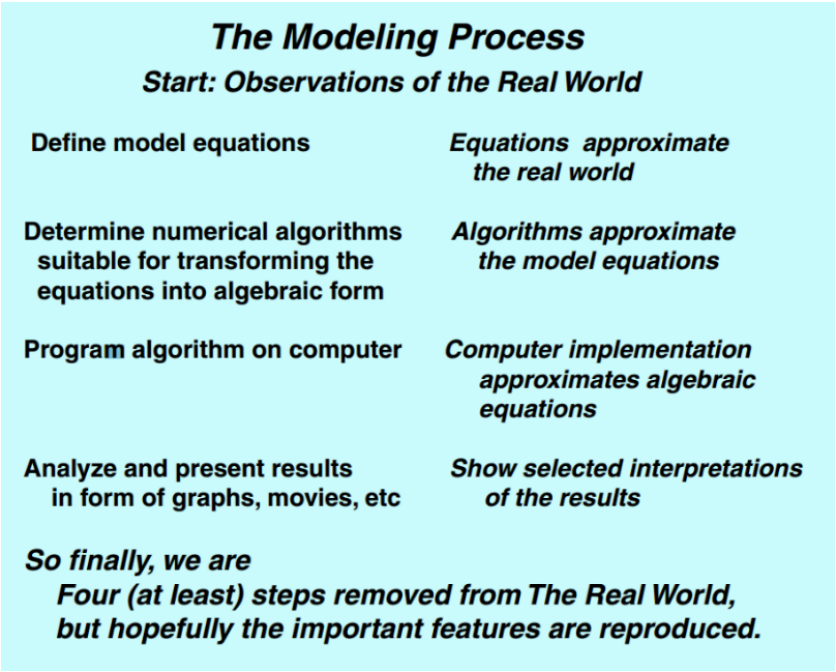

Figure 67. The modeling process.[35]

Despite the degrees of separation between the reality and CFD result, if a particular problem is well-defined, the computational answer can be useful and sufficiently accurate. Chapter 4 presented results that show epistemic error has been minimized by comparing the calculated answer to real and known solutions. Additionally, tests were performed to validate the numerical algorithm, the size of the mesh and the choice of physics models.

Chapter 7: Conclusion

Public information is scant on optimized shapes and positions of two obstacles mounted on a wall and exposed to atmospheric conditions experienced by commuter aircraft like the King Air 350. Aircraft designers need design data that show the optimal size and location for aerodynamic fairings on modified aircraft flying at approximately Mach 0.4 and Reynolds number of 1.64×10^7.

Having identified the need for this information, a general CFD study was performed. The drag coefficients were computed for multiple-sized hemispheres, for multiple distances between the hemispheres and for various shapes of the trailing obstacle, including an oblong pod shape. The results were analyzed and explanations for some trends were provided.

Summary

Two hemispherical objects placed in tandem on a wall in the vicinity of each other, produce approximately the same overall drag as when the obstacles are aerodynamically isolated. The interference drag causes the trailing hemisphere to experience a higher drag and the leading hemisphere to experience a lower drag. This result is in agreement with Biermann and Herrnstein's work on interference effects between two streamlined bodies.[7] The variation in local drag forces indicates the trailing obstacle requires more structural support while the leading obstacle requires less structural support.

As Mach number increases, the interference effects cause an increase in drag on both obstacles. As Reynolds numbers increases, the interference effects cause a decrease in drag on both obstacles. Additionally, the leading obstacle will experience lower drag

when the size of the trailing obstacle increases and is greater than the size of the leading obstacle.

The study also finds that in order to reduce drag on a leading obstacle, it should be located close to, and less than a critical threshold distance apart, from another trailing obstacle of the same size. When the two obstacles were spaced greater than these threshold distances, the interference drag is negligible and the drag coefficients of the obstacles are independent of each other.

The critical threshold distance is influenced by the fineness ratio of the trailing obstacle. When the fineness ratio of the trailing obstacles was 1 (spherical shape), the threshold distance was 6 times the diameter of the leading obstacle. When the fineness ratio was 2.33 (elongated pod shape), the threshold distance was 5.5 times the diameter of the leading obstacle. Increasing the fineness ratio, or elongating the shape of the trailing obstacle, lowers interference drag for a fixed separation distance. This finding is in agreement with Hoerner's work[8] on the drag coefficient as a function of an object's fineness ratio.

The data gathered in this study provides trends for only a small range of independent variables in the domain and does not give a complete picture of the flow. Nevertheless, the recommendations summarized above will be useful to structural and aerodynamic engineers, who have limited time and budget, but must design fairings on the outside mold line of aircraft.

Future Work

A few areas of further study are suggested to complete the drag trends examined in this trade-study. Additional research is recommended to explore different pod geometries,

including pods of various fineness ratios and thickness ratios. Furthermore, since pods on ISR aircraft often house radar systems, a study on pods with planar sides instead of curved sides should also be explored, since pods with planes are desirable for easier performance predictability.

Another recommended study involves understanding the interference drag of obstacles mounted on a curved surface instead of a planar surface. The planar assumption used in this study is valid for large aircraft where the radius of curvature can be approximated as a flat plane over small segments. Many helicopters, general-aviation aircraft, and unmanned aerial vehicles have smaller fuselages and the aforementioned assumption cannot be made. Quantifying the effect of a curved mounting surface would be useful in generalizing the drag trends for large and small aircraft.

Finally, a study of interference drag on multiple objects in staggered orientations is necessary. Mounting protrusions in a tandem manner is not always possible due to limited availability of space on airplanes. Additionally, aircraft often fly in crosswind conditions where a component of free-stream flow approaches the obstacles from the side. This change in velocity direction can substantially alter the aerodynamic forces, which must be understood for structural reasons and, perhaps, for aircraft control and stability reasons.

The results of all these additional studies can be readily applied and made useful in existing and future aircraft designs.

Bibliography

[1] Cenciotti, D. "Russia Has Just Deployed Its Most Advanced Spyplane to Syria." The Aviationist. The Aviationist, 15 Feb. 2016. Web. 21 Nov. 2016.

[2] Stedman, G. "Global Express #2 |." Gary1701.piwigo.com. Gary Stedman Photography, 16 Apr. 2011. Web. 21 Nov. 2016.

[3] MilborneOne. “N162QS –Global 6000.” Wikimedia Commons. Wikimedia Commons, 15 July 2014. Web. 21 Nov. 2016. <https://commons.wikimedia.org/w/index.php?curid>.

[4] Smith, M. “Induced Drag” Michael Smith CFI. 25 December 2017. <http://www.pilotwings.org/induced-drag.html>

[5] Sakellaridis, A. (2002). Experimental study of interference drag for multi-element objects. Experimental Thermal and Fluid Science, 26(2), 313-317. doi:10.1016/S0894-1777(02)00142-5

[6] Hoerner, S. (1958). Fluid-dynamic drag: Practical information on aerodynamic drag and hydrodynamic resistance (2nd ed. ed.). Midland Park, N.J.: Dr.-Ing. S.F. Hoerner, (pages 7-10)

[7] Biermann, D. (1933). The interference between struts in various combinations. Ft. Belvoir: Defense Technical Information Center.

[8] Hoerner, S. (1958). Fluid-dynamic drag: Practical information on aerodynamic drag and hydrodynamic resistance (2nd ed. ed.). Midland Park, N.J.: Dr.-Ing. S.F. Hoerner, (pages 8-2)

[9] Hoerner, S. (1958). Fluid-dynamic drag: Practical information on aerodynamic drag and hydrodynamic resistance (2nd ed. ed.). Midland Park, N.J.: Dr.-Ing. S.F. Hoerner, (pages 8-3)

[10] Kubendran, L. (1984). Interference drag in a simulated wing-fuselage juncture (NASA contractor report, 3811). Washington, D.C.: National Aeronautics and Space Administration, Scientific and Technical Information Branch. (page 3)

[11] Barry, N. (2015). Aerodynamic drag interactions between cyclists in a team pursuit. Sports Engineering, 18(2), 93-103. doi:10.1007/s12283-015-0172-8

[12] Dogan. A., Blake, W., Haag, C. (2013). Bow wave effect in aerial refueling: Computational analysis and modeling. Journal of Aircraft, 50(6), 1856-1868. doi:10.2514/1.C032165

[13] Emeis, S., Dr. (1990). Surface pressure distribution and pressure drag on mountains. Meteorology and Atmospheric Physics, *43*(1-4), 173-185. doi:10.1007/BF01028120

[14] Norodah, E. “Aviation Photo #1873190: Raytheon 350 King Air (B300) - USA - Air Force. “ Airliners.net. Airliners.net 17 Feb 2011. Web. 21 Nov 2016. <http://www.airliners.net/photo/USA-Air-Force/Raytheon-350-King-Air-(B300)/1873190>.

[15] Section 5 Performance, King Air 350/350i/350C (Model B300/B300C) POH/AFM, Wichita, Kansas, Beechcraft Corporation (March 2013)

[16] Cavcar, M. The International Standard Atmosphere (ISA). 1st ed. 26470 Eskisehir, Turkey: Anadolu University. Web. 21 Nov. 2016.

[17] Sutherland, W. (1893), "The viscosity of gases and molecular force", Philosophical Magazine, S. 5, 36, pp. 507-531 (1893).

[18] Anderson, J. D. (1984). Fundamentals of aerodynamics. New York: McGraw-Hill, (pages 107-131).

[19] Tu, J., Yeoh, G. H., & Liu, C. (2008). Computational fluid dynamics: A practical approach (1st ed.). Amsterdam: Butterworth-Heinemann.

[20] Métais, O., Ferziger, J. H., & Centre de physique des Houches. (1997). New tools in turbulence modelling: Les Houches School, May 21-31, 1996(Centre de physique des Houches, 5; Centre de physique des Houches (Series), 5). Berlin: Springer-Verlag.

[21] Rumsey, C. “The Spalart-Allmaras Turbulence Model.” NASA. NASA, 10 June 2016. Web. 21 Nov. 2016. <https://turbmodels.larc.nasa.gov/spalart.html>.

[22] Hewitt, G. F., & Vassilicos, J. C. (2005). Prediction of turbulent flows. Cambridge: Cambridge University Press. http://catdir.loc.gov/catdir/toc/cam051/2004054471.html

[23] Wilcox, D. C. (2006). Turbulence modeling for CFD (3rd ed.). La Cãnada, Calif.: DCW Industries.

[24] Bardina, J.E., Huang, P.G., Coakley, T.J. (1997), "Turbulence Modeling Validation, Testing, and Development", NASA Technical Memorandum 110446.

[25] Osama, A., Marzouk, E., Huckaby, D. Simulation of a Swirling Gas-Particle Flow Using Different k-epsilon Models and Particle-Parcel Relationships, Engineering Letters, 18:1, EL_18_1_07

[26] Wilcox, D. C. (2006). Turbulence modeling for CFD (3rd ed.). La Cãnada, Calif.: DCW Industries.

[27] User Guide STAR-CCM+ Version 8.06. 2013, CD-adapco.

[28] Wendt, J. F., Anderson, J. D., & Von Karman Institute for Fluid Dynamics. (2009). Computational fluid dynamics : An introduction (3rd ed.). Berlin: Springer. http://site.ebrary.com/id/10253766

[29] Sadraey, M. (2009). Aircraft performance analysis. Saarbrücken, Germany: VDM Verlag Dr. Müller.

[30] Barlow, J. (1999). Low-speed wind tunnel testing (3rd ed. ed.). New York: Wiley.

[31] Oran, E. S., & Boris, J. P. (2009). Numerical Simulation of Reactive Flow (2nd Edition). Cambridge, GBR: Cambridge University Press.

[32] Belloli, M., Giappino, S., Robustelli, F., & Somaschini, C. (2016). Drafting Effect in Cycling: Investigation by Wind Tunnel Tests. Procedia Engineering, 147, 38-43. doi:10.1016/j.proeng.2016.06.186

[33] Knight, K. (2012). Interference drag modeling and experiments for a High Reynolds number transonic wing. Journal of Aircraft, *49*(6), 1894-1903. doi:10.2514/1.C031731

[34] Oberkampf, W. (2002). Error and uncertainty in modeling and simulation. Reliability Engineering and System Safety, *75*(3), 333-357. doi:10.1016/S0951-8320(01)00120-X

[35] Oran, E. S. (2002). Matchsticks, Scramjets, and Black Holes: Numerical Simulation Faces Reality. AIAA Journal, 40(8), 1481-1494. doi:10.2514/2.1823